Development of compact, highly sensitive beam position monitors for storage rings

Von der Fakultät für Mathematik, Informatik und Naturwissenschaften der RWTH Aachen University zur Erlangung des akademischen Grades eines Doktors der Naturwissenschaften genehmigte Dissertation

vorgelegt von

Master of Science Physics

Falastine Abusaif

aus Ramallah, Palästina

Berichter: Univ.-Prof. Dr. rer. nat. Jörg Pretz
Univ.-Prof. Dr. rer. nat. Achim Stahl

Tag der mündlichen Prüfung: October 29, 2021

Diese Dissertation ist auf den Internetseiten der Universitätsbibliothek verfügbar.

Eidesstattliche Erklärung

I hereby declare that I have created this work completely on my own and used no other sources or tools than the ones listed, and that I have marked any citations accordingly.

Hiermit versichere ich, dass ich die vorliegende Arbeit selbständig verfasst und keine anderen als die angegebenen Quellen und Hilfsmittel benutzt sowie Zitate kenntlich gemacht habe.

Jülich, November, 2021
Falastine Abusaif

Contents

List of Figures

List of Tables

Abstract

The JEDI* collaboration is currently performing a direct measurement of the **E**lectric **D**ipole **M**oment (EDM) of charged particles with beams of polarized protons and deuterons, using the **CO**oler **SY**nchrotron (COSY) at the Forschungszentrum Jülich in Germany.
For the precision EDM search, the JEDI collaboration is aiming for an experimental target with systematic errors of the same order of magnitude as the statistical sensitivity of 10^{-29} e cm per year of data acquisition. The **M**agnetic **D**ipole **M**oment (MDM) is many orders of magnitude larger than the EDM. If the beam trajectory in the storage ring deviates from the nominal trajectory, this can cause the particles to move through a radial magnetic field. As a result of the interaction with the MDM, this leads to spin precessions which are indistinguishable from a true EDM signal.
Therefore, it is important that the beam orbit be very close to the magnetic center of the focusing elements in the ring. The RMS† deviation of the orbit from the nominal orbit should be as close to zero as possible. This means that the **B**eam **P**osition **M**onitors (BPMs) must have a suitable sensitivity that meets the goals of the EDM experiment up to the desired accuracy level.
In this work, a novel compact inductive BPM based on a segmented toroidal coil (Rogowski coil) has been developed. Various aspects of this Rogowski BPM as a non-destructive monitor for measuring the transverse beam coordinates were investigated.
The theoretical model describing the induced voltages of the Rogowski BPM was extended using the "lumped model" approximation to obtain a more realistic description of the measurement of the induction signals. In this extended model, the coupling between individual quadrant coils was considered. Further theoretical studies were performed to investigate the effect of the angular overlap of the winding on the electrical response. Also, the sensitivity of the beam positions to the specifics of the windings of the segments was investigated.
Electromagnetic simulations performed in COMSOL Multiphysics were used to investigate a simple 3D model for the Rogowski BPM. Simulations were performed in both time and frequency domains. Different boundary conditions were applied on individual quadrants to investigate the electrical properties of the coils. Another simplified model

*_**J**ülich **E**lectric **D**ipole moment **I**nvestigations._

†**R**oot **M**ean **S**quare.

describing a single quadrant coil in the Rogowski BPM was developed assuming a 2D axisymmetric geometry. In this analysis, the impedance and the inductance of the single coil were studied over a frequency range of 10MHz.
Several hardware developments and improvements, starting from a simple ring coil up to the complete BPM with its feedthroughs, flanges and connectors, were achieved. Developments on the laboratory test bench enabled more accurate calibrations. The newly developed cylindrical knife-edge structure was used to study the behavior of the stepper motor drives with a laser tracker, and absolute BPM calibration (with an accuracy of a few micrometers) is possible after the BPMs are installed in the accelerator. Calibration measurements for the Rogowski BPM were performed in the test bench and compared with the theoretical model. A good agreement between the measurement results and the theoretical expectations was achieved.
Various experimental investigations were carried out in the laboratory, such as the measurement of the frequency response, the measurement of the position response, the measurement of the stability of the resonance curves, as well as the tuning of the resonance curves with shunt capacitors, the measurement of the time variations of the electrical signals, as well as the effect of the waveform of the excitation source on the BPM calibration, the possibility of using the BPM as a BCT‡, and the distribution of the **S**ignal to **N**oise **R**atio (SNR). In addition, the effect of the geometric specifications of the windings, the way the whole circuit is connected, and the system's **S**elf **R**esonant **F**requency (SRF) on the position resolution at different frequencies were also investigated.
Two Rogowski BPMs with different geometrical and electrical characteristics were developed and successfully installed and tested in COSY. They were installed at the entrance and exit of the **R**adio **F**requency **W**ien **F**ilter (RF WF). The results of local orbit bumps introduced around the RF WF showed reasonable and linear position responses measured by the two BPMs.
A resolution of up to 400 nm was achieved with the Rogowski BPMs (for a single position measured at 750 kHz during a sampling time of 1s, a system's SRF of 3.229 MHz and a particle intensity of 5×10^9). This corresponds to an order of magnitude improvement in resolution compared to typical capacitive BPMs used in COSY. Moreover, with the newly proposed method for absolute instrument calibration, and taking into account the accuracy of the stepper drives used for calibration, as well as the errors caused by temporal drifts, the accuracy of the Rogowski BPMs is expected to be about 20 µm (error of three standard deviations, corresponding to a beam off-centered by 1 cm), which constitutes an improvement by a factor of five compared to typical BPMs.

‡**B**eam **C**urrent **T**ransformer.

Überblick

Die JEDI[§] Kollaboration führt derzeit eine direkte Messung des Elektrischen Dipolmoments (EDM) geladener Teilchen mit Strahlen von polarisierten Protonen und Deuteronen durch, unter Verwendung des COoler SYnchrotrons (COSY) am Forschungszentrum Jülich in Deutschland.
Für die Präzisions-EDM-Suche strebt die JEDI-Kollaboration ein experimentelles Ziel mit systematischen Fehler in der gleichen Größenordnung wie die statistische Empfindlichkeit von 10^{-29} e cm pro Jahr der Datenaufnahme an. Das magnetische Dipolmoment (MDM) ist um viele Größenordnungen größer als das EDM. Wenn die Strahltrajektorie im Speicherring von der Sollbahn abweicht, kann dies dazu führen, dass die Teilchen sich durch ein radiales Magnetfeld bewegen. Infolge der Wechselwirkung mit dem MDM führt dies zu einer Spinpräzession, welche nicht von einem echten EDM Signal zu unterscheiden ist.
Daher ist es wichtig, dass der Strahlorbit sehr nahe am magnetischen Zentrum der fokussierenden Elemente im Ring liegt. Die RMS[¶] Abweichung des Orbits von der Sollbahn sollte so nahe wie möglich am Nullpunkt liegen. Dies bedeutet, dass die Strahlpositionsmonitore (BPMs) eine geeignete Empfindlichkeit haben müssen, die bis zu dem gewünschten Genauigkeitsniveau den Zielen des EDM-Experiments entspricht.
Im Rahmen dieser Arbeit wurde ein neuartiger kompakter induktiver BPM auf Basis einer segmentierten Ringspule (Rogowski-Spule) entwickelt. Verschiedene Aspekte dieses Rogowski BPM als zerstörungsfreier Monitor zur Messung der transversalen Strahlkoordinaten uerden untersucht.
Das theoretische Modell, welches die induzierten Spannungen des Rogowski-BPM beschreibt, wurde mit Hilfe der "lumped model"-Näherung erweitert, um eine realistischere Beschreibung der Messung der Induktionssignale zu erhalten. In diesem erweiterten Modell wurde die Kopplung zwischen einzelnen Quadrantenspulen berücksichtigt. Weitere theoretische Untersuchungen durchgeführt, um die Auswirkung der Winkelüberdeckung der Wicklung auf die elektrische Antwort zu untersuchen. Außerdem wurde die Empfindlichkeit der Strahlpositionen gegenüber der Wicklung der Spulensegmente untersucht.
Elektromagnetische Simulationen, die in COMSOL Multiphysics durchgeführt wurden,

[§] ***J****ülich* ***E****lectric* ***D****ipole moment* ***I****nvestigations.*
[¶] **R**oot **M**ean **S**quare.

dienten dazu, ein einfaches 3D-Modell für das Rogowski-BPM zu ermitteln. Die Simulationen wurden sowohl im Zeit- als auch im Frequenzbereich durchgeführt. Verschiedene Randbedingungen wurden auf einzelnen Quadranten angewendet, um die elektrischen Eigenschaften der Spulen zu untersuchen. Ein weiteres vereinfachtes Modell, das eine einzelne Quadrantenspule im Rogowski-BPM beschreibt, wurde unter der Annahme einer 2D Geometrie entwickelt. In dieser Analyse wurden die Impedanz und Induktivität der einzelnen Spule über einen Frequenzbereich von 10MHz untersucht.
Mehrere Hardware-Entwicklungen und Verbesserungen, ausgehend von einer einfachen Ringspule bis hin zum kompletten BPM mit seinen Durchführungen, Flanschen und Steckern wurden erreicht. Entwicklungen am Laborprüfstand ermöglichten genauere Kalibrierungen. Mit Hilfe der neu entwickelten zylindrischen Messerkantenstruktur wurde das Verhalten der Schrittmotorantriebe mit einem Lasertracker untersucht, und eine absolute BPM-Kalibrierung (mit einer Genauigkeit von wenigen Mikrometern) ist nach dem Einbau der BPMs im Beschleuniger möglich. Die Kalibrierungsmessung für das Rogowski-BPM wurde am Prüfstand durchgeführt und mit dem theoretischen Modell verglichen. Es wurde eine gute Übereinstimmung zwischen den Messergebnissen und den theoretischen Erwartungen wurde erreicht.
Im Labor wurden verschiedene experimentelle Untersuchungen durchgeführt, wie die Messung des Frequenzganges, die Messung des Positionsverhalten, Vermessung der Stabilität der Resonanzkurven, sowie der Abstimmung der Resonanzkurven mit Shunt Kondensatoren, die Messung der zeitlichen Variationen der elektrischen Signale, sowie die Auswirkung der Wellenform der Anregungsquelle auf die BPM-Kalibrierung, die Möglichkeit der Verwendung des BPMs als BCT[11] und die Verteilung des Signal-Rausch-Verhältnisses (SNR). Darüber hinaus wurde der Einfluss der geometrischen Spezifikationen der Wicklungen, die Art und Weise, wie die gesamte Schaltung angeschlossen ist, und die Eigenresonanzfrequenz (SRF) des Systems auf die Positionsauflösung bei verschiedenen Frequenzen ebenfalls untersucht.
Zwei Rogowski-BPMs mit unterschiedlichen geometrischen und elektrischen Eigenschaften wurden entwickelt und erfolgreich in COSY installiert und getestet. Die Installation erfolgte am Ein- und Ausgang des Hochfrequenz-Wien-Filters (RF WF). Die Ergebnisse von lokalen Orbit Bumps, die um den RF WF herum eingeführt wurden, zeigten angemessene und lineare Positionsantworten die von den beiden BPMs gemessen wurden.
Mit den Rogowski-BPMs konnte eine Auflösung von bis zu 400 nm erreicht werden (für eine einzelne Position, gemessen mit einer Abtastrate von 750 kHz während einer Abtastzeit von 1s, einer SRF des Systems von $3,229$ MHz und einer Teilchenintensität von 5×10^9). Dies entspricht einer Verbesserung der Auflösung um eine Größenordnung im Vergleich zu typischen kapazitiven BPMs, die in COSY eingesetzt werden. Darüber hinaus wird mit dem neu vorgeschlagenen Verfahren zur absoluten Gerätekalibrierung, und unter Berücksichtigung der Genauigkeit der Schrittantriebe, die für die Kalibrierung verwendet werden, sowie der Fehler, die durch zeitliche Drifts verursacht werden, erwartet, dass die Genauigkeit der Rogowski-BPMs bei etwa 20 µm (Fehler von

[11] **B**eam **C**urrent **T**ransformer.

drei Standardabweichungen, was einem um 1 cm dezentrierten Strahl entspricht), was einer Verbesserung um den Faktor fünf im Vergleich zu typischen BPMs.

Chapter 1

Introduction

One of the most evident features of our visible universe is the absence of antimatter. The huge imbalance between observed matter particles e.g. protons, electrons and neutrons and their antimatter counterparts is rated as one of the biggest puzzles in cosmology. In physical cosmology, this is also known as the matter-antimatter asymmetry. It is believed that the big bang must have created an equal amount of matter and antimatter, that in turn annihilated each other once they got in contact producing photons, however, some of this matter has survived the annihilation (about one out of every billion) creating the universe we live in today [1]. Why did matter and not antimatter survive?

1.1 Fundamental symmetries

Symmetry or invariance is one of the main concepts in physics. A physical system is expected to be preserved under the application of some symmetric transformations. In fact, understanding a system can be made much simpler when symmetries are utilized. Symmetries are privately connected with conservation laws, meaning, a symmetry of a system implies at the same time the existence of some conserved quantity or law. For example, for a system which is isolated and free of any external forces, the total energy should be the same under the operation of translation of the system in space, which also implies a conservation of linear momentum as the net force is zero. Together with conservation laws (which are not absolute), symmetry has been considered the backbone of high-energy physics [2]. The next subsections introduce three different types of discrete symmetries: parity, time reversal and charge-conjugate.

1.1.1 Parity

The operation of parity $\mathcal{P}$ implies an inversion in the spacial coordinates [2,3] such as $x, y, z \xrightarrow{\mathcal{P}} -x, -y, -z$. If parity is conserved, the laws of physics should apply equally when the system is viewed in its mirrored or inverted coordinates, where left becomes

right and right becomes left or up becomes down and down becomes up. Otherwise, if the parity is violated, then the two systems (original and mirror-reflected) should become distinguishable. While parity is proved to be conserved in both strong and **E**lectro-**M**agnetic (EM) interactions, it is maximally violated in the weak sector. As an example, applying parity transformation on the neutrinos which are found to be left handed (where particle spins in an opposite direction to its momentum) results in a reversed momentum direction while spin (which under parity operation should remain the same) is left unchanged, by this, a right handed neutrino which, in fact, does not exist in nature is produced (see figure 1.1, upper right panel).
The first parity violation in weak interactions [4,5] was discovered in 1956 during the experiment carried by Chien-Shiung Wu using a sample of Cobalt ^{60}Co nuclei which undergoes the decay:

$$^{60}\mathrm{Co} \rightarrow {}^{60}\mathrm{Ni}^{*} + e^{-} + \bar{\nu}_{e}\,. \tag{1.1}$$

The radioactive sample of ^{60}Co was employed inside a solenoidal magnetic field at a temperature of 0.01 K. It was expected that if parity is symmetric then the intensity of e^{-} particles emitted with an angle θ or $\pi - \theta$ with respect to the direction of Cobalt nuclear spin must be equally probable. However, it was surprisingly seen that the electrons were preferentially emitted anti-parallel to the nuclear spin of parent ^{60}Co, which clearly indicates a parity violation.

1.1.2 Charge-conjugation

The operation of Charge-conjugation ($\mathcal{C}$) transforms a particle into its anti-particle counterpart [6] which means an opposite sign for the charge and magnetic moment, however it leaves unchanged both the spin and spacial direction (momentum) of the particle. Similar to parity transformation, the Charge-conjugation is conserved in strong and EM sectors but not in the weak interactions. Under $\mathcal{C}$ operation, a left-handed neutrino will turn into a left-handed antineutrino which in fact is not seen in nature (see figure 1.1, lower left panel). An example of conservation of $\mathcal{C}$ is the EM interaction [2]:

$$\pi^{0} \rightarrow \gamma + \gamma\,, \tag{1.2}$$

where $\mathcal{C}$ is symmetric in both initial and final states ($\mathcal{C}$ for π^{0} is $+1$ and $\mathcal{C}$ in the final state is $(-1)^{2}$)*. While a decay like:

$$\pi^{0} \rightarrow \gamma + \gamma + \gamma \tag{1.3}$$

is forbidden by EM interaction, as clearly it violates $\mathcal{C}$.

1.1.3 Time reversal

The operation of time reversal ($\mathcal{T}$) implies an inversion in the direction of time [7], simply as $t \xrightarrow{\mathcal{T}} -t$ which also corresponds to a reversal of motion (momentum) as well as in

*The photons have -1 eigenvalue under $\mathcal{C}$ operation and the power of two because $\mathcal{C}$ is multiplicative.

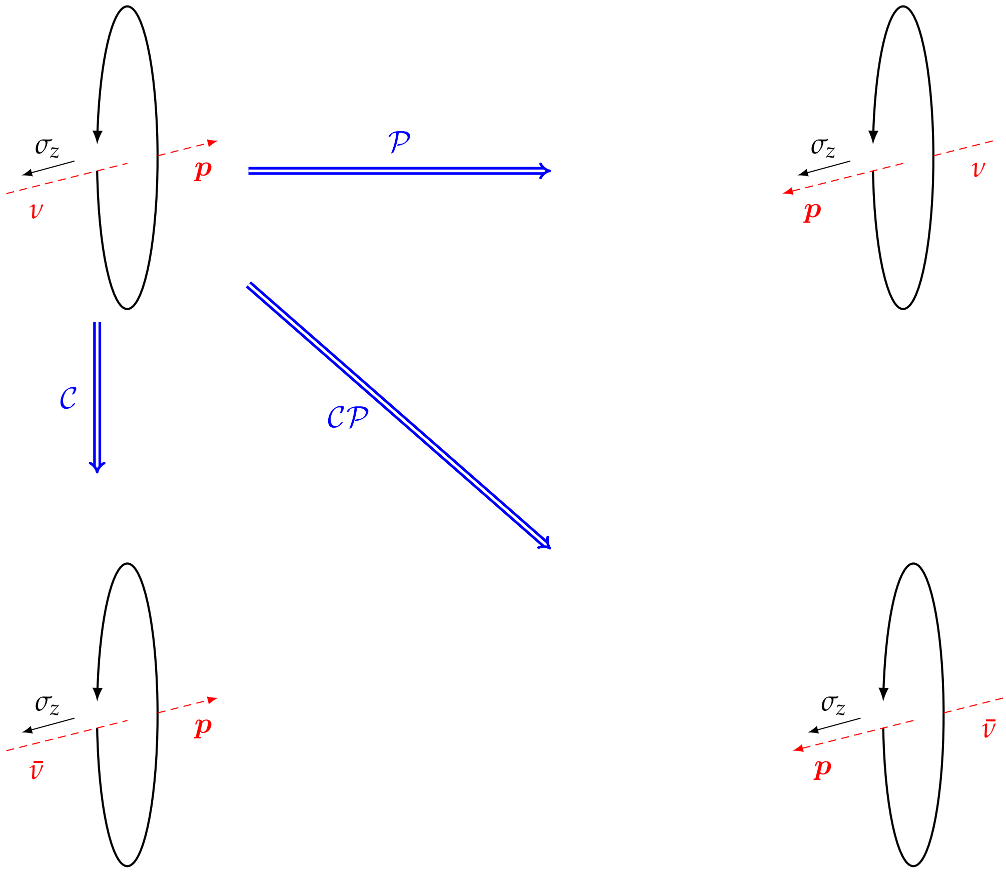

Figure 1.1: Left-handed neutrino with spin direction opposite to the neutrino's momentum direction (upper left). Applying parity on the particle's state in the upper left panel results in a right-handed neutrino which does not exist (upper right). Applying charge-conjugation on the particle's state in the upper left panel produces a left-handed anti-neutrino which does not exist (lower left). Applying both parity and charge-conjugation on the particle's state in the upper left panel produces a right-handed anti-neutrino, which exists (lower right). The dashed red vectors represent the particle's momentum direction $\boldsymbol{p}$. The solid black vectors represent the z-component of the particle's spin direction σ_z. The blue arrows are to guide the eye to the applied transformation.

spin directions and leaving the spacial coordinates unchanged. A consequence of having the time reversal to be invariance is whenever the direction of time is reversed then laws of physics should be the same for both forward and backward reactions, or in simpler words, the reaction $X \to Y$ and $Y \to X$ should have equal rates or probabilities of occurrence. Time reversal holds good in the strong and EM interactions but not in the weak sector. A direct indication for the asymmetry in time reversal in the weak interactions was demonstrated by the neutral K mesons [8] through the reaction:

$$K^0 \rightleftharpoons \bar{K}^0 \,. \tag{1.4}$$

The asymmetry of the two reversed reactions (difference in rates) was calculated by:

$$A = \frac{R(\bar{K}^0 \to K^0) - R(K^0 \to \bar{K}^0)}{R(\bar{K}^0 \to K^0) + R(K^0 \to \bar{K}^0)} \,. \tag{1.5}$$

The degree of $\mathcal{T}$ violation calculated through this asymmetry was found to be in the per-mill level.

1.1.4 Charge-conjugate parity

Charge-conjugate parity is the combined operation of charge-conjugate and parity ($\mathcal{CP}$) where particles are replaced with their anti-particles in mirrored coordinates. Although weak interactions were proven to separately violate $\mathcal{C}$ and $\mathcal{P}$ symmetries, it was still believed until 1964 that the combined $\mathcal{CP}$ is conserved in the weak sector (see figure 1.1, lower right panel). However, it came out in that year through the Cronin experiment that the decay of long lived neutral kaons did not respect the $\mathcal{CP}$ symmetry [3,8,9]. These long lived kaons usually decay through:

$$K_L \to 3\pi \,. \tag{1.6}$$

Where in the above equation†, the operation of $\mathcal{CP}$ implies an eigenvalue of -1. However, it was also seen that K_L particles also undergo the reaction:

$$K_L \to 2\pi \,, \tag{1.7}$$

with some per-mil probability. The above decay‡ corresponds to a $+1$ eigenvalue under the operation of $\mathcal{CP}$, which is clearly addressing $\mathcal{CP}$ violation in weak interactions.
According to the universal $\mathcal{CPT}$ theorem, which is symmetric as far as we know, all types of interactions are invariant under the successive operation of $\mathcal{C}$, $\mathcal{P}$ and $\mathcal{T}$, carried in any order. By $\mathcal{CPT}$, an invariance in $\mathcal{T}$ would also violate $\mathcal{CP}$ symmetry (similarly an asymmetry in $\mathcal{P}$ means $\mathcal{CT}$ violation). Although the **S**tandard **M**odel (SM) expected $\mathcal{CP}$ violation but to a very small extent that unfortunately fails to explain the baryon asymmetry in the universe (see next section).

1.2 Asymmetry in universe

According to the big bang theory, in the very early stage of the universe when the thermal energy per particle was larger than hadron masses, baryons, anti-baryons and photons

†The three pions are either $\pi^0\pi^0\pi^0$ or $\pi^0\pi^-\pi^+$

‡The two pions are either $\pi^0\pi^0$ or $\pi^-\pi^+$

were all in thermal equilibrium, being created and destroyed through reversible reactions. Eventually, when expansion proceeds and temperature decreases, the rate of production of new pairs becomes smaller than the expansion rate, or in other words, photons will no longer produce enough nucleon pairs, neither can nucleons find enough counterparts with which to annihilate. At this critical temperature which happens at the so-called freeze-out stage, the expected ratio for baryon and anti-baryon densities with respect to photon density[§] is [1,2]:

$$\eta = \frac{N_B}{N_\gamma} = \frac{N_{\bar{B}}}{N_\gamma} \approx 10^{-18} . \tag{1.8}$$

And because the universe is expanding and subsequent to the freeze-out stage, the above ratio should hold true until today. However, the current observation of the ratio between density of baryons and that of microwave photons is:

$$\eta = \frac{N_B - N_{\bar{B}}}{N_\gamma} \approx \frac{N_B}{N_\gamma} \approx 10^{-9} . \tag{1.9}$$

The above relation implies that for each 10^9 anti-baryons there were $10^9 + 1$ baryons, and considering annihilation, a residue of only one baryon particle must have created the current universe. The big bang theory gets the baryon number wrong by a factor of 10^9, assuming equal amounts of baryons and anti-baryons originally produced, i.e. an initial baryon number of zero. In 1967 A. Sakharov postulated in a paper widely quoted nowadays, three main prerequisites for generating such an asymmetry in baryons after the big bang with $\mathcal{C}$ and $\mathcal{CP}$ violating processes as one of these three main conditions [10,11]:

- baryon-number violating processes
- non-equilibrium state during expansion
- $\mathcal{C}$ and $\mathcal{CP}$ violation

Sources for $\mathcal{CP}$ violation in the SM correspond to a baryon asymmetry of:

$$\eta \approx 10^{-20} , \tag{1.10}$$

which is way too small to explain the observed ratio in eq. (1.9). This means that new sources for $\mathcal{CP}$ violation and new physics beyond the SM are needed in order to understand the observed baryon asymmetry (see next section).

1.3 Electric dipole moment

The electric dipole moment (EDM) of a subatomic particle arises from an asymmetry in the spacial distribution of the charge (carried by e.g. the quarks for a hadron) relative to

§Densities are in units of particles per unit volume the spin axis ($\boldsymbol{S}$). In analogy to the Magnetic Dipole Moment (MDM) of a particle which is given by:

$$\boldsymbol{\mu} = g\frac{q\hbar}{2m}\boldsymbol{S}\,, \tag{1.11}$$

the EDM of a particle is defined as:

$$\boldsymbol{d} = \eta\frac{q\hbar}{2mc}\boldsymbol{S}\,, \tag{1.12}$$

with q and m for the particle's charge and mass, respectively. The dimensionless quantity η denotes the strength of the electric dipole, and similarly, for the strength of magnetic dipole the dimensionless g factor is used. For a particle in the presence of an EM field, the Hamiltonian can be expressed as:

$$\hat{\mathcal{H}} = -\boldsymbol{d}\cdot\boldsymbol{E} - \boldsymbol{\mu}\cdot\boldsymbol{B}\,. \tag{1.13}$$

Under parity and time reversal transformations, the Hamiltonian reads [12]:

$$\mathcal{P} : \hat{\mathcal{H}} = +\boldsymbol{d}\cdot\boldsymbol{E} - \boldsymbol{\mu}\cdot\boldsymbol{B}\,, \tag{1.14}$$

$$\mathcal{T} : \hat{\mathcal{H}} = +\boldsymbol{d}\cdot\boldsymbol{E} - \boldsymbol{\mu}\cdot\boldsymbol{B}\,. \tag{1.15}$$

Applying $\mathcal{P}$ inverts the direction of electric field $\boldsymbol{E}$ leaving the magnetic field $\boldsymbol{B}$ and the spin (implicitly in $\boldsymbol{d}$) directions unchanged. While applying $\mathcal{T}$ inverts both magnetic field $\boldsymbol{B}$ and spin directions leaving electric field direction unchanged. Therefore, a permanent EDM violates both parity and time reversal symmetries [13–15], and also $\mathcal{CP}$ which makes it a perfect candidate for physics beyond SM.

1.4 Searches for EDM in storage rings

The history of the search for a particle's EDM has started over 60 years ago. Many measurements on subatomic or composite particles' EDM had already been done [16]. The latest experimental limit for the neutron EDM is 1.8×10^{-26} e cm [17]. The basic principle of storage rings EDM searches relies on studying the interaction between the particle's spin and the electric field. Different approaches for the search of EDM in storage rings have been investigated by considering purely electric, purely magnetic or combined E/B rings. In the following, a brief description for the method of magnetic machine with a **R**adio **F**requency (RF) Wien filter will be given.
The ***J****ülich* ***E****lectric* ***D****ipole moment* ***I****nvestigations* (JEDI) collaboration [18] aims at a first direct measurement of charged particle EDM for protons and deuterons using the **CO**oler **SY**nchrotron (COSY) accelerator facility located at the Forschungszentrum Jülich in Germany. In general, for a particle in the presence of the ring's electric and magnetic fields, the spin evolution is governed by the famous Thomas Bargmann Michel Telegdi (T-BMT) equation [19]:

$$\frac{d\boldsymbol{S}}{dt} = \boldsymbol{S}\times\boldsymbol{\omega}\,, \tag{1.16}$$

with the total angular velocity $\boldsymbol{\omega}$ defined as (for $\boldsymbol{E}$ and $\boldsymbol{B}$ fields perpendicular to the momentum direction):

$$\boldsymbol{\omega} = -\frac{e\hbar}{mc}\left[G\boldsymbol{B} + \left(G - \frac{1}{\gamma^2 - 1}\right)\boldsymbol{E}\times\boldsymbol{v} + \frac{\eta}{2}\left(\boldsymbol{E} + \boldsymbol{v}\times\boldsymbol{B}\right)\right], \tag{1.17}$$

where G is the anomalous magnetic moment ($\frac{g-2}{2}$), γ is the relativistic Lorentz factor and $\boldsymbol{v}$ is the particle's velocity. However, for a magnetic ring (like COSY), the upper equation becomes:

$$\boldsymbol{\omega} = -\frac{e\hbar}{mc}\left[G\boldsymbol{B} + \frac{\eta}{2}\boldsymbol{v}\times\boldsymbol{B}\right]. \tag{1.18}$$

Assuming an initially polarized beam along the longitudinal axis and a vertical magnetic field, the first term results in a horizontal spin precession (due to the effect from the magnetic dipole moment) while the second term, which arises from the EDM effect, results in a spin precession in the vertical plane (observe the cross product in eq. 1.16). In fact, oscillations caused by the EDM term are very small compared to those caused by the MDM term. It is possible to turn the vertical oscillations into a macroscopic measurable signal over time if an RF Wien filter is used [20–23]. An RF Wien filter device provides vertical magnetic and radial electric fields under the condition that the total Lorentz force acting on particles is zero. To maximize the spin response, the RF Wien filter is operated on resonance with the spin precession frequency:

$$f_{\mathrm{RF}} = f_{\mathrm{rev}}|k + \nu_s|, \tag{1.19}$$

with f_{rev} denotes the revolution frequency, K is an integer that represents the harmonic number and ν_s is the spin tune. For a purely magnetic ring, the build-up of vertical polarization (S_{v}) over time due to the presence of EDM when the RF Wien filter is used can be approximated to the first order [21]:

$$\left(\frac{dS_{\mathrm{v}}}{dt}\right)_{\mathrm{EDM}} = \eta P_0 \frac{q^2 B_{\mathrm{Wien}}}{(2mc)^2}\frac{1+G}{\gamma^2}\frac{\beta B_{\mathrm{v}}}{\nu_s \omega_{\mathrm{rev}}}, \tag{1.20}$$

where P_0 is the amplitude of the initial polarization, c is the speed of light, ω_{rev} is the angular revolution frequency, β is the relativistic velocity and B_{v} is the ring's vertical magnetic field. In the above relation, an approximation is made based on a zero phase shift between the Wien filter RF fields and the spin rotations.

A precision experiment as the search for the EDM, requires a very high control of systematics. For instance, a fake EDM signal can be easily generated by a radial magnetic field, misalignment in quadruples or an orbit RMS¶ deviated from zero. In [24], the effect of deviation of the vertical orbit RMS generated by simulating some random vertical quadruple shifts on the change in the vertical spin component was investigated. A change of 1.6 mm or greater in the vertical orbit RMS would produce a change in the vertical

¶Root Mean Square.

spin build-up in the order of 10^{-9} which is, indistinguishable from a true existing EDM with $\eta = 10^{-4}$. In fact, this does not solely highlight the importance of having accurately aligned magnetic elements, but also the absolute accuracy of the **B**eam **P**osition **M**onitors (BPMs) themselves. The existing BPMs equipped in the COSY ring offer a resolution down to few µm (assuming a total of 4096 data entries) for a particle beam with intensity in the order of 10^{10} [25], however, their accuracy can be much worse. A recent upgrade should bring their accuracy down to the level of 100 µm. These capacitive BPMs (where position determination of the charged-particle beam results from the coupling between the device capacitive plates and electric field accompanying the beam) are relatively big in size, installation of such BPMs requires a minimum free space of about 50 cm.
As a step towards improving the BPM system for our EDM experiments, a new type of compact (insertion factor of about 10 cm) Rogowski BPMs has been developed. With these inductive Rogowski BPMs, a resolution down to about 400 nm is possible (for one position measurement assuming integration time of 1 s and a beam intensity of around 5×10^9). However, their expected accuracy is around 20µm. The aim of this thesis is to provide hardware developments in building and testing Rogowski BPMs. Different improvements of these inductive BPMs are presented. Experimental efforts have been carried out in developing a dedicated laboratory test-stand to perform calibrations before installation into COSY. In addition, this thesis aims at providing a better understanding for this new system of position monitoring and its possible limitations.

1.5 Organization of the thesis

The structure of this thesis is is organized as follows.
In chapter 2, an extension to the theoretical model that describes induction signals is presented based on the lumped model approximation. Effects from the EM coupling between nearby coils are considered. The sensitivity to beam coordinates is investigated based on different winding configurations. Furthermore, the impact of incomplete winding angular coverage is also introduced.
In chapter 3, EM simulations carried out within COMSOL Multiphysics on the transient response from a simple model of the Rogowski BPM are given. Investigations carried in the frequency domain on the electrical parameters of a single quadrant coil are also discussed.
Chapter 4 provides the experimental realization of the Rogowski BPM, how its signal is processed and how the system is calibrated. A description of the hardware development of the device assembly, the laboratory test-stand and the vacuum chamber test-stand is also depicted.
Results from experiments carried out in the laboratory are introduced in chapter 5. The frequency response, the position response, temporal changes and effects from the signal wave form on the device calibration, are all given. The validation of the developed theoretical model in the results from the calibration measurement is introduced.
Chapter 6 provides the commissioning results of the Rogowski BPMs in the accelerator facility COSY. Results of the BPM response after application of local orbit bumps are

given. Changes of the BPM's readouts over time, or as a result of some nearby changes in the ring as the rotation of the RF Wien filter, are also elaborated. The effect of number of bunches per beam on returned positions is also discussed.
In chapter 7, a discussion for the results and an insight into needed future developments is presented.

Chapter 2

Theory

This chapter will introduce the theoretical background for the induction signals from the Rogowski BPM. The use of the lumped model approximation in describing the output signals (measured signals) will be given. Effects from the electromagnetic coupling between the single quadrants and from the windings' incomplete angular range on the voltage responses are also described.

2.1 Principle of Rogowski coil

A Rogowski coil is a special type of helical wire wound around a non-magnetic torus (see Figure 2.1 panel (a)). It was named after the German physicist Walter Rogowski (1881-1947) who bridged the gap between theoretical physics and applied technology in numerous areas of electronics [26]. As common induction sensors, the principle of the Rogowski coil signal can be explained by Faraday's law of electromagnetic induction [27–29] (also known as Maxwell-Faraday law) which states that a time varying magnetic flux density $\mathbf{B}(t)$ gives rise to a time changing non-conservative electric field $\mathbf{E}(t)$ [30]:

$$\nabla \times \mathbf{E}(t) = -\frac{\partial \mathbf{B}(t)}{\partial t}\,. \tag{2.1}$$

In our case, the time changing magnetic flux is originated from the particles' beam [31]. Consider the Rogowski BPM in Figure 2.1. with an alternating beam current going along the $\mathbf{z}$ direction (normal to the plane of the page). The transient current results in the formation of circulating transient magnetic fields around the Rogowski conductive domains. This is stated by Ampere's law [32] as:

$$\mu_0 \mathbf{I}(t) = \oint \mathbf{B}(t) \cdot d\mathbf{l}\,, \tag{2.2}$$

where the right hand side of eq. (2.2) represents a line integral for a closed curve (an arbitrary curve in the direction of helical winding) that encircles the beam current $\mathbf{I}(t)$, d$\mathbf{l}$ is a small element length of this curve. μ_0 is the magnetic permeability for vacuum. Whenever an electric field existed, an accompanying electric potential $V(t)$, or voltage difference exists as well. By using the relation [33]:

$$V(t) = -\oint \mathbf{E}(t) \cdot d\mathbf{l}\,, \tag{2.3}$$

where the integral is again over a closed loop, together with eq. (2.1) and applying Stoke's theorem we arrive at:

$$V(t) = -n\frac{\partial \Phi(t)}{\partial t}\,. \tag{2.4}$$

$\Phi(t)$ is the magnetic flux which represents the integral sum of all magnetic field lines passing through the surface domain of the Rogowski coil. n is the Rogowski turn number. It is important to mention that both $V(t)$ and $\mathbf{E}(t)$ exist whether or not the circuit was closed, i.e. induced voltage and induced electric fields are formed even if the coil's terminals were open ended (when the induced current does not flow). Another very important remark is, that the magnetic flux $\Phi(t)$ should represent the net magnetic flux around the Rogowski surface, meaning that it includes a contribution from the primary flux coming from the beam current, the induced flux if the coil's terminals were closed ended (which should be directed in an opposite direction to the primary), the induced flux as a result from the presence of a time changing electric field [34] as well as that is originated from any coupling between nearby domains.
Now that was a general description for induction in a Rogowski coil and how it explains the presence of an induced voltage signal. The next sections, present more about the Rogowski as a BPM and the measurement of the voltage signal induced between wire terminals of a single Rogowski BPM quadrant and how it links to the main mission of the device as a monitor for delivering beam coordinates.

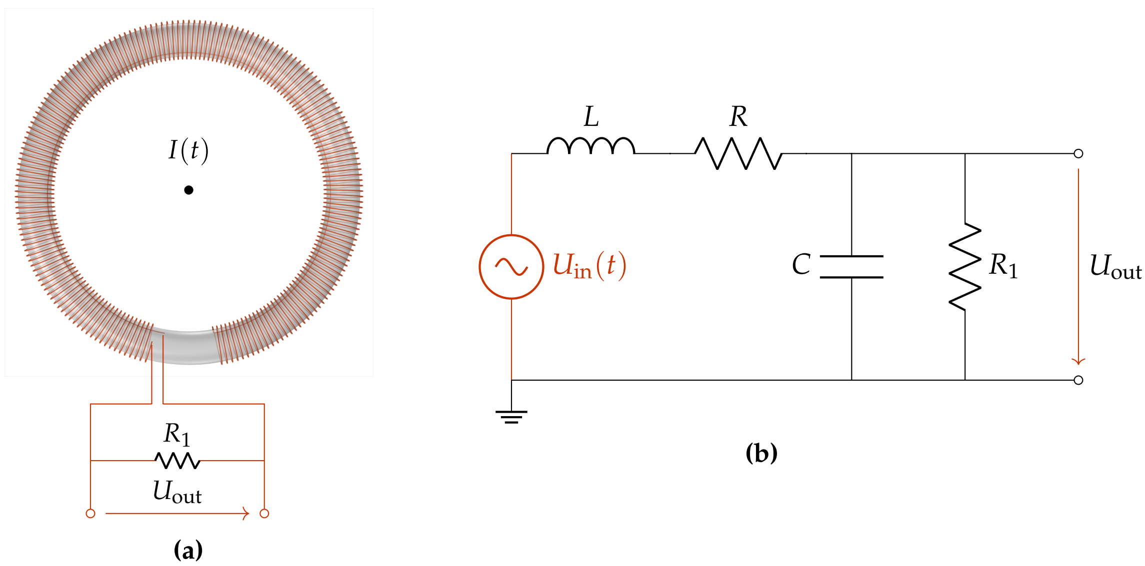

Figure 2.1: Realization of the typical Rogowski winding used for sensing a current $I(t)$ and how its output signal results (a). Equivalent circuit for the induced voltage measurement using the lumped elements (R, L and C) approximation. U_{in} is the induced signal, U_{out} is the measured one and R_1 is the input impedance of the measuring device (b).

2.2 Rogowski coil as BPM

Taking the winding of a typical Rogowski coil, as illustrated in figure 2.1, a way to relate the induction signal to the beam positions can be made by splitting the full helical geometry into further equal but electrically disconnected parts. One possibility is to segment the domain into four quadrants (see Figure 2.2), where the combination of the four voltages can be linked to a position of the inducing current in the xy-plane.

The Rogowski BPM elaborated throughout this thesis has the four-segment configuration as illustrated in Figure 2.2. A PEEK (Polyetheretherketones) core is used in order to provide mechanical stability for the winding. The choice of PEEK, which is a non-ferromagnetic (with relative permeability of 1), for the core material is referred to the highly linear response* resulting from the absence of magnetic saturation. Another advantage of using PEEK plastic in particular and not other types of polymers as the VESPEL for instance † is vacuum compatibility, where in the latter, the out-gassing rate is about five times higher than in the case of PEEK [35]. The PEEK core has the geometrical parameters of $R = 58.625$ mm and $2a = 12.75$ mm representing the torus central radius and height, respectively (see figure 2.2). The selection of these parameters is to ensure

*Here, the term linear describes the relation between the beam current amplitude and the power or the output voltage signal measured from a Rogowski quadrant.

†VESPEL was used in some former time as a core material.

a reasonable and accessible position measurement in the COSY ring that has a tube diameter of 150 mm [36] and a typical beam size [37,38] of around 7 mm and around 3 mm for the horizontal and vertical bunch widths, respectively[‡]. On the surface domain of each quarter of the core, holes are drilled in order to provide a path for the wire return loops that go in an opposite direction to the advancement of each coil's windings to help in cancellation of unwanted magnetic fields. The windings are made of a copper wire with a kapton insulation. The wire diameter plays an important role in defining the coil's electrical features (e.g. inductance, resistance and capacitance) as well as the desired operational bandwidth [§].

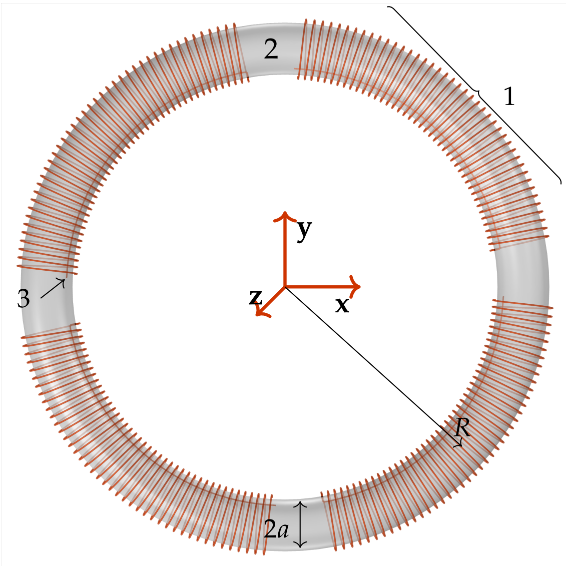

Figure 2.2: Winding of a Rogowski BPM viewed in the xy-plane. The z vector points to the beam direction. The labels 1, 2 and 3 are representing the single quadrant coil 1, the PEEK core and the winding return loop, respectively. R (58.625 mm) indicates the torus central radius and $2a$ (12.75 mm) indicates its height. For the naming of the remaining quadrants (2 to 4), follow a clockwise order with respect to quadrant coil 1.

[‡]The widths represent the three standard deviations of a Gaussian beam after cooling, however, this size can be as big as 20 mm before the cooling process.

[§]Assuming the fixed core dimensions, selecting some diameter for the wire will be limited with the physical surface on a quarter circumference, this will influence the total possible number of windings which is an important parameter in defining the coil's inductance and hence the frequency operational bandwidth.

2.3 Measurement of induced voltage

2.3.1 Induced voltage

For a single Rogowski quadrant coil (take quadrant number one in the upper right plane of Figure 2.2) with n windings, the voltage induced between the wire terminals originated from a sinusoidal beam current with an amplitude I and an angular frequency ω is [39]:

$$\begin{aligned} U_{\text{in}1}(x, y, \omega) = \; & n\mu_0 c_0 \omega I \Big[1 + c_1(x+y) + c_2(xy) + c_3(-x^3 - y^3 + 3yx^2 + 3xy^2) \\ & + c_5(x^5 + y^5 - 10x^3y^2 - 10y^3x^2 + 5y^4x + 5x^4y) \Big] . \end{aligned} \tag{2.5}$$

Where x and y denote the beam positions in the transverse plane (typically in mm). The c terms[¶] are constants that depend on the coil's geometry (see Appendix A). Because of symmetry, the expressions for induced voltages from remaining quadrant coils are:

$$\begin{aligned} U_{\text{in}1}(x, y, \omega) \quad & = U_{\text{in}2}(x, -y, \omega) \\ & = U_{\text{in}3}(-x, -y, \omega) \\ & = U_{\text{in}4}(-x, y, \omega) . \end{aligned} \tag{2.6}$$

The expression in eq. (2.5) represents only the induced signal. Details on the measured induced signal are presented in the next subsection.

2.3.2 Measured voltage

For the measurement of the induced signal, the lumped model can be used to derive the value of the voltage signal at the input of the measuring device. Figure 2.1 (b) shows an equivalent circuit of the Rogowski voltage measurement using the lumped elements R, L and C which can be also used to describe the case of a single quadrant voltage measurement. L represents the quadrant's inductance, R is its resistance and C is the capacitance from the quadrant coil plus that from measurement cables connected with coil's terminals. The inductance L of a toroidal coil, with a circular cross section [40–42] and n windings is directly proportional to the turn number squared:

$$L \propto n^2 . \tag{2.7}$$

With a constant of proportionality that depends on the coil's geometry. The capacitance C represents the self capacitance from the Rogowski coil segment plus the external capacitance, mainly from the cables in the measurement (where cables are conceived as parallel external capacitors). The coil's capacitance includes the capacitance between individual windings in a single toroidal layer (relatively very small as these windings are in serial connections with each other), that between windings and the returning loop

¶They have a unit of $(\text{mm})^{-m}$ with m for the degree of the polynomial that the c term is multiplied by.

and the capacitance from twisted wire extensions that goes through the way between the end of coil windings and the RF coaxial cable which is normally used for analog signal transmission. Following the transfer function derivations given in appendix A (see eq. A.3), a general expression for the measured induced voltage signal from a single Rogowski quadrant can be stated as:

$$U_{\text{out}} = \gamma(\omega_0, \omega_1, \omega) U_{\text{in}}\,, \tag{2.8}$$

which reads for the quadrant number one:

$$\begin{aligned} U_{\text{out1}}(x, y, \omega) = \ & \gamma(\omega_0, \omega_1, \omega) n \mu_0 c_0 \omega I \Big[1 + c_1(x + y) + c_2(xy) + c_3(-x^3 - y^3 + 3yx^2 + 3xy^2) \\ & + c_5(x^5 + y^5 - 10x^3y^2 - 10y^3x^2 + 5y^4x + 5x^4y) \Big]\,. \end{aligned} \tag{2.9}$$

Where ω_0 (resonance angular frequency) and ω_1 are constants that depend on the lumped elements' values (R, L and C. See appendix A).

2.4 Coupling between single quadrants

The previous section explained the measured voltage signal from a single quadrant based solely on the interaction with the beam signal. However, possible contribution to the voltage signal of the Rogowski quadrant can be coming from the interaction with nearby quadrant coils. This latter interaction can be explained as a mutual coupling between nearby coils [43] where a current running in an ith coil will produce a voltage signal in a jth nearby coil. It is also the same basic principle as that with how the quadrant itself interacts with the beam current. That was how one can explain this interaction in general, but in fact it is a special type of unintentional interference at the same time, this is because the Rogowski single quadrants are manufactured for a different purpose where the quadrant itself is not excited with a signal, for this reason it is more accurate in this context to say where a "flux changing in the ith quadrant produces a voltage in the jth nearby quadrant".

This cross-talk effect between the quadrants is reduced to its minimum when the beam is exactly centered, whereas, when the beam is deviated from the center (especially when closest to one particular quadrant) the effect gets visible. Furthermore, the existence of manufacturing variations between separate quadrants is possible which results in making this interference more clear. To quantify the effect of the coupling between quadrants, the coefficient of coupling k which equals the mutual inductance between any two quadrants (out of the four) divided by the square root of the product of their self inductances [44] can be used. But this of course requires deriving an analytical formula for the mutual inductance based on the existing size and geometry. One other easier and straight-forward method will be using the results from eqs. 2.4 and 2.5 in addition to the pure definition of the coupling factor. This factor k varies between 0 and 1 depending on the amount of flux originally produced in a quadrant i and possibly hitting the surface domain of a quadrant j. This should imply that a value of unity means that all flux lines originated in the ith quadrant will also be passing through the surface of the jth near quadrant. For the existing geometry of the Rogowski BPM, this coupling should be small, especially at frequencies well below the resonance. Now let us again explain how the earlier mentioned two equations (eqs. 2.4 and 2.5) can help quantifying the voltage contribution from coupling between individual quadrants. Eq. (2.4) states that the voltage induced should be proportional to the time derivative of the magnetic flux. In fact, what we see as a result of the time derivative in eq. 2.5 is the ω which resulted from deriving the sinusoidal beam current with respect to time. This should mean that we already know the formula of the magnetic flux through any surface (which should be the expression in eqs. 2.5 and 2.6 without the ω term). This reads for quadrant 1:

$$\begin{aligned}\Phi_1(x,y,t) = \; & \mu_0 c_0 I(t) \Big[1 + c_1(x+y) + c_2(xy) + c_3(-x^3 - y^3 + 3yx^2 + 3xy^2) \\ & + c_5(x^5 + y^5 - 10x^3y^2 - 10y^3x^2 + 5y^4x + 5x^4y) \Big] \, . \end{aligned} \tag{2.10}$$

This will enable modifying eq. (2.9) into a more general form with voltage contribution from interference between quadrants (simply as $-nk\frac{\partial\Phi(t)}{\partial t}$) included :

$$\begin{aligned}U'_{\text{out1}}(x,y,\omega) = \; & \gamma(\omega_0,\omega_1,\omega) \Big[U_{\text{in1}}(x,y,\omega) + k_{12} U_{\text{in2}}(x,y,\omega) \\ & + k_{13} U_{\text{in3}}(x,y,\omega) + k_{14} U_{\text{in4}}(x,y,\omega) \Big] \, . \end{aligned} \tag{2.11}$$

Similarly for the remaining three quadrants:

$$\begin{aligned}U'_{\text{out2}}(x,y,\omega) = \; & \gamma(\omega_0,\omega_1,\omega) \Big[U_{\text{in2}}(x,y,\omega) + k_{21} U_{\text{in1}}(x,y,\omega) \\ & + k_{23} U_{\text{in3}}(x,y,\omega) + k_{24} U_{\text{in4}}(x,y,\omega) \Big] \, , \end{aligned} \tag{2.12}$$

$$\begin{aligned}U'_{\text{out3}}(x,y,\omega) = \; & \gamma(\omega_0,\omega_1,\omega) \Big[U_{\text{in3}}(x,y,\omega) + k_{31} U_{\text{in1}}(x,y,\omega) \\ & + k_{32} U_{\text{in2}}(x,y,\omega) + k_{34} U_{\text{in4}}(x,y,\omega) \Big] \, , \end{aligned} \tag{2.13}$$

$$\begin{aligned}U'_{\text{out4}}(x,y,\omega) = \; & \gamma(\omega_0,\omega_1,\omega) \Big[U_{\text{in4}}(x,y,\omega) + k_{41} U_{\text{in1}}(x,y,\omega) \\ & + k_{42} U_{\text{in2}}(x,y,\omega) + k_{43} U_{\text{in3}}(x,y,\omega) \Big] \, . \end{aligned} \tag{2.14}$$

With the unit-less coupling factor k_{ji} that represents the amount of the magnetic flux originally generated in the ith quadrant and going through the jth quadrant domain. In fact this factor is frequency dependent [44–46], and is only constant for a beam with fixed frequency. Chapter 5 will show how these coupling factors can be deduced from the BPM calibration measurement (which is typically performed at a constant beam frequency).

2.5 Incomplete winding angular coverage

The effect introduced to the theoretical response of induced voltage signals by incomplete winding angular coverage is mainly in the value of the geometrical parameters (see appendix A). The polynomials where an explicit dependence on beam transverse coordinates exists are the same for both cases of complete and incomplete angular coverage. An exception is in the fourth order polynomial term which vanishes in case each quadrant covers a range of $\Delta\psi = \frac{\pi}{2}$, while does not in the case of $\Delta\psi < \frac{\pi}{2}$ (a demonstration for the winding ranges and the different angles ψ_1 and $\Delta\psi$ is given in figure 2.3). To summarize the effect on different geometrical parameters, the following equations state the expressions for these parameters in the case of incomplete angular range ($c^\dagger$ terms) written in terms of the parameters in the case of complete angular range (c terms):

$$c_0^\dagger = c_0\,, \tag{2.15}$$

$$c_1^\dagger = \frac{\pi(\cos(\psi_1) - \sin(\psi_1))}{2\Delta\psi} c_1\,, \tag{2.16}$$

$$c_2^\dagger = \frac{\pi(\cos^2(\psi_1) - \sin^2(\psi_1))}{2\Delta\psi} c_2\,, \tag{2.17}$$

$$c_3^\dagger = \frac{\pi(\cos(3\psi_1) + \sin(3\psi_1))}{2\Delta\psi} c_3\,, \tag{2.18}$$

$$c_4^\dagger = \frac{2\pi\sin(4\psi_1)}{2\Delta\psi} c_4\,, \tag{2.19}$$

$$c_5^\dagger = \frac{\pi(\cos(5\psi_1) - \sin(5\psi_1))}{2\Delta\psi} c_5\,. \tag{2.20}$$

The relations governing the response at the output (using the lumped model) does not change either. The same expression as in eq. 2.8 can still be used for the incomplete angular range but with $c^\dagger$ terms replacing c terms and with the fourth order term being included as stated earlier. For quadrant coil 1, this reads:

$$\begin{aligned} U_{\text{out1}}(x,y,\omega) = {} & \omega\gamma_1(\omega_0,\omega_1,\omega)n\mu_0 c_0^\dagger I \Big[1 + c_1^\dagger(x+y) + c_2^\dagger(xy) + c_3^\dagger(-x^3 - y^3 + 3yx^2 + 3xy^2) \\ & + c_4^\dagger(-x^4 - y^4 + 6x^2y^2) + c_5^\dagger(x^5 + y^5 - 10x^3y^2 - 10y^3x^2 + 5y^4x + 5x^4y)\Big]\,. \end{aligned} \tag{2.21}$$

Similarly, for the remaining quadrant coils, eq. 2.6 can be used to construct their expressions.

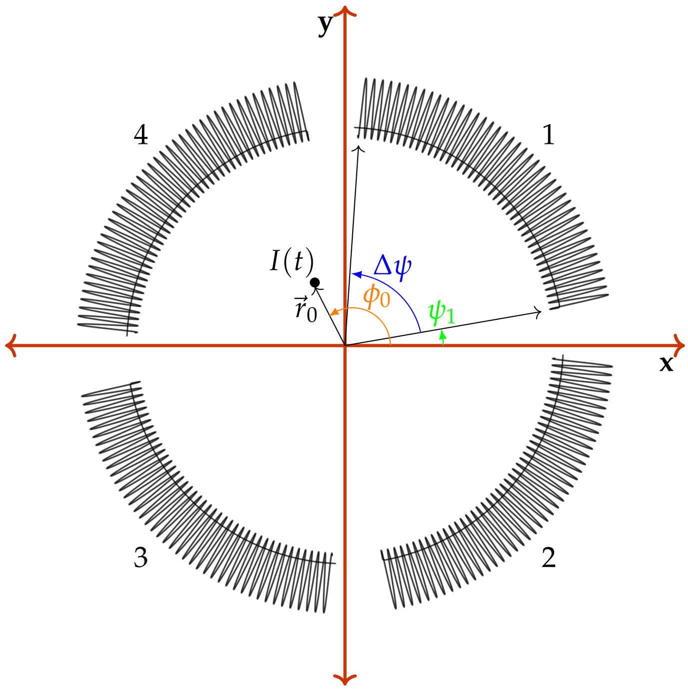

Figure 2.3: Rogowski BPM winding viewed in the xy-plane. Numbers 1 to 4 indicate the quadrant coil number 1 through 4. The vector $\vec{r}_0$ points from the origin towards the beam $I(t)$ center which goes in the longitudinal direction. The angle ψ_1 spans the range between the vector to the initial winding of the quadrant coil and the positive x-axis. The angle $\Delta\psi$ covers the range between the vectors to the start and the end of windings in the quadrant coil. The angle ϕ_0 is made by the beam position vector $\vec{r}_0$ with respect to the positive x-axis.

Chapter 3

Electromagnatic simulations in COMSOL Multiphysics

COMSOL Multiphysics is an interactive environment software for modeling and solving all kinds of physics and engineering problems based on the **F**inite **E**lement **M**ethod (FEM) [47]. This software provides six modules within the Electromagnetic main module or computational electromagnetics branch, which mainly works by solving Maxwell's equations. This chapter introduces the analyses performed within COMSOL using the AC DC* module as one of the six branches under computational electromagnetics. The analyses were performed for the response of a Rogowski BPM coil in different studies and assumptions, like time domain and frequency domain, assuming both 3 dimensional (3D) and 2 dimensional (2D) axisymmetric geometrical cases.

3.1 Transient analysis

3.1.1 Background

The magnetic field interface within the AC DC module was used to investigate the response of a simple Rogowski BPM in the presence of time varying fields. The software runs the analysis based on the following equations [48]:

$$\nabla \times \boldsymbol{H} = \boldsymbol{J}\,, \tag{3.1}$$

$$\nabla \times \boldsymbol{A} = \boldsymbol{B}\,, \tag{3.2}$$

$$\sigma \boldsymbol{E} + \boldsymbol{J_e} = \boldsymbol{J}\,, \tag{3.3}$$

$$\boldsymbol{E} = -\frac{\partial \boldsymbol{A}}{\partial t}\,, \tag{3.4}$$

***A**lternating **C**urrent **D**irect **C**urrent.

where $\boldsymbol{H}$ is the magnetic field intensity, $\boldsymbol{J}$ is the total current density, $\boldsymbol{A}$ is the magnetic vector potential, $\boldsymbol{B}$ is the magnetic flux density, σ is the conductivity, $\boldsymbol{E}$ is the electric field and $\boldsymbol{J_e}$ is the external current density. Using the constitutive relation:

$$\boldsymbol{B} = \mu_0(\boldsymbol{H} + \boldsymbol{M})\,, \tag{3.5}$$

where $\boldsymbol{M}$ denotes the magnetization vector. Ampere's law, which is the main equation solved for within this analysis with the magnetic vector potential as the dependent variable then becomes:

$$\sigma\frac{\partial \boldsymbol{A}}{\partial t} + \boldsymbol{\nabla} \times (\mu_0^{-1}\boldsymbol{\nabla} \times \boldsymbol{A} - \boldsymbol{M}) = \boldsymbol{J_e}\,. \tag{3.6}$$

The used time dependent study assumes the quasi-static approximation, which means that displacements currents are disregarded:

$$\frac{\partial \boldsymbol{D}}{\partial t} = 0\,, \tag{3.7}$$

where $\boldsymbol{D}$ is the electric displacement field. In fact, validity of this approximation is linked to both the operation frequency and the physical size of the modeled object. The rule says that the shortest wavelength (λ) of the signal should be much longer than the effective length of the device (l) [48–52]:

$$l \ll \lambda\,. \tag{3.8}$$

A factor of at least one order of magnitude is usually sufficient to use the quasi-static approximation. For example, if the excitation signal was changing at a rate of 750 kHz[†], a device length smaller than 40 m will not see any spatial wave effects and thus can be modeled using this approximation.

Another important consideration within this study is the skin depth. At high frequency, the current does not flow uniformly throughout the conductor cross sectional area. The depth of a conductor required to get the internal magnetic field intensity attenuated by a factor of 1/e is called the skin depth (δ) and for a good conductor, is given by [52,53]:

$$\delta = \sqrt{\frac{2}{\omega\mu\sigma}}\,, \tag{3.9}$$

where μ is the material magnetic permeability. The coil features used in this study assume a uniform current distribution over the conductor cross sections, but since the modeled winding wire has a radius of 70 µm and for a sinusoidal signal at 750 kHz, this assumption of uniform current density can safely resolve the skin effect as 70 µm is less than $\delta_{750\text{ kHz}} \approx 75.3$ µm.

[†]For a COSY beam with momentum of 0.97 GeV/c, a revolution frequency of 750 kHz is yielded.

3.1.2 Geometry and mesh

Within this analysis, a simple 3D geometry (without metallic flanges) for the Rogowski BPM was considered. This included the four quadrant coil domains, the core, a wire with a diameter of 0.5 mm along the central axis to mimic the beam source and a cylinder for the surrounding air. Figure 3.1 shows these different domains. Each quadrant coil was chosen with a turn number of 445 and a wire diameter of 140 µm. The core was modeled with radii of 58.625 mm and 6.375 mm. The material selected for the core was the PEEK. A copper conductor was selected as a material for both the quadrant coils and the exciting wire mimicking a beam source. The surrounding cylinder was modeled using air as material.

A fine mesh was selected for the four quadrants' domains‡, the central wire and the

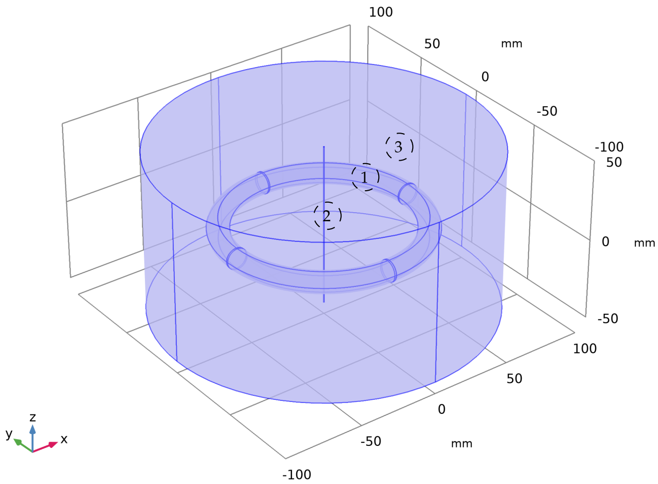

Figure 3.1: Geometry of a simple Rogowski BPM model used in the transient analysis. The label 1 represents a single quadrant coil domain with turn number of 445 and wire diameter of 140 µm. The label 2 represents the central wire domain with a diameter of 0.5 mm. The label 3 represents the cylindrical air domain surrounding the geometry. The PEEK core is the torus domain around which the four quadrants are modeled (non labeled interior geometry) is chosen with radii of 58.625 mm and 6.375 mm.

PEEK core. For the air domain, a normal mesh was chosen§. The entire geometry had about 2 million tetrahedral mesh elements in total. In figure 3.2, panel (a) shows the mesh quality for the whole geometry. Panel (b) is a zoomed inset for the mesh quality around a part of the domain of the central wire and one quadrant coil¶.

‡Maximum and minimum predefined element sizes were 7mm and 0.1mm, respectively.

§Maximum and minimum predefined element sizes were 20mm and 3.6mm, respectively.

¶The mesh element quality where 1 represents a perfectly regular element, and 0 represents a degenerated element based on skewness quality measure and considering all elements types in the mesh.

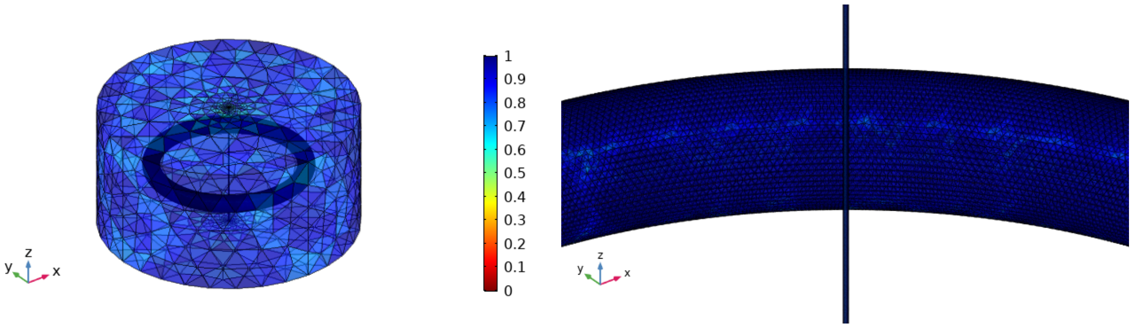

(a) **(b)**

Figure 3.2: Mesh quality and structure of the entire 3D geometry (a) and in a part of the domain of the central wire and one quadrant coil (b). The color legend indicates the elements quality from low (0) to high (1).

3.1.3 Physics and solver

The four quadrant coils were modeled using the built in 'homogenized multi-turn coil' feature within the magnetic field physics interface. In addition, to avoid singularities and to ensure having a unique solution, a 'Gauge fixing for A field' boundary condition was added to all domains. Together with the magnetic field interface, the electric circuit interface was used to provide a harmonic excitation to the central wire , a current with an amplitude of 0.5 mA and a frequency of 750 kHz was used. In order to account for the capacitive effects from a 16 cm long coaxial cable, which is usually used in signal transmitting and the effect from the twisted wire extensions, a parallel capacitor of 21 pF was connected to each quadrant coil along with different circuit elements used to enable a voltage measurement between each quadrant coil's terminals[||].
The test was performed on a two-socket workstation, with 16 cores per processor, operated with Windows®10, COMSOL Multiphysics® 5.5 and a RAM total capacity of 120 GB. In the transient study, a PARDISO direct solver was chosen and a time span of 100 µs with steps of 20 ns was used, this resulted in a total study computational time of 12 hours and 40 minutes.

3.1.4 Results

Figure 3.3 panel (a) shows a Multi-slice plot of three perpendicular planes intersecting at the central axis for the normalized magnetic flux density[**] in the whole geometry. A

[||] Each quadrant coil was connected to a resistance of 1 MΩ and an external I vs. U circuit feature that enables a voltage measurement.

[**] The magnetic flux density norm is defined as: $\sqrt{\mathrm{realdot}(B_r, B_r) + \mathrm{realdot}(B_{phi}, B_{phi}) + \mathrm{realdot}(B_z, B_z)}$, where B_r, B_{phi} and B_z are the components of the magnetic flux in cylindrical coordinates. A similar definition is followed for the electric field norm. The realdot(a, b) expression treats complex numbers a and b as if they

surface plot for the normalized magnetic flux density in the domain of the four quadrant coils is shown in panel (b). Both figure panels are calculated at the time $t = 98.64$ μs. On the surface of the four quadrant coils, the normalized flux varies from around 46 pT (low) to around 62 pT (high).
The four measured induced voltages from the quadrant coils of the Rogowski BPM versus time over a span of 100 μs are shown in figure 3.4 (a). The figure clearly shows the distortions caused by the time delay introduced by the lumped element (mainly parallel capacitors). A magnified plot for the same response in panel (a) over the time interval $80 - 100$ μs when the system starts settling is shown on the right. To check if the distortions are really coming from a time delay and not due to any potential errors in the study, the same transient analysis was repeated with excluded parallel capacitors (see Appendix B).

were real-valued vectors of length 2 and returns their dot product.

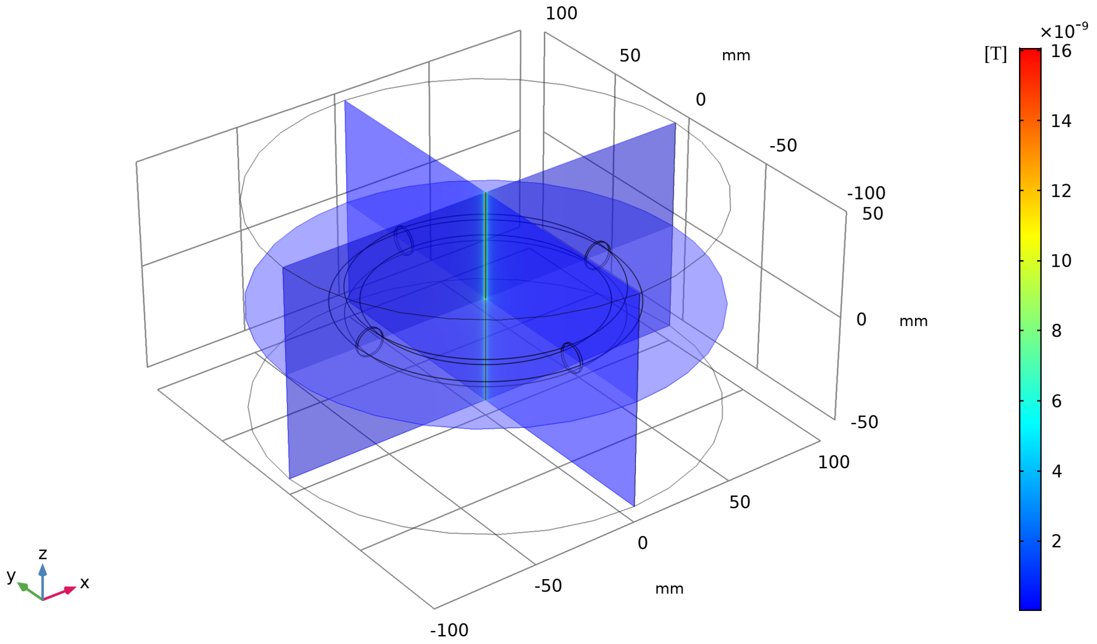

(a)

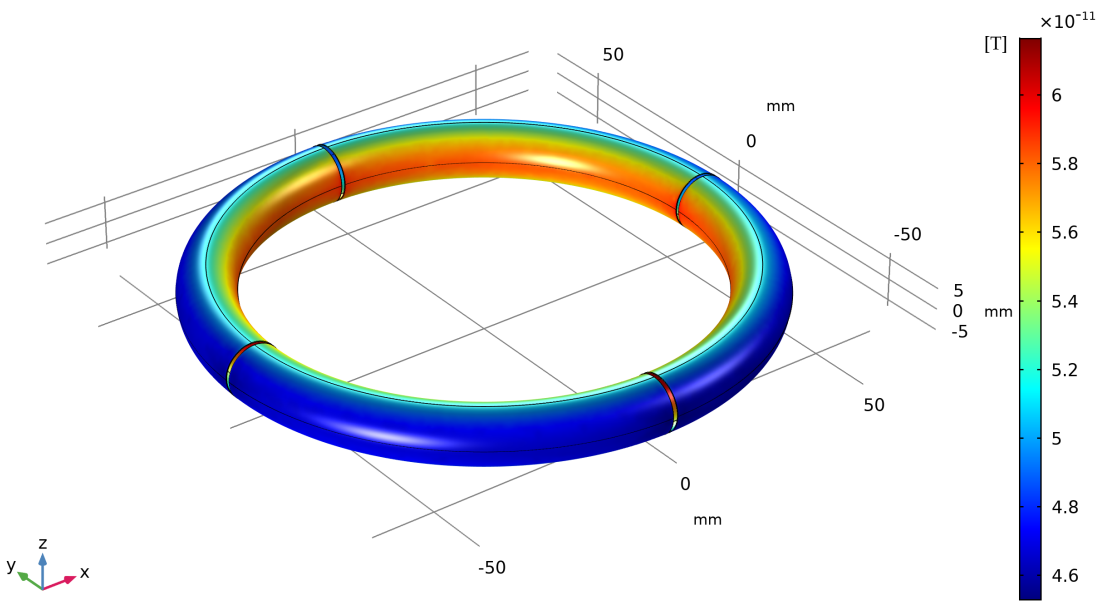

(b)

Figure 3.3: Multi-slice plot of the normalized magnetic flux density in the whole geometry (a) and a surface plot of the normalized magnetic flux density in the domains of the four quadrant coils (b). Both figure panels are calculated at the time $t = 98.64$ µs.

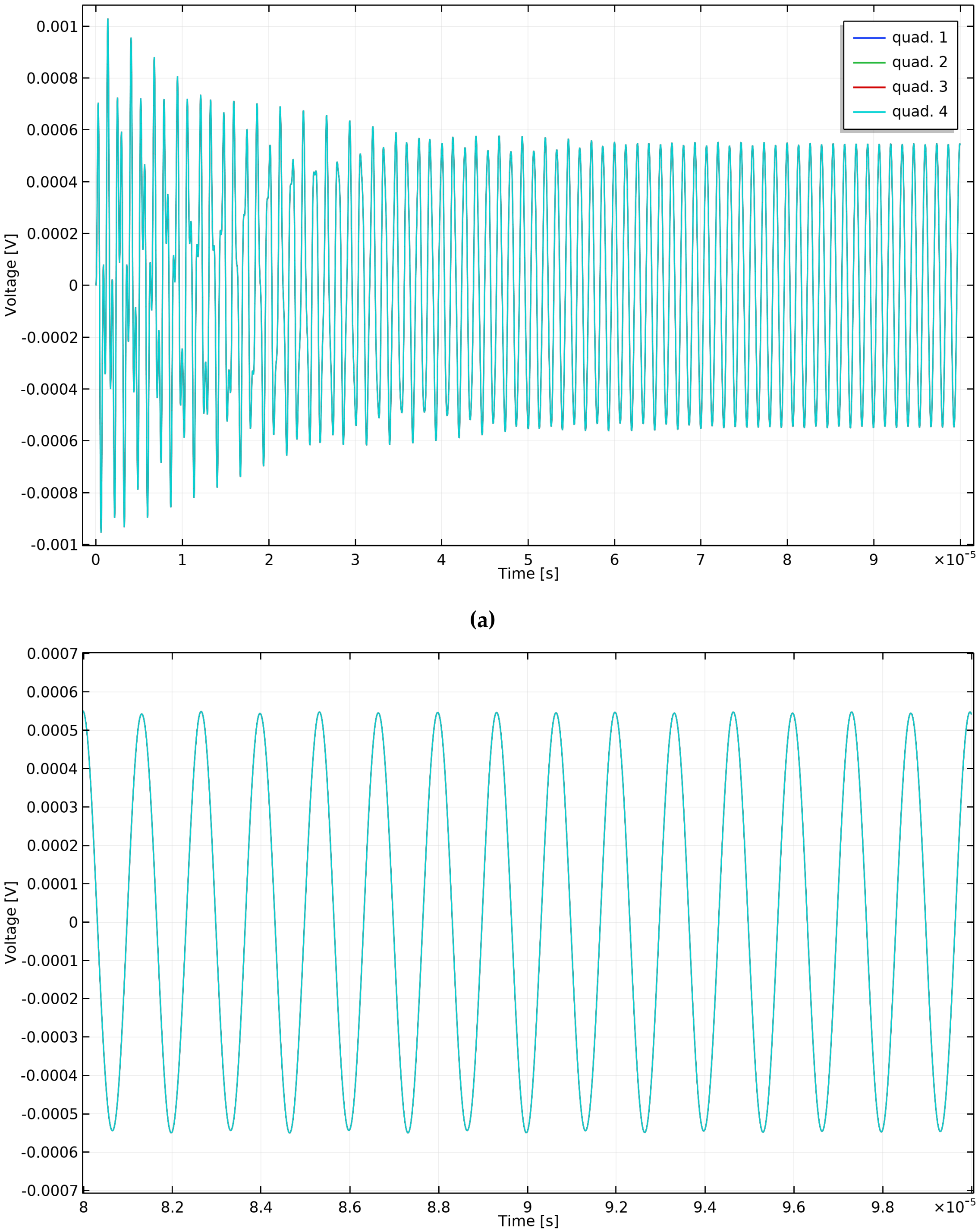

(a)

(b)

Figure 3.4: The four measured induced voltages from the Rogowski BPM versus the time over a span of 100 μs (a). A magnified plot for the response in panel (a) in the time interval 80 – 100 μs (b).

3.2 Frequency domain analysis (study 1)

When both the excitation and the system response vary sinusoidally, solving the problem in the frequency domain can be used rather than in the time domain. Furthermore, time-domain simulations are more computationally challenging than frequency-domain ones because their solution time is directly proportional to how long the time span of interest is, in addition to its dependence on the system nonlinearities. This section introduces different studies that were carried out in the frequency domain for the Rogowski BPM with the same 3D geometry and mesh features as stated in the previous section for the case of the transient analysis. Additionally, the same physics interfaces (magnetic field and electric circuit) were used with the same boundary conditions and the same solver. This resulted in a total study computational time of 25 minutes.

3.2.1 Background

The frequency domain analyses within the magnetic field interface in the AC DC module are based on the following equations [48]:

$$\nabla \times \boldsymbol{H} = \boldsymbol{J}\,, \tag{3.10}$$

$$\nabla \times \boldsymbol{A} = \boldsymbol{B}\,, \tag{3.11}$$

$$\sigma \boldsymbol{E} + \boldsymbol{J}_e + i\omega \boldsymbol{D} = \boldsymbol{J}\,, \tag{3.12}$$

$$\boldsymbol{E} = -i\omega \boldsymbol{A}\,, \tag{3.13}$$

Unlike the transient case, the displacement currents are not neglected here ($\frac{\partial \boldsymbol{D}}{\partial t} \neq 0$). Using the constitutive relations:

$$\boldsymbol{B} = \mu_0(\boldsymbol{H} + \boldsymbol{M})\,, \tag{3.14}$$

$$\boldsymbol{D} = \epsilon_0 \boldsymbol{E}\,, \tag{3.15}$$

Ampere's law, with the magnetic vector potential as the dependent variable then becomes:

$$(i\omega\sigma - \omega^2\epsilon_0)\boldsymbol{A} + \nabla \times (\mu_0^{-1}\nabla \times \boldsymbol{A} - \boldsymbol{M}) = \boldsymbol{J}_e\,. \tag{3.16}$$

3.2.2 Results

Panel (a) in figure 3.5 shows a surface plot for the normalized magnetic flux density in the domains of the four quadrant coils. Red arrows on the surface represent the components of the flux density in the x, y and z directions. Panel (b) represents a surface plot of the normalized electric fields in the domains of the four quadrant coils. Red arrows on the surface represent the components of the electric field in the x, y and z directions. As stated earlier, this analysis carried out in the frequency domain takes into account the time rate of change of displacement electric field. Figure 3.6 shows a surface plot of the normalized electric displacement field in the domains of the four quadrant coils with red arrows on the surface represent the components of the displacement current density in the x, y and z directions. The measured induced voltages (assuming same circuitry used in transient study) were 546.766, 546.792, 546.795 and 546.77 μV for the quadrant coils 1 through 4, respectively.

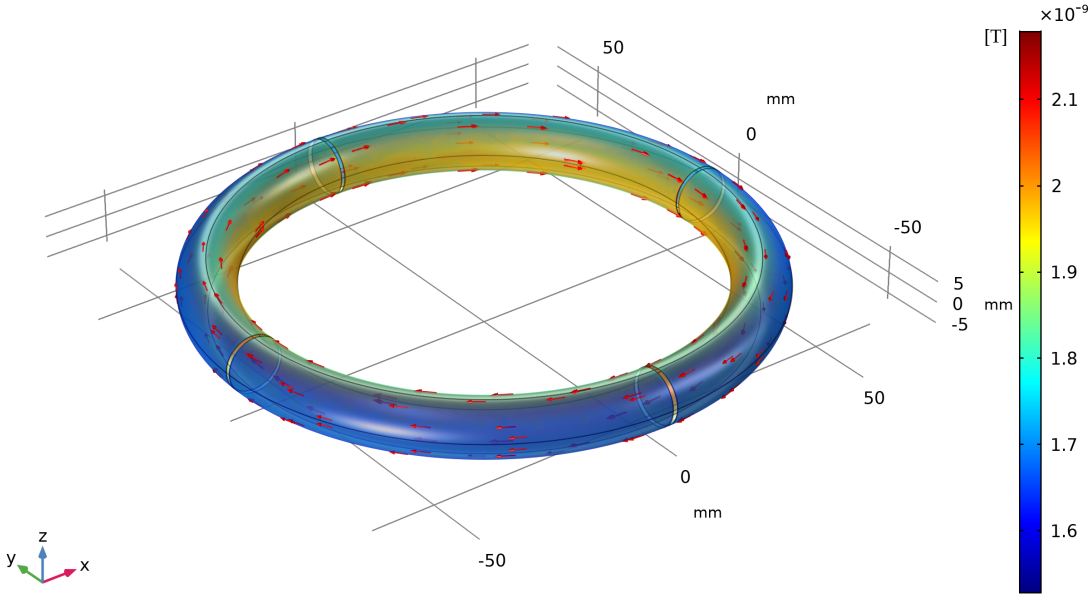

(a)

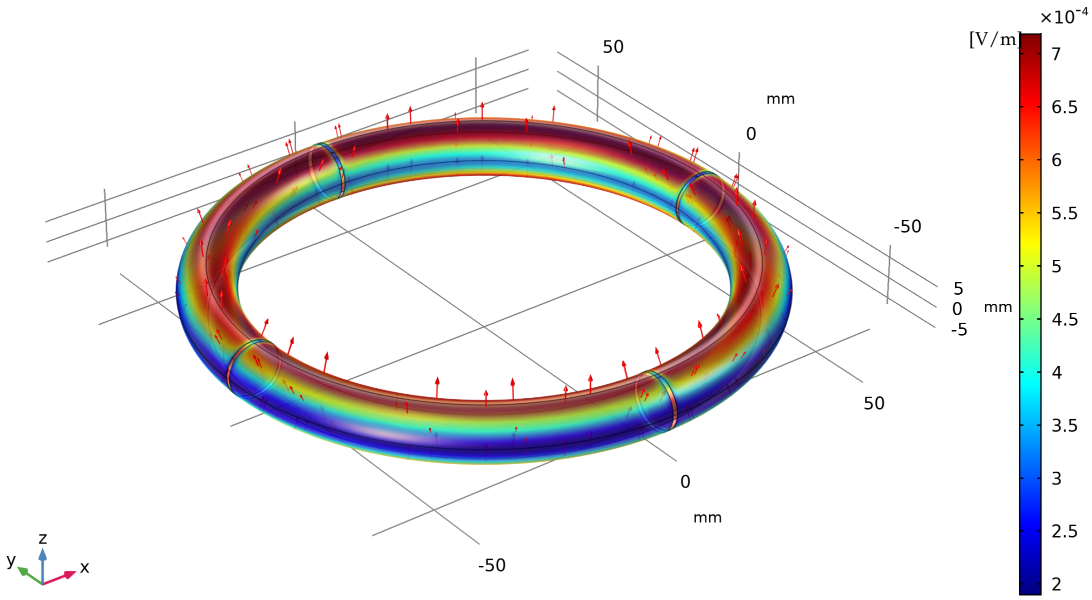

(b)

Figure 3.5: Surface plot of the normalized magnetic flux density in the domains of the four quadrant coils. Red arrows on the surface represent the components of the flux density in the x, y and z directions (a). Surface plot of the normalized electric fields in the domains of the four quadrant coils. Red arrows on the surface represent the components of the electric field in the x, y and z directions (b).

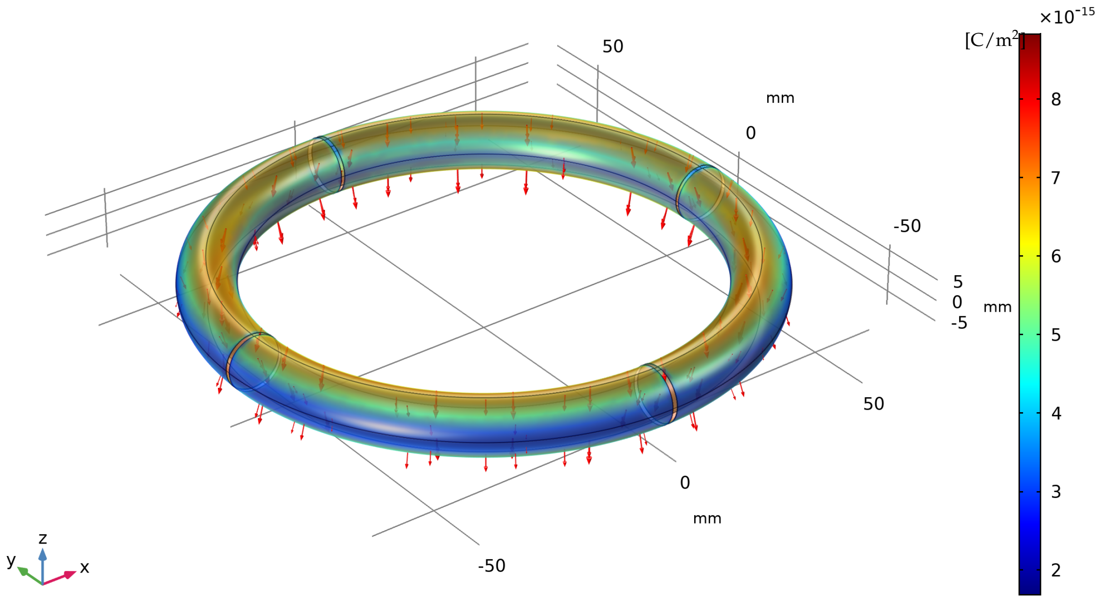

Figure 3.6: Surface plot of the normalized electric displacement field in the domains of the four quadrant coils. Red arrows on the surface represent the components of the displacement current density in the x, y and z directions.

3.3 Frequency domain analysis (study 2)

Another study in the frequency domain with the same mesh and geometry as in the previous studies was performed but with different boundary conditions. The magnetic field physics interface was still used but the electric circuit interface was used only to excite the central wire whenever needed. The goal was to check how applying different boundary conditions can affect each quadrant coil's response and whether it is fulfilling physics expectations. A summary of these different case studies and their boundary conditions is given in table 3.1. In all case studies, the frequency of 750 kHz was chosen for excitation signals. The boundary conditions of $V = 0$ and $I = 0$ represent a quadrant coil in the closed ended and open ended cases, respectively. In the cases 6 and 7, only quadrant coil 1 existed, the remaining three quadrants were modeled as air domains and not copper or as coil features. The reason was to eliminate the influence introduced by the presence of the nearby coils in a separate case study and compare it with other cases. The results from these different case studies are summarized in table 3.2. For the closed circuit (case 1), the induced currents from all quadrants were around 277 pA with variations in the 10 fA level. For case 2, when the Rogowski quadrants were open ended, the induced voltages were 457 µV with variations between the coils on the level of 10 nV. However, the level of induced voltage in the quadrant coil 1 from the case study 2 compared with that from the cases 3, 4 and 5 follows the physical expectations. When one coil is set with a different boundary condition that lets the current flow through it, this will generate some induced fields that are opposing the one generated by the central wire, or in other words, the level of induced voltage should get reduced.
The selection for the current amplitude of 292.7 nA, used to excite the Rogowski quadrant domains in the last three cases was based on the results obtained from the case 7 when only quadrant 1 existed as a closed ended coil. The inductance for quadrant 1 calculated from case 10 was 349.97 µH . The difference in the inductance from the other quadrants was in the level of 10 nH (see table 3.2).
The case study 8 was used to investigate the mutual inductance (L_{ij}) and coupling coefficients between the four quadrant coils. The mutual inductance in a time harmonic case can be computed through[††]:

$$L_{ij} = \frac{V_j}{i\omega I_i}\,. \tag{3.17}$$

while the coupling coefficient is given by:

$$k_{ij} = \frac{L_{ij}}{\sqrt{L_i L_j}}\,. \tag{3.18}$$

In fact, the coupling coefficient can also be computed by finding the ratio of the flux or voltage in the ith and jth domains such as:

$$k_{ij} = \frac{\Phi_j}{\Phi_i} = \frac{V_j}{V_i}\,. \tag{3.19}$$

[††]Here i represents the imaginary unit. The subscripts i and j are indices to distinguish different quadrant coils.

Table 3.3 shows the results for mutual inductance and coupling coefficients computed via the case study 8. Clearly, the opposite quadrant coil 3 has the least mutual inductance and coupling with respect to quadrant coil 1 as a reference (which was excited in the study) as this domain is the farthest in distance. The values for the neighboring quadrants 2 and 4 are similar and follow the expectations as all the Rogowski four domains were modeled to be identical and to hold a symmetry in the geometrical spacing. In addition, the self inductance of quadrant coil 1 was 331.36 µH, which is less than what was computed through the case study 10 by about 19 µH, this can be explained by the difference in the net generated flux through domain 1 in both cases as a result of setting different boundary conditions (less overall flux when the other three quadrants are closed ended). However, it is very important to mention that these calculations for mutual inductances, induced voltages and coupling coefficients as listed in tables 3.2 and 3.3 are subject to the setting of boundary conditions, the results may vary depending on the state of the system (for example, if some or all coils were active, loaded or not).
Panel (a) in figure 3.7 shows a surface plot of the normalized magnetic flux density in the four Rogowski domains when the quadrant coil 1 is excited with a current of 292.7 nA while the remaining quadrants are open ended from the case study 8. The same surface plot as in panel (a) is plotted for the opposite quadrant 3 is shown in panel (b).The red arrows in figure represent the directional magnetic flux density along the x-,y- and z-axis. Similar illustration for the normalized magnetic flux density in the surface domain of the two neighboring quadrants 2 and 4 is shown in figure 3.8 from the same case study 8 (see the appendix B for similar representation of the normalized magnetic flux density when the coils were closed ended from the case study 9).

Table 3.1: The case studies and their boundary conditions from the second frequency domain analysis.

Case study	Boundary condition[b]
1	$I = 0.5$ mA (central wire), $V = 0$ (all Rogowski quadrants)
2	$I = 0.5$ mA (central wire), $I = 0$ (all Rogowski quadrants)
3	$I = 0.5$ mA (central wire), $I = 0$ (quadrant 1) and $V = 0$ (quadrants 2, 3 and 4)
4	$I = 0.5$ mA (central wire), $I = 0$ (quadrants 1 and 3) and $V = 0$ (quadrants 2 and 4)
5	$I = 0.5$ mA (central wire), $I = 0$ (quadrants 1 and 4) and $V = 0$ (quadrants 2 and 3)
6	$I = 0.5$ mA (central wire),[a] $I = 0$ (quadrant 1)
7	$I = 0.5$ mA (central wire),[a] $V = 0$ (quadrant 1)
8	$I = 292.7$ nA (quadrant 1), $I = 0$ (quadrants 2, 3 and 4)
9	$I = 292.7$ nA (quadrant 1), $V = 0$ (quadrants 2, 3 and 4)
10	$I = 292.7$ nA (all Rogowski quadrants)

[a] Only quadrant coil 1 existed, the remaining quadrants were modeled as air domains.
[b] $I = 0$ represents an open ended condition, $V = 0$ represents a closed ended condition.

Table 3.2: The results from the different case studies from the second frequency domain analysis.

Case study	Result[a]
1	$I_1 = 277.11$, $I_2 = 277.15$, $I_3 = 277.15$ and $I_4 = 277.14$
2	$V_1 = 457.41$, $V_2 = 457.43$, $V_3 = 457.44$ and $V_4 = 457.41$
3	$V_1 = 432.44$, $I_2 = 284.52$, $I_3 = 277.54$ and $I_4 = 284.51$
4	$V_1 = 433.05$, $I_2 = 291.91$, $V_3 = 433.07$ and $I_4 = 291.9$
5	$V_1 = 444.25$, $I_2 = 285.12$, $I_3 = 285.12$ and $V_4 = 444.26$
6	$V_1 = 457.41$
7	$I_1 = 292.7$
8	$V_1 = 457.41$, $V_2 = 12.213$, $V_3 = 1.2941$ and $V_4 = 12.217$
9	$V_1 = 456.37$, $I_2 = 7.5232$, $I_3 = 0.15957$ and $I_4 = 7.5254$
10	$L_1 = 349.97$, $L_2 = 349.94$, $L_3 = 349.94$ and $L_4 = 349.94$

[a] Units for V_i, I_i and L_i are in µV, nA and µH, respectively.

Table 3.3: Mutual inductance and coupling with respect to quadrant coil 1 from the second frequency domain analysis.

i,j quadrants	L_{ij} [µH]	k_{ij}
1, 1	331.36	100%
1, 2	8.8475	2.6703%
1, 3	0.93748	0.28294%
1, 4	8.85	2.6710%

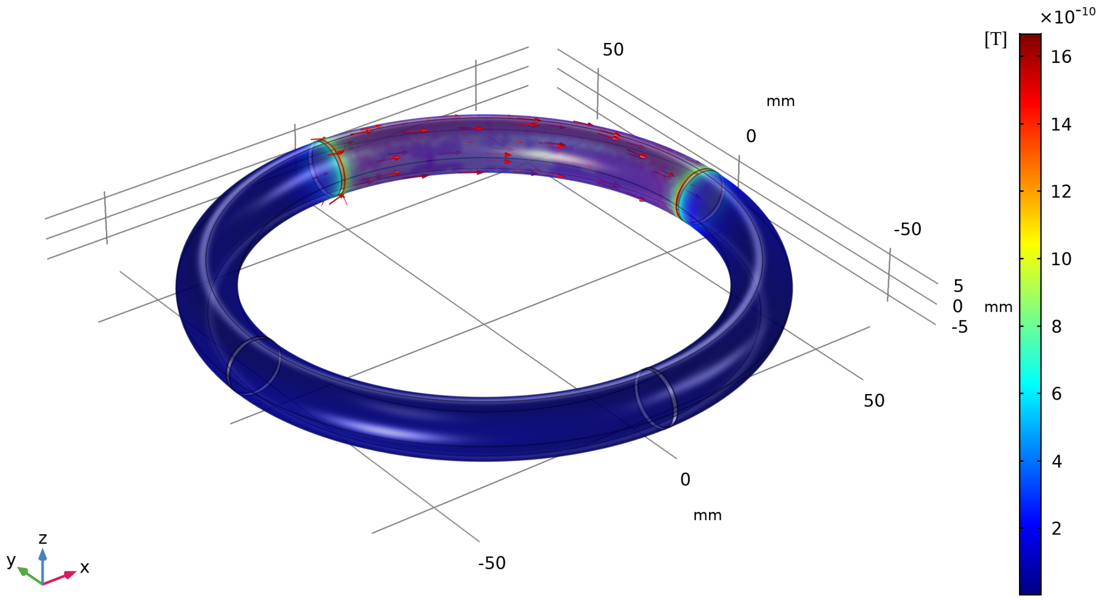

(a)

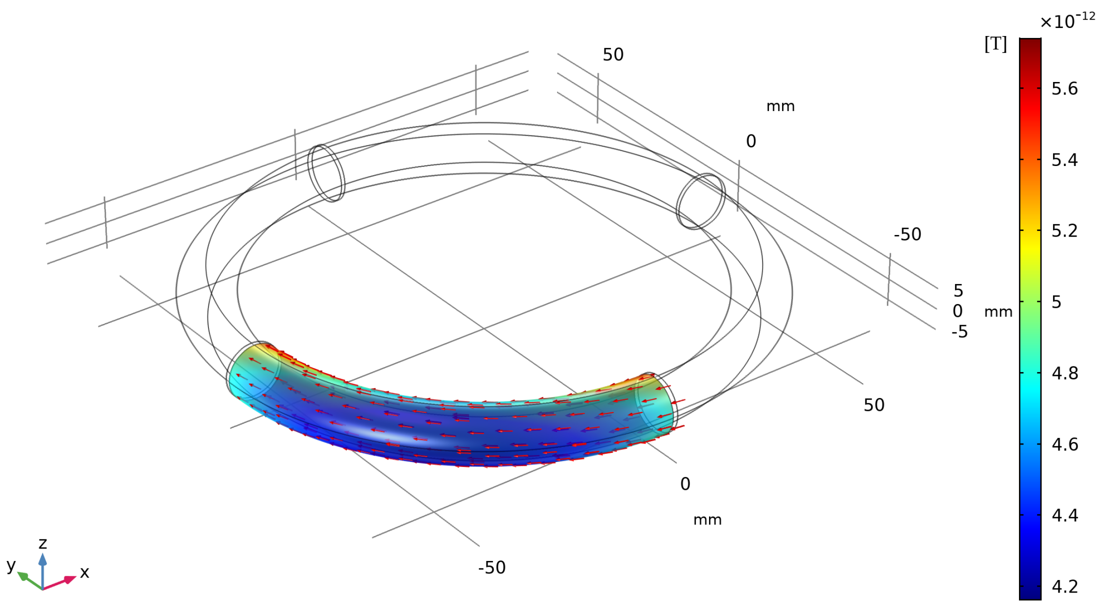

(b)

Figure 3.7: Normalized magnetic flux density in the Rogowski's four domains when the quadrant 1 is excited with a current of 292.7 nA and the remaining quadrants are open ended from the case study 8 (a). The same surface plot as in (a) for the domain of the opposite quadrant 3 (b). The red arrows represent the directional magnetic flux density along the x-,y- and z-axis.

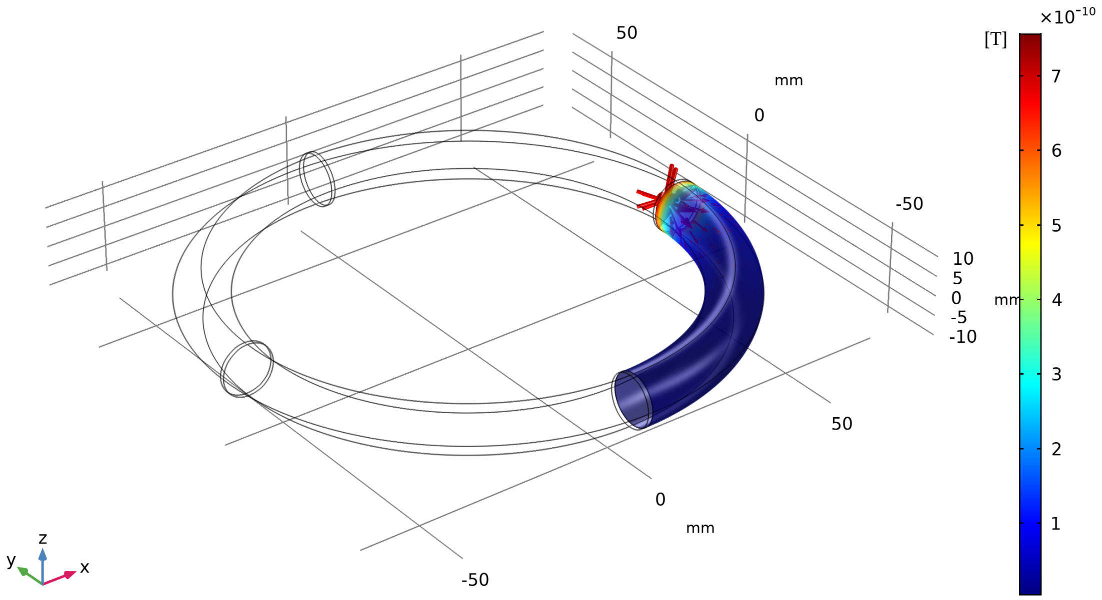

(a)

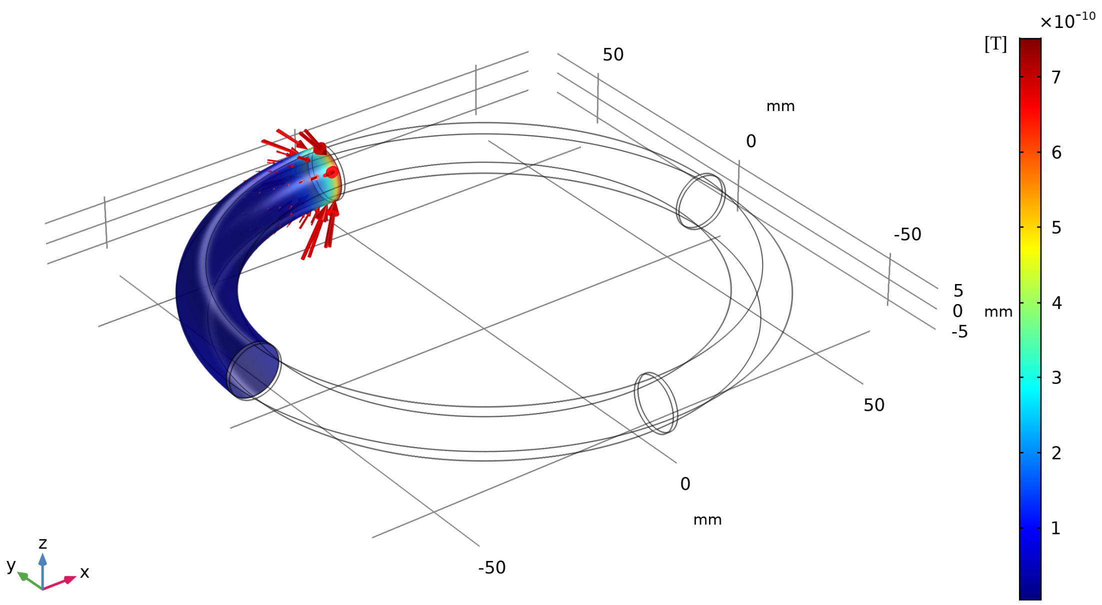

(b)

Figure 3.8: Normalized magnetic flux density in the surface domains of the neighboring quadrant 2 (a) and the neighboring quadrant 4 (b) when the quadrant 1 is excited with a current of 292.7 nA and the remaining quadrants are open ended from the case study 8. The red arrows represent the directional magnetic flux density along the x-,y- and z-axis.

3.4 Rotation versus sensitivity

The sensitivity of the Rogowski BPM can be defined as the strength of the relation between some mathematical expression of the electrical responses from the four quadrants and the beam (which is here mimicked by an excited central wire) transverse positions. In order to investigate how different rotation scenarios for the Rogowski BPM can affect the sensitivity, a dedicated analysis was made in the frequency domain with the same geometry, mesh, solver, boundary conditions and physics as those in section 3.1. The additional work in this analysis was adding a parametric sweep study step which loops over all the defined positions each time before moving into the main frequency domain study step.

Figure 3.9 shows the two possible orientations viewed in the xy-plane, which are used for investigating the sensitivity within the current analysis. In panel (a), the first possible orientation of the windings of the Rogowski BPM is shown, where the quadrant coil 1 spans the angular range from 0° to 90°. In panel (b), the second possible orientation of the windings of the Rogowski BPM with the quadrant coil 1 spanning the angular range from 45° to 135° is shown. In both panels, the sequence of quadrants is in the clockwise direction. In the parametric sweep, the value of the vertical axis was fixed at 10 mm while the horizontal axis varied from -10 mm to 10 mm with steps of 1 mm. The reason behind fixing a positional parameter and varying the other was to ease the mission in construction the sensitivity as a function of one argument and hence to make the comparison easier. The mathematical formula that was used to link responses with the transverse coordinates was the difference over the sum (or as commonly known, the delta over sigma):

$$\frac{\Delta_x}{\Sigma} = \frac{\text{right} - \text{left}}{\text{sum}}, \tag{3.20}$$

$$\frac{\Delta_y}{\Sigma} = \frac{\text{up} - \text{down}}{\text{sum}}. \tag{3.21}$$

Where for orientation 1:

$$\text{right} = U_1 + U_2, \tag{3.22}$$
$$\text{left} = U_3 + U_4, \tag{3.23}$$
$$\text{up} = U_1 + U_4, \tag{3.24}$$
$$\text{down} = U_2 + U_3, \tag{3.25}$$

with U_i for the measured electrical response from the ith quadrant coil. While for orientation 2:

$$\text{right} = U_2, \tag{3.26}$$
$$\text{left} = U_4, \tag{3.27}$$
$$\text{up} = U_1, \tag{3.28}$$
$$\text{down} = U_3. \tag{3.29}$$

The sum is uniquely defined for both cases as:

$$\text{sum} = \quad U_1 + U_2 + U_3 + U_4 \,. \tag{3.30}$$

Figure 3.10 shows the $\frac{\Delta_x}{\Sigma}$ plotted against the central wire's x positions for the two windings' orientations shown in figure 3.9. The horizontal positions were modified within the range of ± 10 mm while the vertical position was fixed at 10 mm for all data points. From the plot, the sensitivity is better in the case of the first orientation, by simply neglecting the higher orders, the slope for a linear relation (between $\frac{\Delta_x}{\Sigma}$ and x positions) from the second orientation is about 0.7 that from the first orientation which makes a good agreement with the theoretical expectations (for more details see appendix B.3).
To check whether this conclusion is valid if the windings did not complete the full $\pi/2$ range, another similar study was performed but with the total turn number reduced by a factor of a third (296 instead of 445) which resulted in a span of around 60°. Figure 3.11 shows the two possible orientations for this case. The quadrant coil 1 spans the angular range from 15° to 75° for orientation 1. For the second orientation, the quadrant coil 1 spans the angular range from 60° to 120°.
As shown in figure 3.12, the sensitivity is again better in the case of the windings orientation 1 even if the windings did not fully complete the angular range (while keeping the desired symmetry in the geometry).

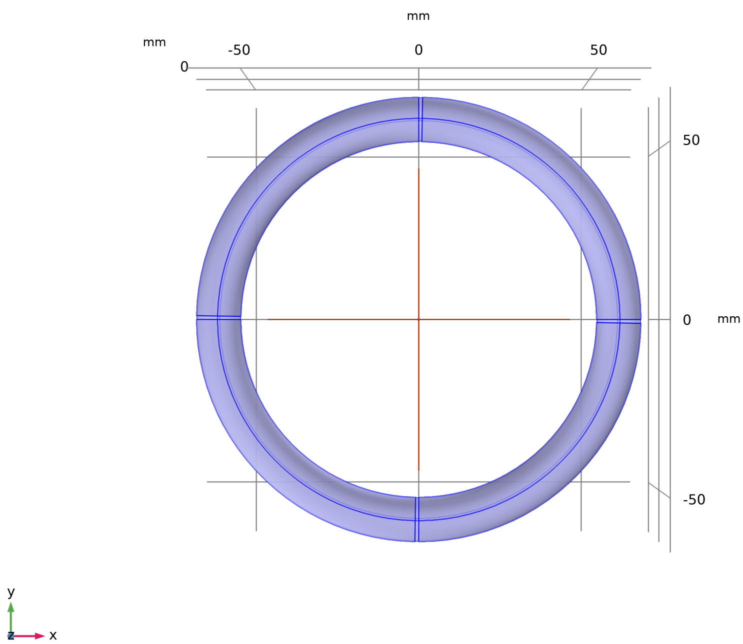

(a)

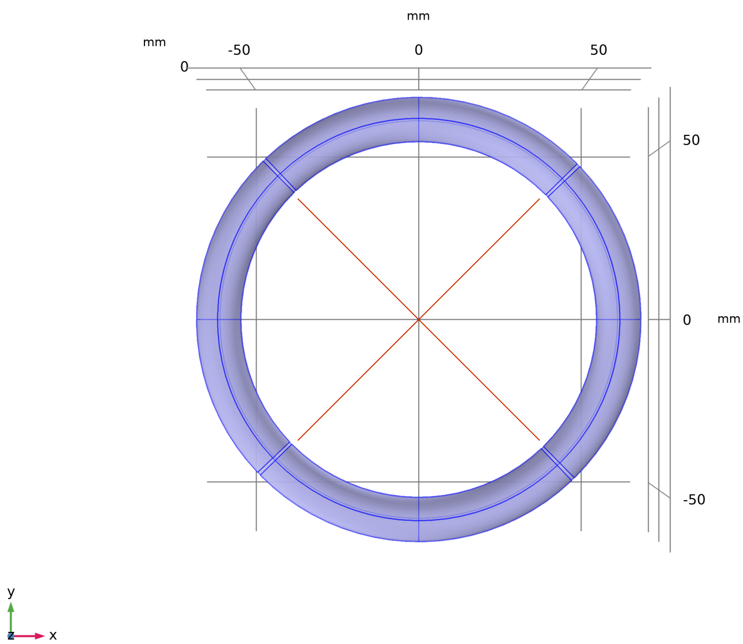

(b)

Figure 3.9: The first possible orientation for the windings of the Rogowski BPM. The quadrant coil 1 spans the angular range from 0° to 90° (a). The second possible orientation for the windings of the Rogowski BPM. The quadrant coil 1 spans the angular range from 45° to 135° (b). In both panels, the sequence of quadrants is in the clockwise direction. The red crosses are drawn to guide the eye to the start and to the end of the windings in the different quadrants.

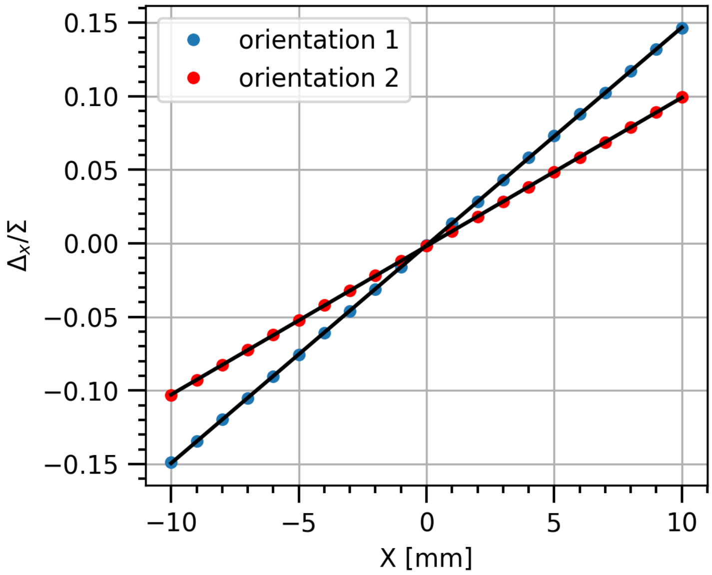

Figure 3.10: $\frac{\Delta_x}{\Sigma}$ plotted against the central wire's x positions for the two windings orientations shown in figure 3.9. From the plot, the sensitivity to positions is better in the case of the first orientation. The vertical position was fixed at 10 mm for all data points.

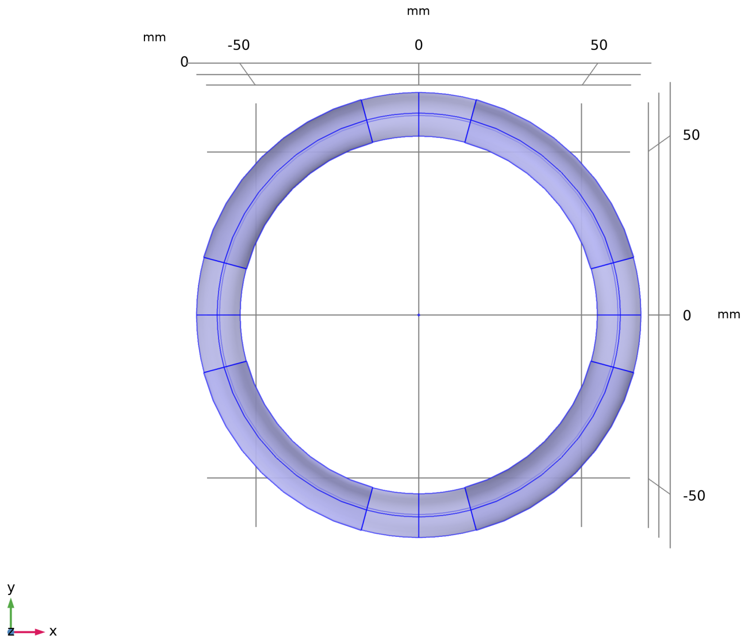

(a)

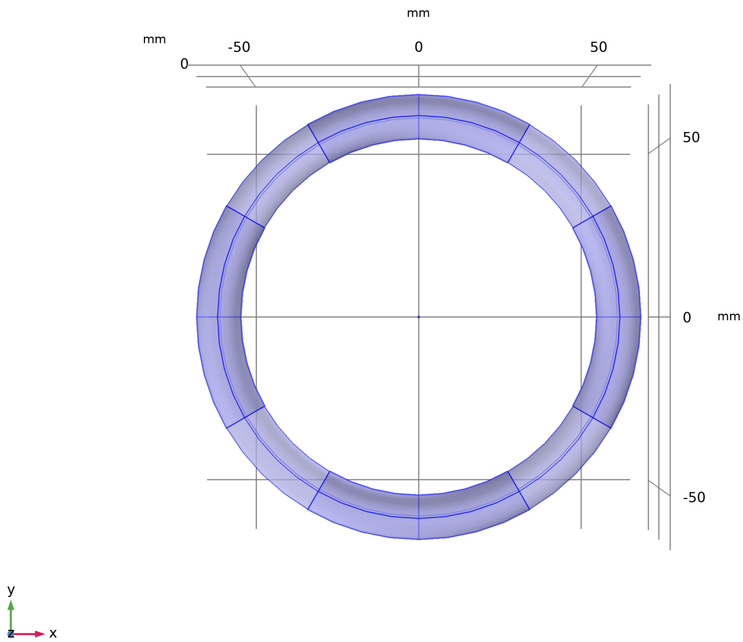

(b)

Figure 3.11: The first possible orientation of the windings of the Rogowski BPM with incomplete angular coverage. The quadrant coil 1 spans the angular range from 15° to 75° (a). The second possible orientation of the windings of the Rogowski BPM with incomplete angular coverage. The quadrant coil 1 spans the angular range from 60° to 120° (b). In both panels, the sequence of quadrants is in the clockwise direction.

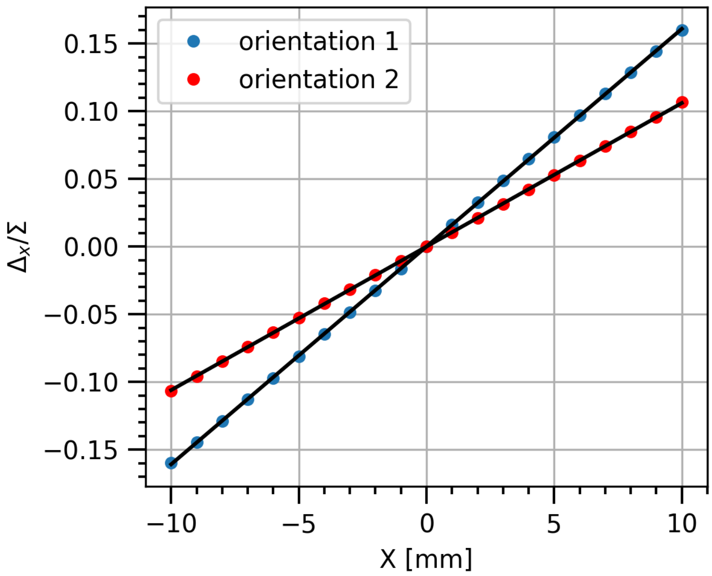

Figure 3.12: $\frac{\Delta_x}{\Sigma}$ plotted against the central wire's x positions for the two windings orientations shown in figure 3.11. From the plot, the sensitivity to positions is better in the case of the first orientation. The vertical position was fixed at 10 mm for all data points.

3.5 Electrical response versus positions

To investigate how both the voltage response in general and the sensitivity of the Rogwski BPM device changes as a function of the beam transverse positions, the study in the previous section was extended to include variations in vertical positions as well. The coil with 445 turns was used in this analysis with widings' configuration as orientation 1 (see figure 3.9 panel (a)). The position of the central wire that mimics a beam was varied in a square grid ($\pm$10 mm with steps of 2 mm). This analysis was performed in the frequency domain and had a total computation time of 61 hours.
Figures 3.13 and 3.14 show the $\frac{\Delta_y}{\Sigma}$ plotted against the $\frac{\Delta_x}{\Sigma}$ for all the scanned grid positions in the xy-plane. The simulation results were compared with two theoretical models, one that is based on eqs 2.9 and 2.6 and another that is based on eqs 2.11-2.14 where the coupling between the quadrant coils is included (see chapter 2). In panel (a) for the two figures, the blue points represent the simulation while the red points represent the fit models. The residuals are plotted in panel (b). Clearly the shape of residuals is more reasonable for the model 2 (where the coupling is included) if compared to the model 1 results. In addition, the residuals are one order of magnitude smaller for the second model.

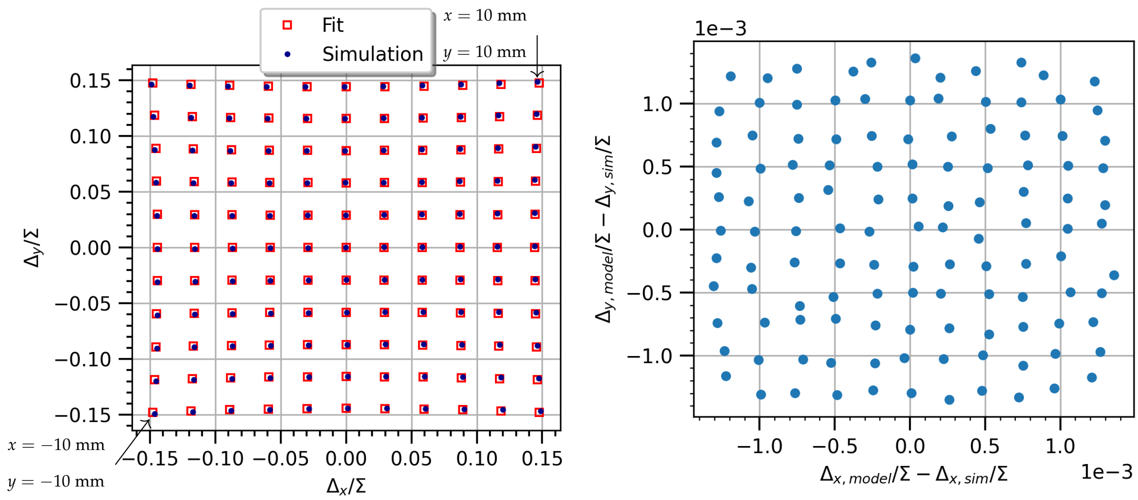

(a) **(b)**

Figure 3.13: Panel (a): the $\frac{\Delta_y}{\Sigma}$ against the $\frac{\Delta_x}{\Sigma}$. The blue dots represent the simulation while the red squares represent the fit model 1. The arrows indicate the locations of the first ($x = -10$ mm and $y = -10$ mm) and the last ($x = 10$ mm and $y = 10$ mm) position grids in the scanned map. Panel (b): the residuals plot for the difference between the fit model 1 and the simulation.

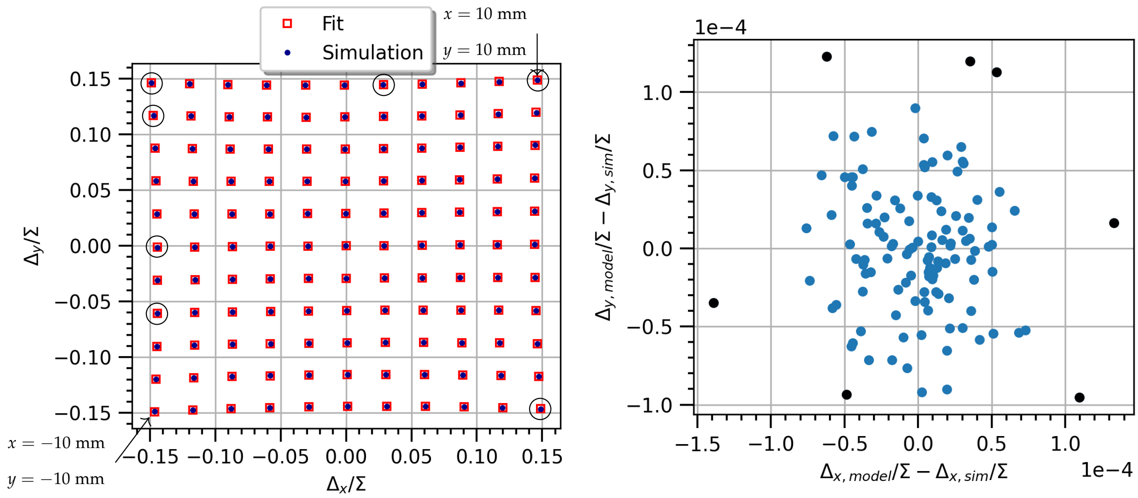

(a) **(b)**

Figure 3.14: Panel (a): the $\frac{\Delta_y}{\Sigma}$ against the $\frac{\Delta_x}{\Sigma}$. The blue dots and the red squares represent the simulation and the fit model 2 which takes into account the coupling between separate quadrants, respectively. The arrows indicate the locations of the first ($x = -10$ mm and $y = -10$ mm) and the last ($x = 10$ mm and $y = 10$ mm) position grids in the scanned map. Panel (b): the residuals plot for the difference between the fit model 2 and the simulation. Clearly the shape of residuals is more reasonable if compared with the model 1 results. In addition, the residuals are one order of magnitude smaller for this model. The black points correspond to the maximum-valued residuals (also indicated with black circles on the left panel).

3.6 2D axisymmetric analysis

In the former studies, the 3D geometry was used to run the different analysis. Within the current analysis, a 2D axisymmetric approximation was used to investigate the single quadrant coil's electrical properties. As the name of the approximation implies, an axial symmetry should be present in order to use such a geometry, for this, the cylindrical configuration was used to describe the geometry of a single coil‡‡. In addition to geometry, different meshing and physics were used here compared to the previous analysis.

3.6.1 Geometry and mesh

As mentioned earlier, a cylindrical axial symmetry was used as an approximation for a single quadrant's geometry. Figure 3.15 shows the full 2D axisymmetric geometry used

‡‡In reality, the single quadrant is curved, but for approximation, an axial symmetry can still be used.

in the analysis (to the left). The horizontal axis is represented by the radial R distance and the vertical axis is represented by the longitudinal Z distance. A magnified picture for the same geometry around the center is shown on the right. The two arrows are pointing to the insulation and the windings' domains. The right rectangular side represents the air domain, the left rectangular side represents the core domain. PEEK material was chosen for the core, copper for the windings and kapton for the insulation. The quadrant was represented by a total of 445 turns with a wire radius of 70 µm and an insulation thickness of 10 µm. The width of the rectangular core is 6.375 mm which represents half the thickness of the core in a realistic 3D configuration. A distance of 10 µm was chosen to separate individual windings, in fact, a perfectly wound coil would imply a zero spacing between windings but neither does this exist in reality due to manufacturing errors, nor does COMSOL allow modeling touching domains.
A free triangular mesh was selected for the entire geometry with a fine size[§§]. A boundary layer condition was added for the windings domains. This condition introduced two layers (each of 20 µm thickness) in the copper domains. Adding these mesh layers can help resolving the skin effect, especially at higher frequencies. The geometry included a total of 318323 elements. Figure 3.16, panel (a) shows the mesh quality for the whole geometry. Panel (b) shows the mesh quality for a magnified plot around the center.

3.6.2 Physics and solver

For this analysis, the magnetic and electric fields interface was used. This interface can be selected for modeling full coupling between electric and magnetic fields. For time harmonic fields within this physics interface, and based on the Ampere's Maxwell law, the two main equations solved for with the magnetic vector potential and the scalar potential (V) as dependent variables are:

$$(i\omega\sigma - \omega^2\epsilon_0)\boldsymbol{A} + \boldsymbol{\nabla} \times (\mu_0^{-1}\boldsymbol{\nabla} \times \boldsymbol{A} - \boldsymbol{M}) + (\sigma + i\omega\epsilon_0)\boldsymbol{\nabla} V - i\omega\boldsymbol{P} = \boldsymbol{J_e}\,, \tag{3.31}$$

$$-\boldsymbol{\nabla} \cdot ((i\omega\sigma - \omega^2\epsilon_0)\boldsymbol{A} + (\sigma + i\omega\epsilon_0)\boldsymbol{\nabla} V - (\boldsymbol{J_e} + i\omega\boldsymbol{P})) = 0\,. \tag{3.32}$$

With $\boldsymbol{P}$ for the electric polarization vector. In addition, the electric circuit interface was used to enable the current excitation and needed circuit elements. An AC current with an amplitude of 1 A was used. A parallel capacitor of 21 pF was connected to the coil's windings. The windings were modeled by defining an RLC (Resistive-Inductive-Capacitive) coil group feature[¶¶]. The study was computed in the frequency domain, starting from 200 kHz and until 10 MHz with steps of 20 kHz. A MUMPS[***] solver was selected and the study computational time was 7 hours.

[§§]Based on the default settings of a fine mesh as: a maximum element size of 6.51 mm, a minimum element size of 3.68 µm and a resolution of narrow region of 100%.

[¶¶]The RLC coil group feature takes advantage of the A-V formulation of the magnetic and electric fields features to take into account the in-plane electric current flow in the coil's current balance.

[***]For more information on the MUMPS solver, see the reference [54].

3.6.3 Results

In figure 3.17, the normalized electric field and a stream line plot for the electric potential at 760 kHz (left) and at 9 MHz (right) are shown. Figure 3.18, panel (a) shows the normalized magnetic flux density viewed in the 2D axial symmetric plane at frequency of 760 kHz. A 3D plot for panel (a) generated from revolving the plane around the symmetry axis is shown in panel (b). The magnified insets for the magnetic flux density around the center at 760 kHz and 9 MHz are shown in figure 3.19.
As the frequency increases, the skin effect becomes stronger and the current density is largely distributed around the surface domains of the conductors while it decreases exponentially towards the center. Figure 3.20 shows the normalized current density at at the two frequencies: 200 kHz (a) and 9 MHz (b).
The impedance of a single quadrant coil (Z_{coil}) is calculated from the study where the resistive, inductive and capacitive effects between coil's windings are included. The system's impedance (with the effect of the parallel capacitor C included) is calculated through:

$$Z_{\text{system}} = \left(\frac{1}{Z_{\text{coil}}} + i\omega C \right)^{-1} . \tag{3.33}$$

Similarly, the effective inductance of the full system (L_{system}) is calculated from:

$$L_{\text{system}} = \frac{\text{Im}\{Z_{\text{system}}\}}{\omega} . \tag{3.34}$$

Figures 3.21 and 3.22 show how the inductance and the impedance are changing versus the frequency for the quadrant coil only (green) and for the system of the quadrant coil plus 21 pF parallel capacitor (blue). Clearly, the effect of the parallel capacitance resulted in shifting the effective inductance of the system to a lower frequency value. The region until the inductance curve peaks up is called the inductive region. Crossing zero and switching to a negative value means that the reactance becomes negative and the system belongs to the capacitive region. On the right of figure3.21, a magnified plot of the inductance curves in panel (a) up to 1 MHz is shown. The inductance is close to what was resulted in section 3.3 where the inductance was around 350 µH at the frequency of 750 kHz (see table 3.2) which verifies differently that results from the 2D axisymmetric approximation are close to those obtained from the 3D analysis in the frequency domain study.
The effect of the parallel capacitance on the impedance resulted in shifting the impedance curve to a lower frequency range, it has also changed the amplitude.

Theoretically, the coil turn number plays a major role in defining its inductance, for this, the same study was repeated with different number of turns. A coil with 164 windings, each with a wire diameter of 0.45 mm and an insulation thickness of 10 µm was modeled. The system's effective inductance and impedance are shown in Figure 3.23. From the resonance curve, it can be seen that the **S**elf **R**esonance **F**requency (SRF) has changed in accordance (in comparison with a coil with a turn number of 445).

The same coil with a turn number of 164 was used to investigate the effect of the spacing between the individual windings on the coil's inductance. The same analysis in the frequency domain was repeated for the three cases of uniform spacing between the turns (10 µm, 20 µm and 30 µm). The results are shown in figure 3.24. It can be seen that the greater the windings' spacing, the lesser the resulting coil's inductance, which makes an agreement with the theoretical expectations as the inductance should decrease with more windings pitch distances [55].

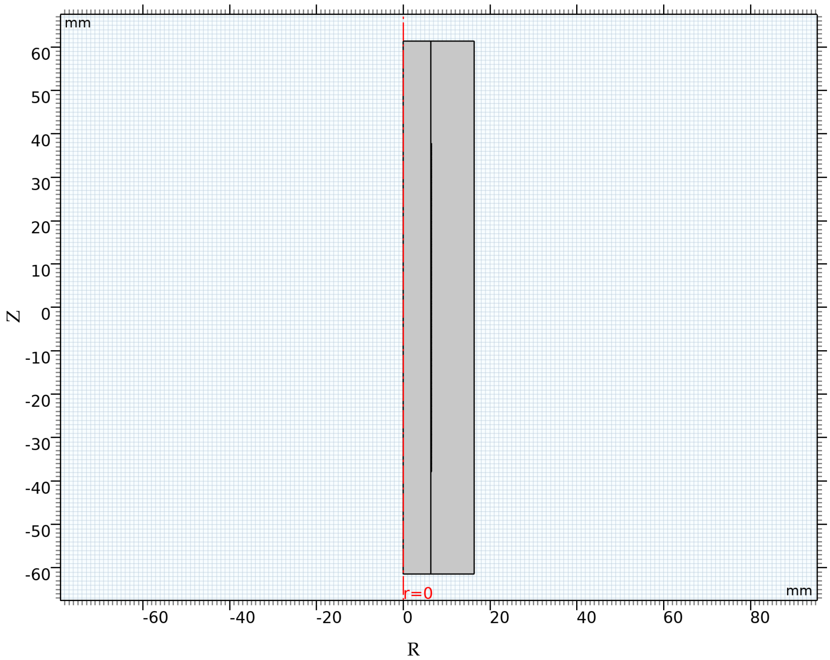

(a)

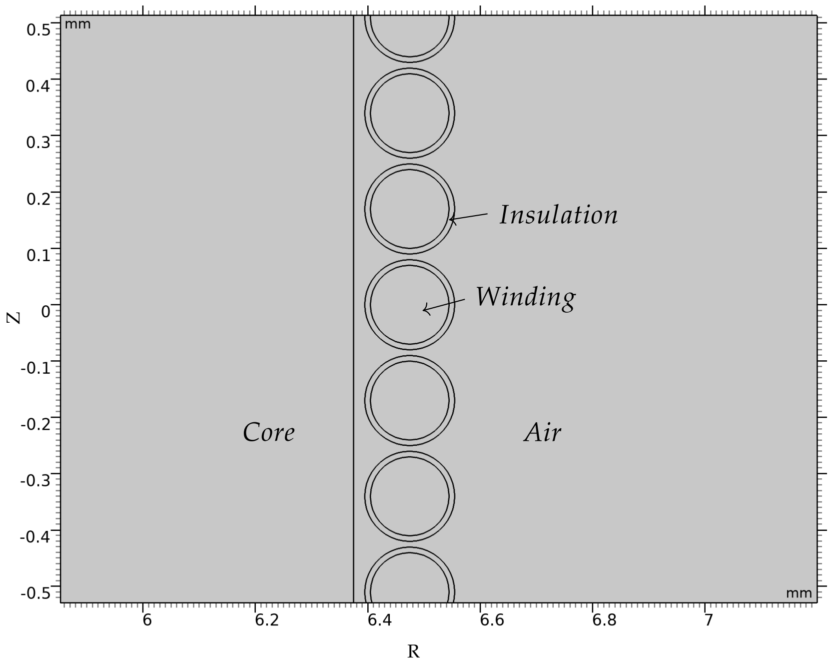

(b)

Figure 3.15: The full geometry of the 2D axisymmetry study as an approximation for a single quadrant coil (a). A magnified picture for the same geometry in (a) around the center (b). The two arrows are pointing to the insulation and windings' domains. The right rectangular side represents the air domain, the left rectangular side represents the core domain. The horizontal axis is represented by the radial R distance and the vertical axis is represented by the longitudinal Z distance.

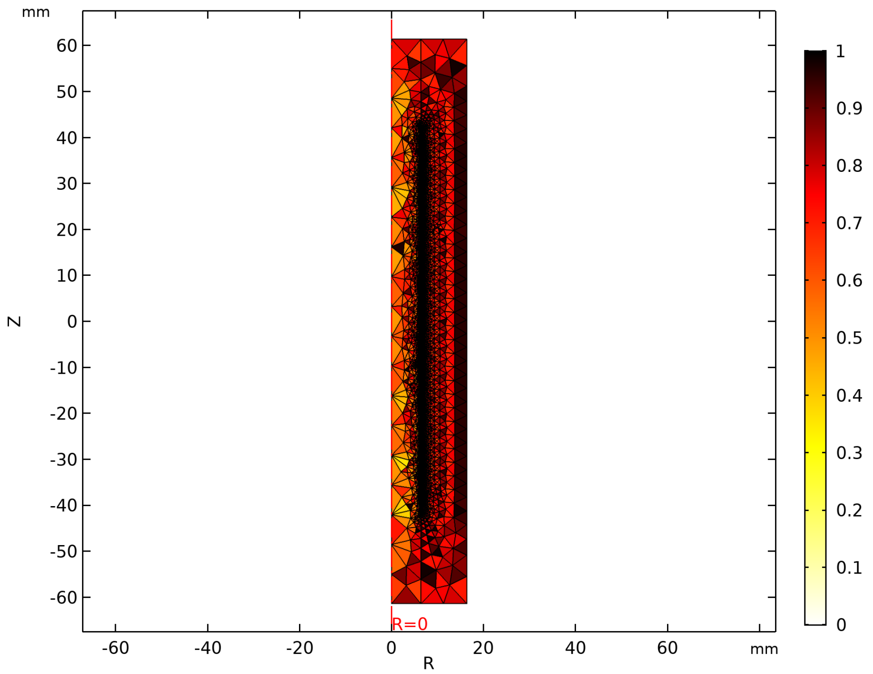

(a)

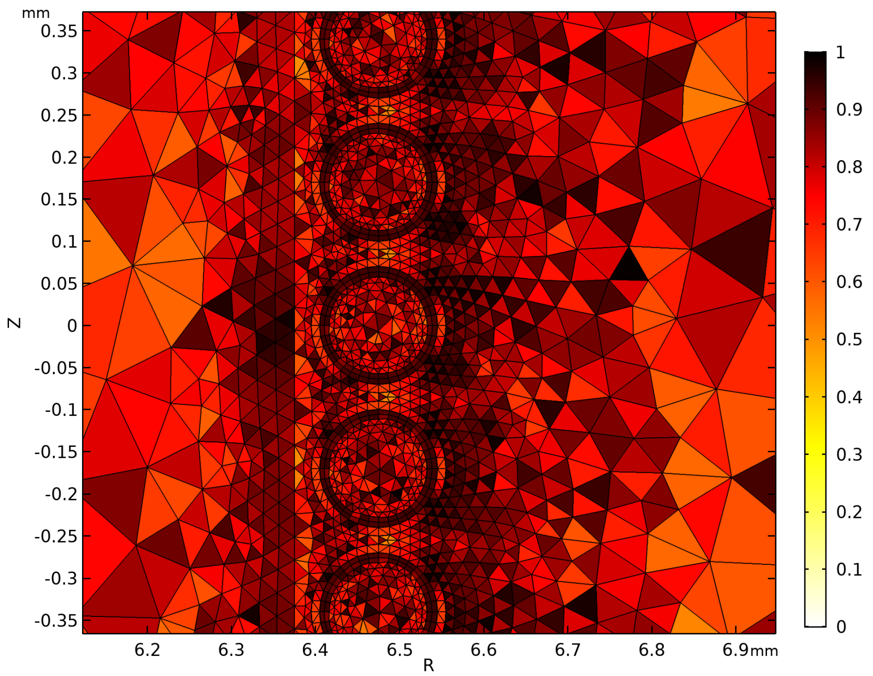

(b)

Figure 3.16: Mesh quality and structure of the entire 2D axisymmetry geometry. The red vertical line represents the axial symmetry line (a). A magnified plot around the center for mesh quality and structure (b). The color legends indicate the elements' quality from low (0) to high (1).

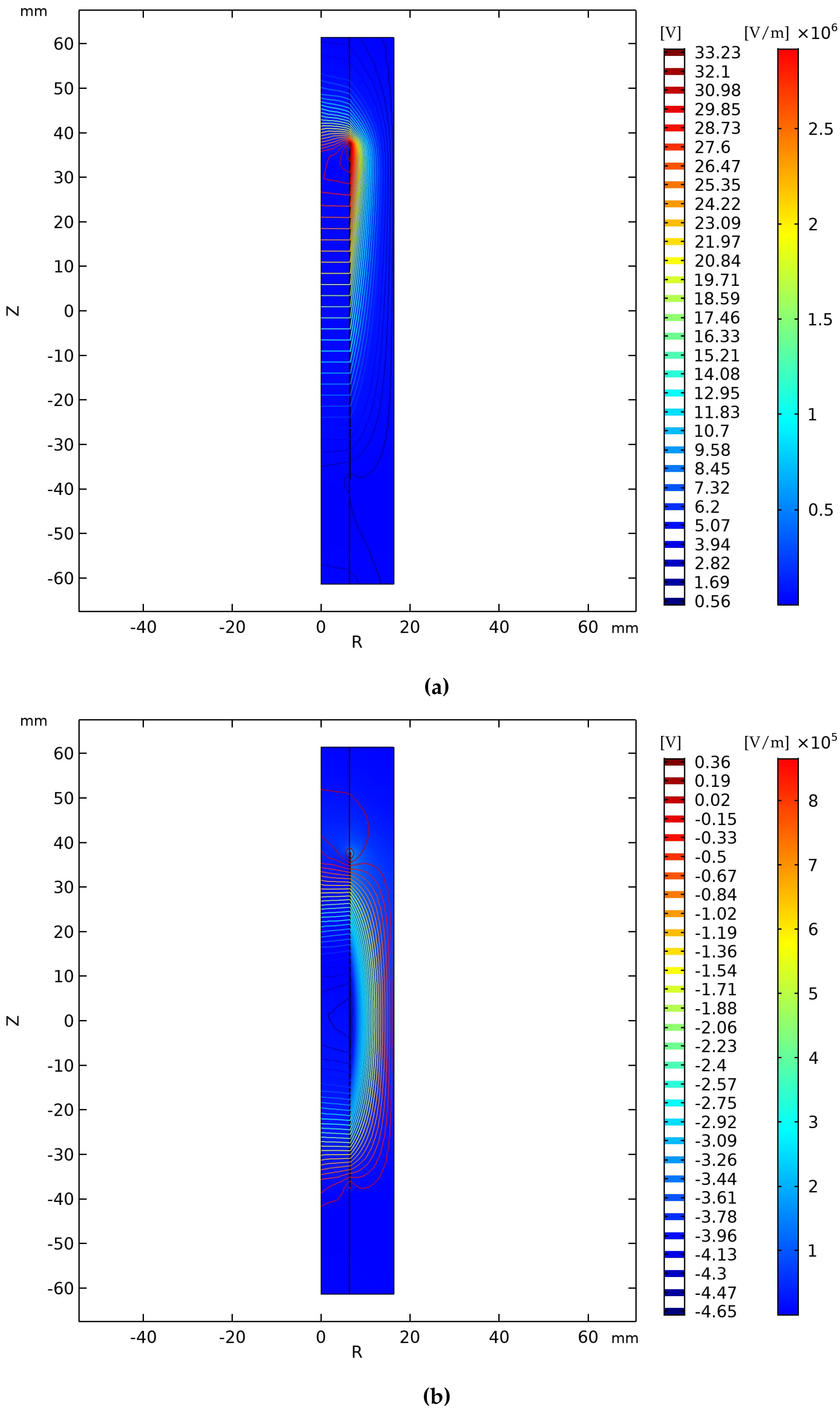

Figure 3.17: The normalized electric field and a stream line plot of the electric potential at 760 kHz (a) and at 9 MHz (b).

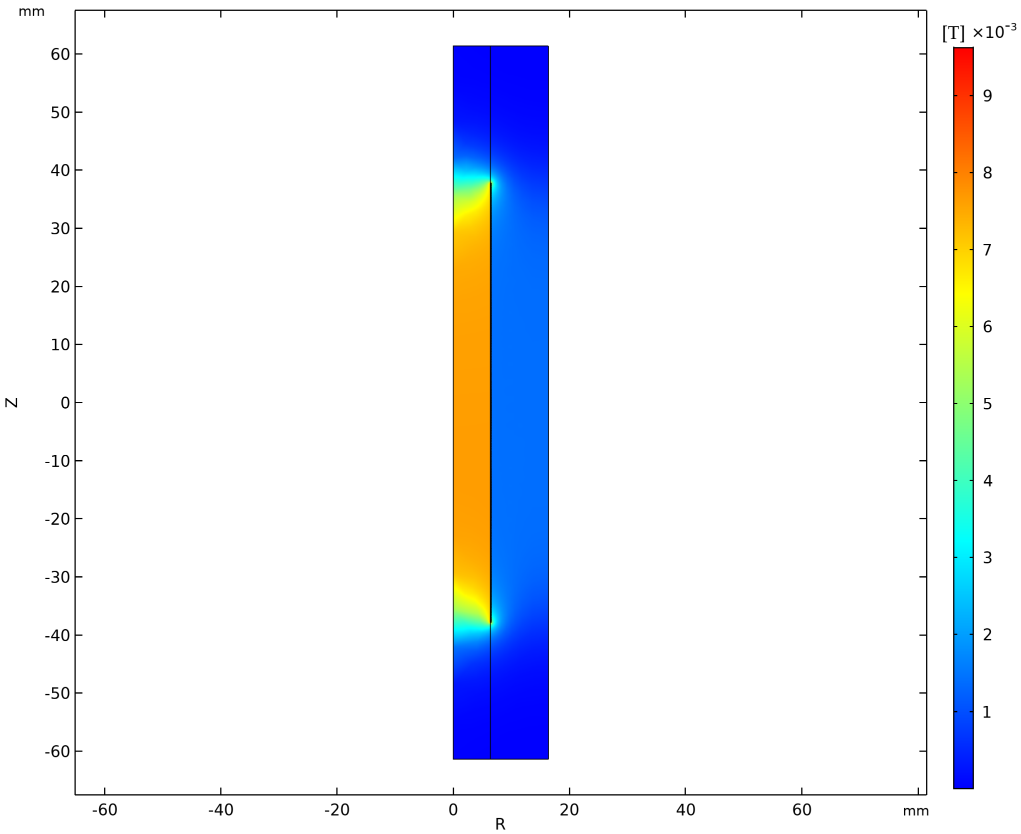

(a)

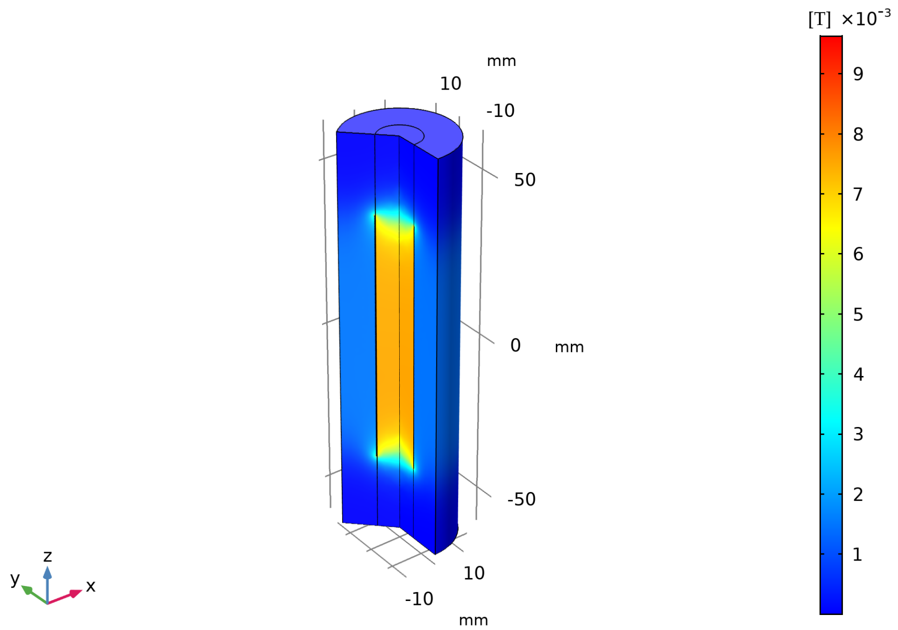

(b)

Figure 3.18: The normalized magnetic flux density viewed in the 2D axial symmetric plane at the frequency of 760 kHz (a). A 3D plot for panel (a) generated from revolving the plane around the symmetry axis (b).

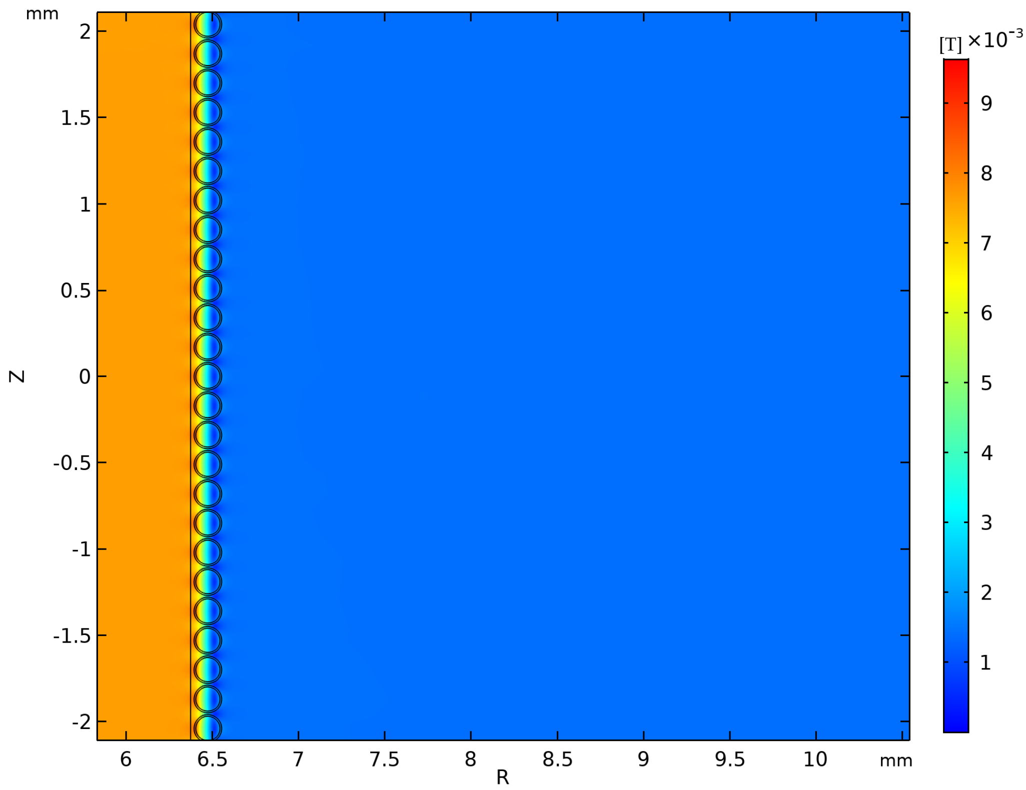

(a)

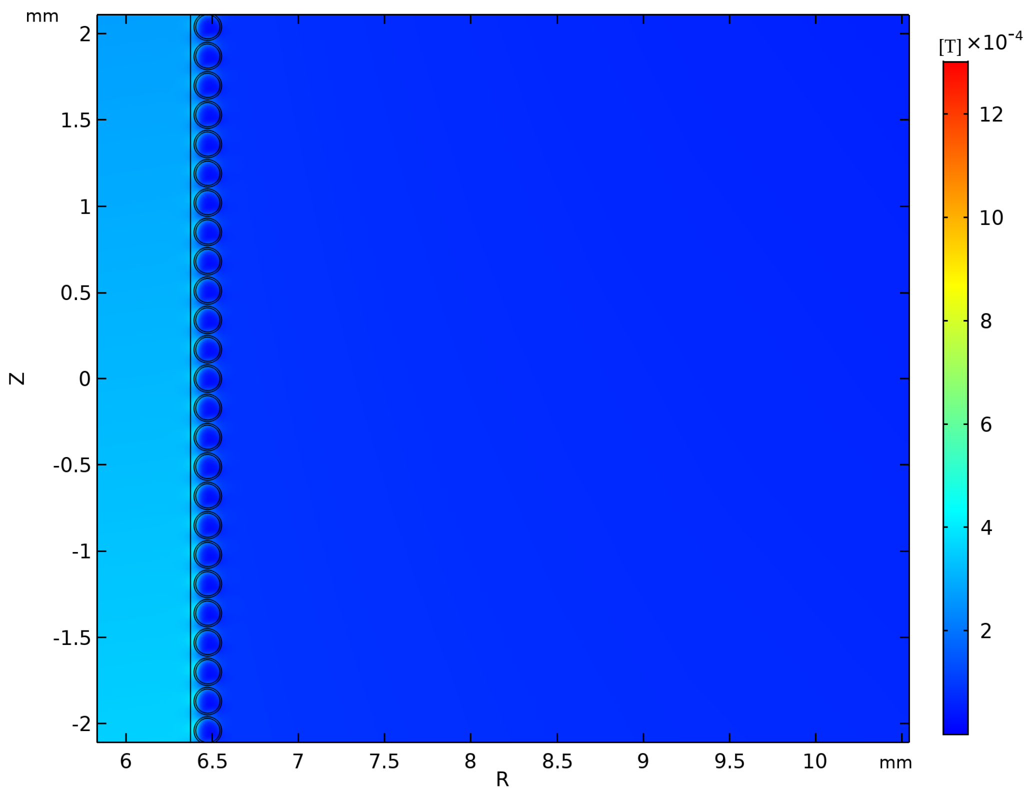

(b)

Figure 3.19: A magnified inset for the normalized magnetic flux density around the center viewed in the 2D axial symmetric plane at the frequency of 760 kHz (a) and at the frequency of 9 MHz (b).

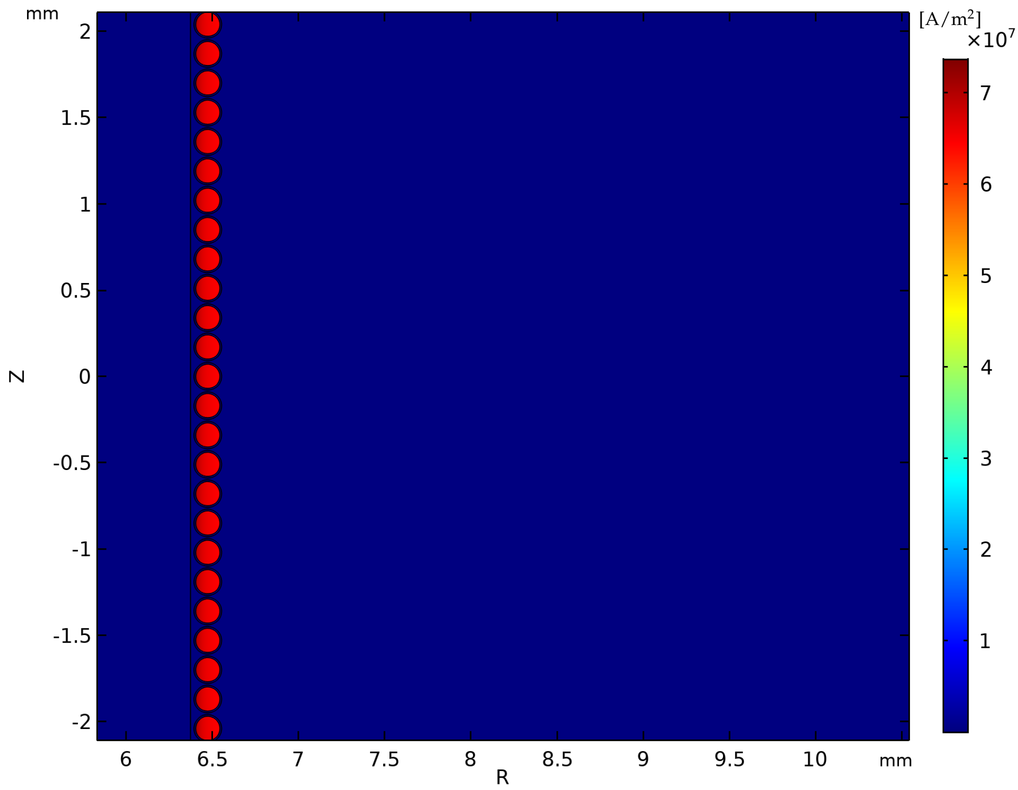

(a)

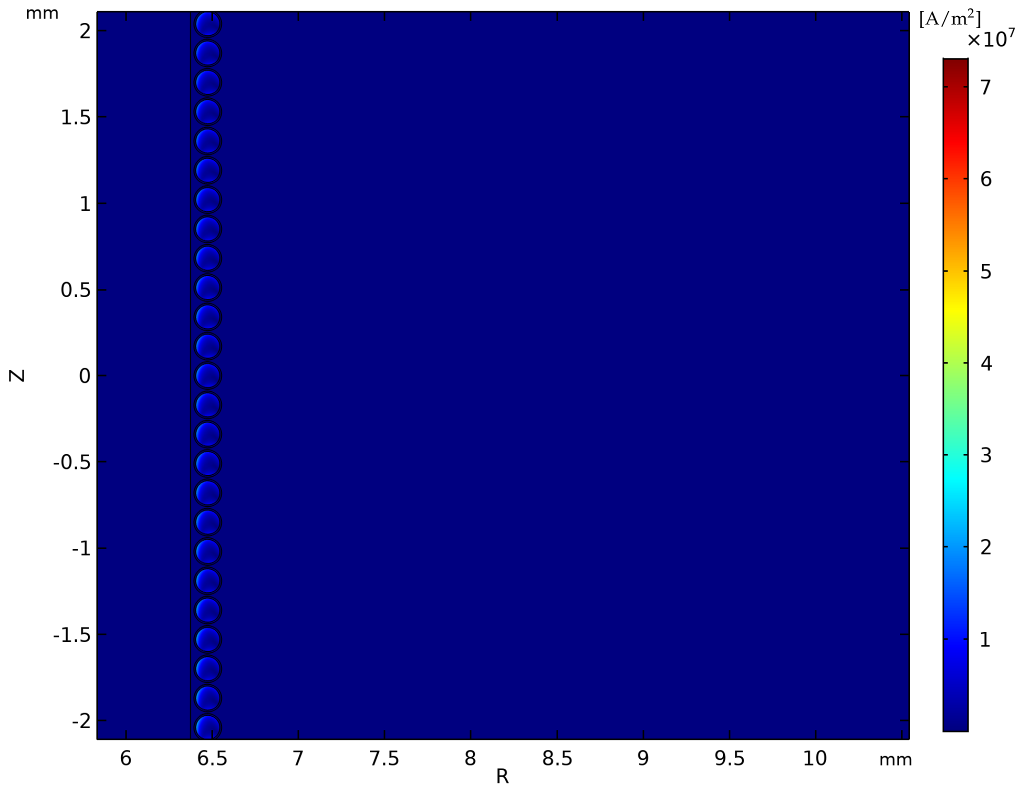

(b)

Figure 3.20: The normalized current density at 200 kHz (a) and at 9 MHz (b). The skin effect becomes strongly visible as the frequency increases.

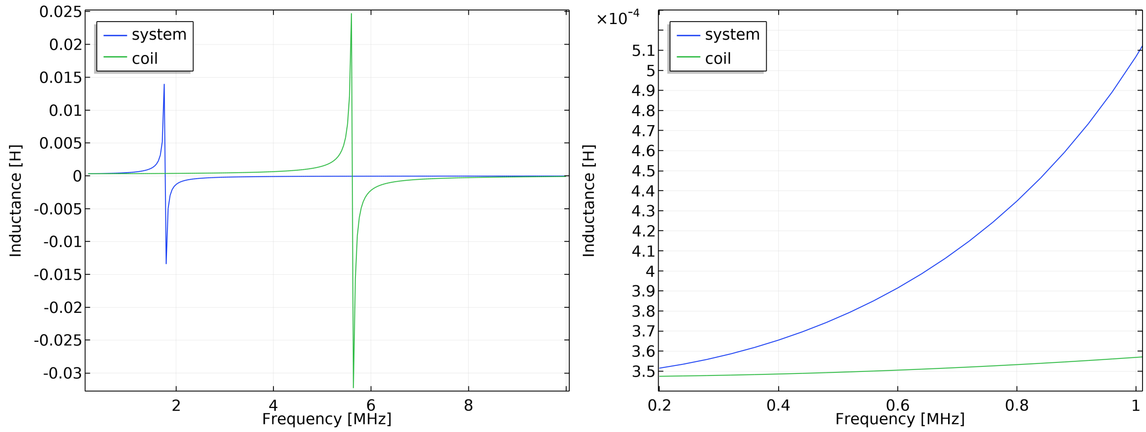

(a) **(b)**

Figure 3.21: Left: the inductance versus the frequency for the quadrant coil only (green) and for the system of the quadrant coil plus a 21 pF parallel capacitor (blue). Right: a magnified inset for inductances in panel (a) up to 1 MHz.

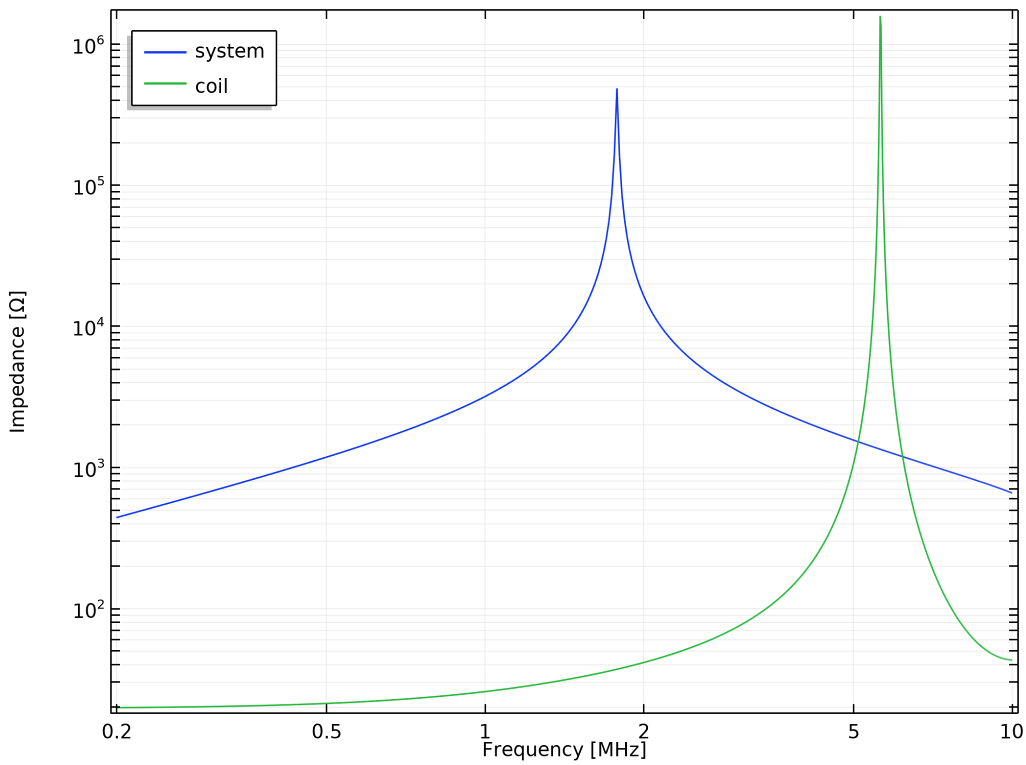

Figure 3.22: Impedance versus frequency for the quadrant coil only (green) and for the system of the quadrant coil plus a 21 pF parallel capacitor (blue).

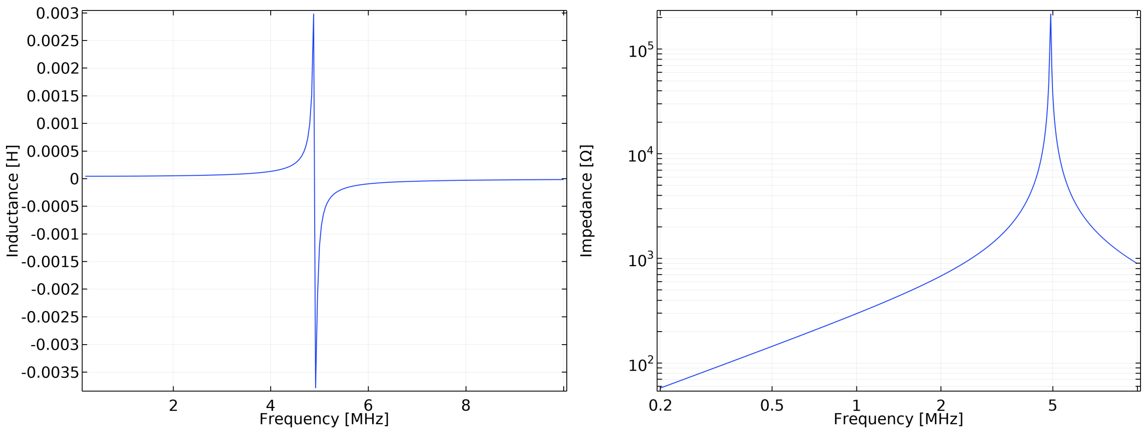

(a) **(b)**

Figure 3.23: The effective inductance (a) and the effective impedance (b) versus the frequency for a Rogowski quadrant coil with 164 windings (see eqs. 3.33 and 3.34).

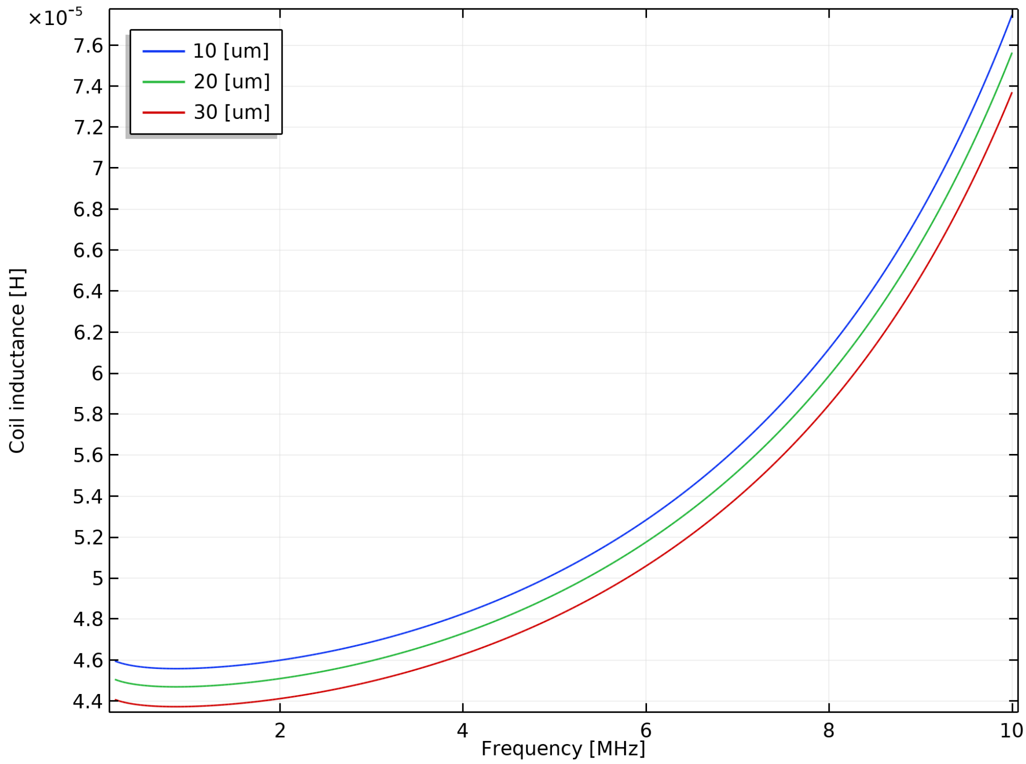

(a)

Figure 3.24: The inductance versus the frequency for a Rogowski quadrant coil with 164 windings using three sets of windings' spacing; 10 µm, 20 µm and 30 µm represented in blue, green and red curves, respectively.

Chapter 4

Experimental realization

This chapter describes several experimental aspects. A general description of how the Rogowski BPM is usually assembled is given. Developments in the laboratory test-stand and the vacuum test-stand, details on the procedure of the calibration measurement and a description for the device absolute calibration are also introduced.

4.1 Device assembly

The first step in building the Rogowski BPM starts with the winding process where the four separate quadrant coils are wound around the PEEK core. In order to provide mechanical stability for the wound coil (winding-core combination), a pair of PEEK clamping rings is used where the wound coil is placed in between and fixed (also using special PEEK screws) on the top of a steel CF-160 flange. Four CF-16 nipple tubes are then connected to the sides of the flange (over which the coil is supported). The end sides of these nipple tubes are connected to CF-16 SMA feedthroughs. For transmitting the analog signal, each quadrant coil has a 10 cm long twisted-pair extension which is connected to a 16 cm long coaxial cable that goes inside the nipple tubes until the outside SMA connection point. The assembly is usually made inside a clean room to secure good vacuum compatibility. Figure 4.1 shows a photograph of the winding-core combination inside the clean room during the device assembly. Figure 4.2 shows the Rogowski BPM in its final assembled form with complete flanges and signal feed-through connectors, where the connections to the pre-amplifiers and processing electronics are usually made.

Figure 4.1: A photograph of the Rogowski winding-core combination inside the clean room during the device assembly.

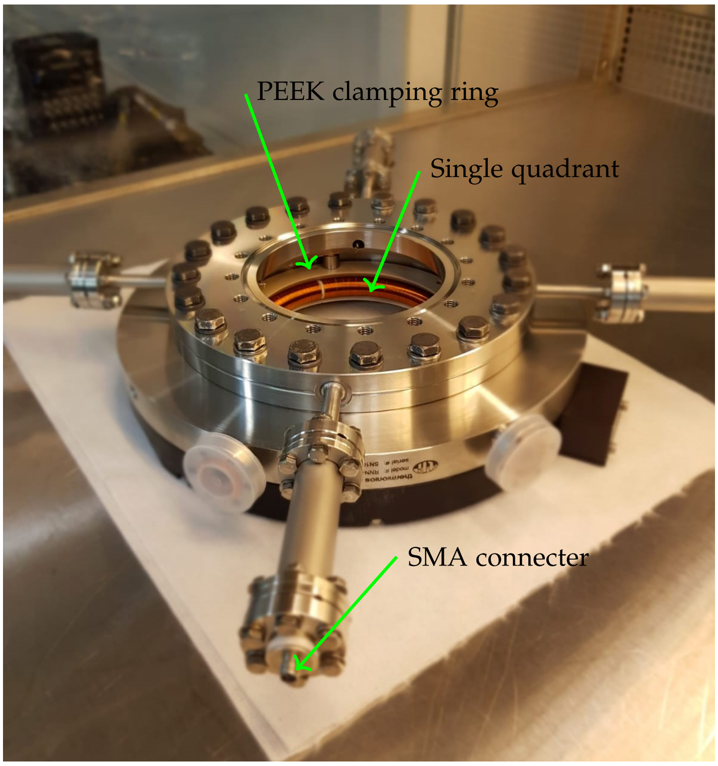

Figure 4.2: A Rogowski BPM in its final assembled form. The Arrows are indicating the windings of a single quadrant, the PEEK clamping rings between which the coil is fixed and the SMA connector through which the connection to the pre-amplifier is usually made.

4.2 Test-stand of Rogowski BPM

A dedicated test-stand has been developed in the laboratory for the purpose of calibrating and testing the Rogowski BPMs prior to installation. A schematic of the measurement test-stand is shown in Figure 4.3. The BPM is mechanically supported and fixed on the top of two stepping drives. Two cylindrical flanges are connected to the two sides of the BPM to mimic a beam tube in COSY. The beam is mimicked by using a copper tin-coated wire suspended along the longitudinal axis ($\vec{z}$). This wire is about 1 m long and is terminated with a 50 Ω impedance. The other side of the wire is attached to a 500 g load to provide a good longitudinal alignment. The load is placed inside a damping water to avoid possible vibrations during the measurement. The beam signal is provided from a waveform generator* [56]. A sine waveform with a frequency of 750 kHz and an amplitude in the range of $0.01 - 1$ mA† is usually used for calibrating the Rogowski BPM. The selection for this particular frequency and current range is linked to the COSY beam momentum‡ of 0.97 Gev/c and a usual number of particles in the range of $10^8 - 10^{10}$. The manual tables provide further adjustment for the alignment of the copper wire. The stepping drives [59] are used to move the coil in the xy-plane during a calibration measurement. These drives have a travel range of 200 mm, a load capacity of 60 kg, a positioning error of $5 - 6$ µm§ (denoted by σ_2 in subsection 5.4.6), a repeatability of < 500 nm and a linear measuring system with resolution of 50 nm.

*33500B True-form Wave form Generators, KEYSIGHT Technologies.

†Since the waveform generator drives a voltage signal, the inspected beam current is defined as the ratio of voltage amplitude and the beam line impedance measured at the operational frequency.

‡COSY accelerates and stores polarized and unpolarized beams in the momentum range $0.3 - 3.7$ GeV/c [57,58], which means a required operational frequency of the BPM system from few 100 kHz up to 1.6 MHz assuming the single bunch mode.

§Measured at a distance of 100 mm.

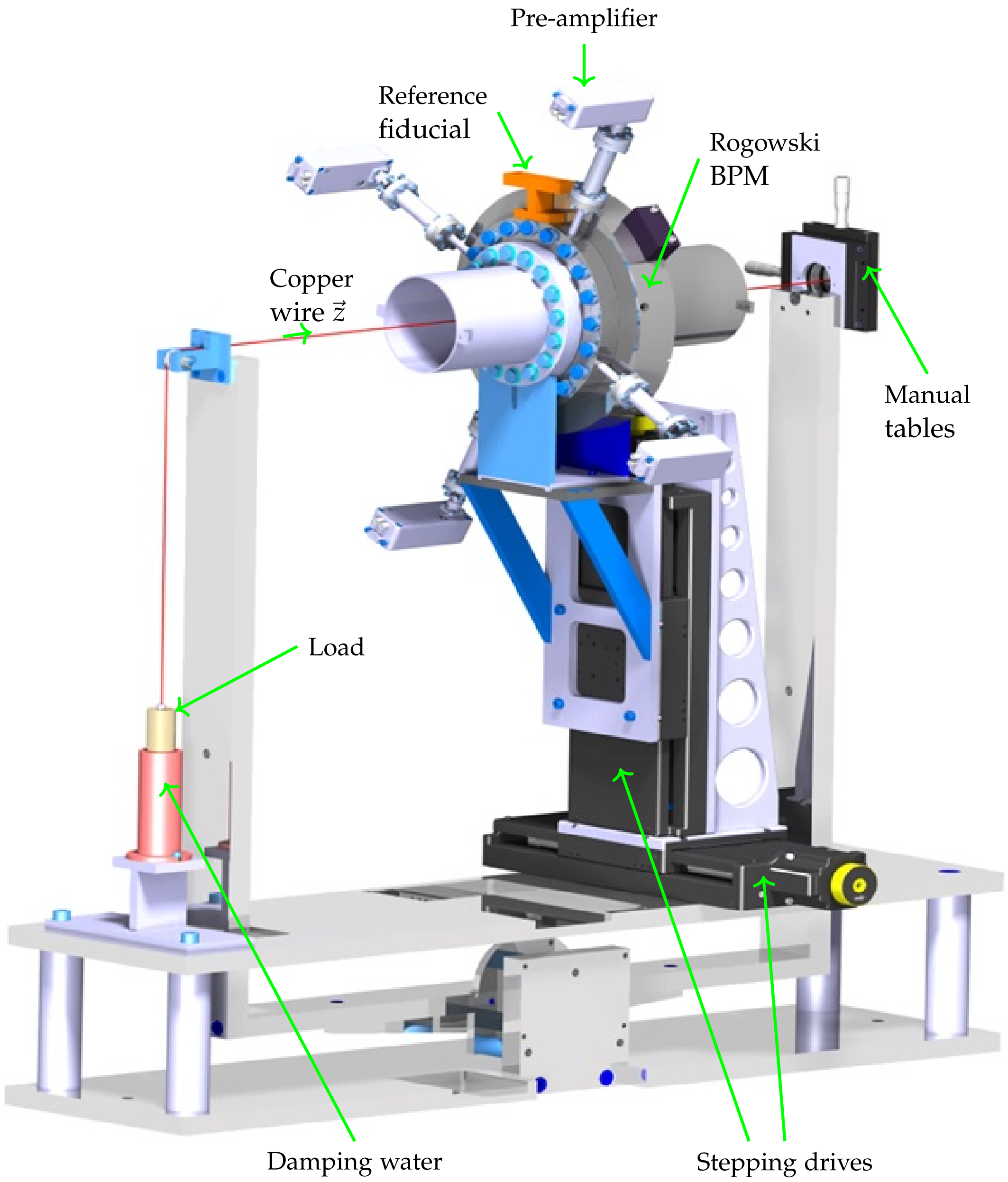

Figure 4.3: A schematic of the test-stand showing the Rogowski BPM on the top of two stepping drives (horizontal and vertical in the xy-plane). Each quadrant of the device is connected to a pre-amplifier which then takes the signal through a 2 m long cable to the lock-in amplifier device. The copper wire which mimics the beam line is attached to a 500 g load to provide a good longitudinal alignment. The load is placed inside a damping water to avoid possible vibrations during the measurement. The manual tables provide further adjustment for the alignment of the copper wire. Two reference fiducial points on the top of the device are used for absolute device calibration.

4.3 Absolute Rogowski BPM calibration

Absolute device calibration means calibrating the device where the beam positions are defined relative to some absolutely known coordinate system. This is usually done with the help of a special steel cylinder-like mechanical structure that has a disk-like knife edge from one side and planar disk with machined three fiducial spots on its surface from the other side (see Figure 4.4 part a). The geometry of this structure was determined on a mechanical measuring device in the central workshop of the Forschungszentrum Jülich to a precision of a few µm. This mechanical structure is longitudinally aligned and fixed inside one of the two tube flanges connected to the sides of the Rogowski BPM. The procedure of absolute device calibration is summarized in the following steps (see Figure 4.5 which summarizes these steps using vector representations):

- Once the mechanical structure is fixed and aligned inside one of the tube flanges as mentioned earlier, the stepping drives are programmed to scan the internal transverse plane around the knife edge. The physical location of the center of the knife edge is made to roughly coincide with the wound torus's centroid. This automated method enables finding the center of the knife-edged disk by scanning both transverse axes in both positive and negative directions and hence defining the plane's origin point. During the scanning process, the stepping drives stop the motion once an electric contact between the knife-edged surface and the copper wire takes place, this enables finding the upper most and lower most coordinates of the disk which then enables finding the center of the scanned plane with (the position of the wire when centered in the knife-edged disk). Because we are limited with the mechanical alignment of the cylindrical structure, this does not necessarily mean that the measured center is exactly equal to the geometrical center of the torus itself.
- After defining the center mentioned in the previous step, the drives are asked to move exactly to that returned center and with the help of the laser tracker [60], the positions of the three fiducial markers on the outer plane of the mechanical structure are measured. This enables defining a coordinate system (which is centered around the knife-edged disk) for the position of the wire in the disk's xy-plane. By the end of these two steps, the coordinates of the wire are defined (by the stepping drives) when centered in the mechanical structure (again not necessarily to coincide with the device's center) which will be used later as a fixed offset for distances traveled by the stepping drives during a calibration measurement. Additionally, the same center (by the laser tracker) is also defined in the real right-handed coordinate system which will be used in the next step.
- A special steel piece with two machined fiducial spots, is usually attached to the exterior body of the BPM device before the beginning of all the previous steps. The three Cartesian coordinates of these fiducial spots are determined now using the laser tracker with respect to the electrical center (the same center which was

measured by the laser tracker in the real coordinate system as stated in the previous step).

- When a calibration measurement is made, an additional offset between the beam positions and the geometrical center of the torus is retrieved by applying the theoretical model on the measured data. However this offset should be compatible with the degree of the mechanical alignment of the cylindrical structure inside the BPM device, which is another way of judging the reliability of the used theoretical model. By the end of this step, the vectors defined using the laser tracker for the positions of top fiducials can be redefined again with respect to the torus's own axis.
- When the device is installed in the accelerator environment, the vectors of the top fiducials are measured with the laser tracker again, but this time with respect to the COSY axis. Comparing these vectors in both the laboratory and the accelerator environments will define the offset between the COSY axis and the torus's axis.
- Since the BPM device is calibrated to return positions with respect to its own central axis, the offset determined in the previous step can be included so as to reconstruct final positions with respect to the COSY axis. With all these steps, the device's absolute calibration can be made possible.

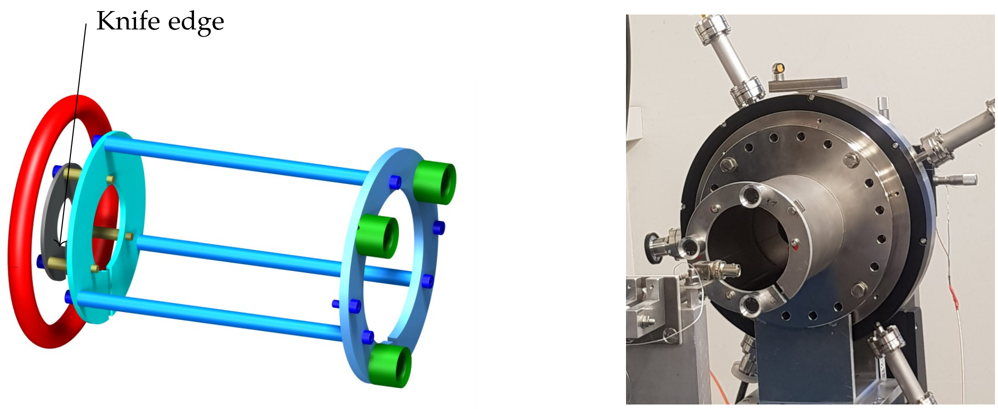

(a) (b)

Figure 4.4: A schematic drawing of the mechanical structure showing the knife-edged disk on the left and the other disk with the three machined fiducial markers on the right side (a). The picture for the Rogowski BPM with the mechanical structure inserted the BPM through during the procedure of absolute calibration (b).

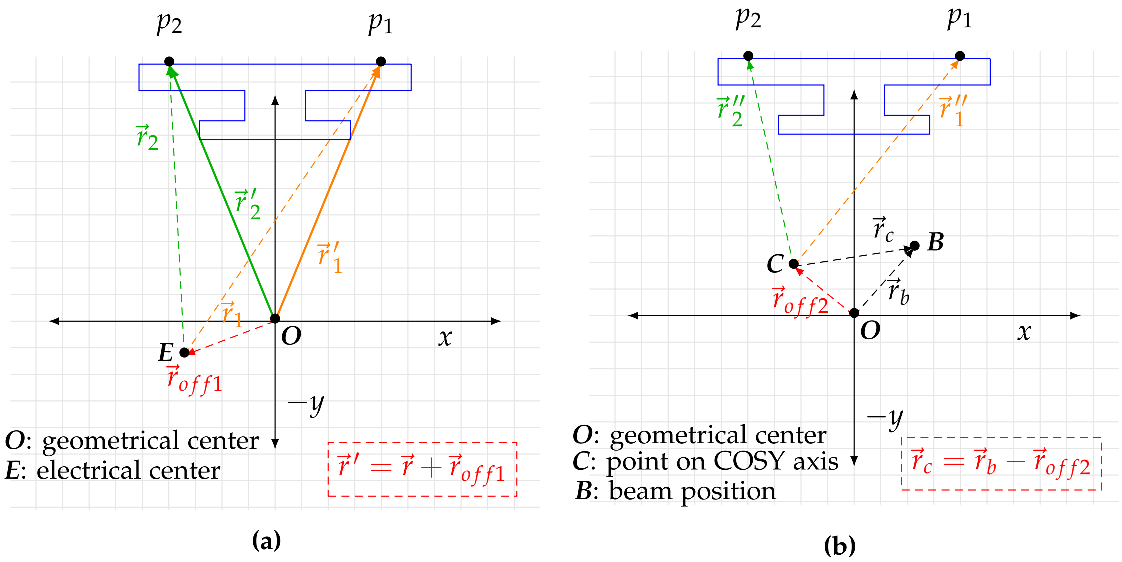

Figure 4.5: Vector representation in the xy-plane of the procedure for the absolute Rogowski BPM calibration. A representation of the beam positions in the lab environment and in the COSY environment are shown in the left and the right panels, respectively. The blue polygon represents a 2D cut in the xy-plane for the top steel piece with the two reference fiducials. In part a, the unprimed vectors are those defined by the laser tracker for the positions of the top fiducials with respect to some electrical axis (which is defined in a real coordinate system centered around the knife-edged disk ***E***). The offset vector is defined later after applying the theoretical model on the measured data from the calibration test. The primed vectors are also positions of the reference points but with respect to the BPM's central axis (***O***). In panel (b), the double primed vectors are positions of the reference points measured by the laser tracker with respect to the COSY central axis in the real coordinate system (***C***) after the installation process. The offset vector is calculated after comparing the double primed coordinates with the primed coordinates from panel (a). For the final beam positions with respect to the COSY axis, the vector $\vec{r}_c$ should be used.

4.4 Signal processing

Each quadrant coil is connected through an SMA connector to a pre-amplifier with a gain factor of 18 (measured at 750 kHz). In order to get the transient Rogowski coil's signal integrated, each pre-amplifier is connected through a 2 m long cable to an input in the lock-in amplifier device [61] where the signal is processed and measured. This digital lock-in amplifier permits input ranges from 1 mV up to 1.5 V with an input sensitivity down to 1 nV and a permissible frequency range of (0.7 µHz – 50 MHz). The built-in analog to digital converter has a 14-bit resolution. With these lock-in amplifiers, a dynamic reserve of up to 120 dB is reachable[¶]. A low pass filter with a roll of up to the 8th order is possible. The filter 3dB bandwidth can be as small as < 100 µHz and as large as a few hundreds of Hertz.[||] A bandwidth of 6.81 Hz is typically used within a fourth order low-pass filter in the Rogowski signal processing, this corresponds to a time constant of about 10 ms, however, in time domain scale, and due to delay, the demodulator would need about 10 times larger time to reach 99% of the final filtered output value, which means an averaging for about 76 thousand complete turns around the COSY ring. With the existing electronics, bunch-to-bunch monitoring would be possible if a first order filter was chosen with a 3 dB bandwidth of 200 kHz, however, on the other hand, the signal to noise ratio in this case will be much worse as the frequency window is bigger.

4.5 Vacuum test-stand

Vacuum refers to the state in which the pressure of a gas in a certain volume is much lower than the surrounding atmospheric pressure. **U**ltra **H**igh **V**acuum (UHV) is the vacuum regime characterized by pressures below 1.0×10^{-9} mbar. UHV conditions are created by pumping the gas out of a UHV chamber. At this low pressure the mean free path of a gas molecule is greater than approximately 40 km, so the gas molecules in the free molecular flow will collide with the chamber walls many times before colliding with each other [62–64].
The vacuum environment serves as a fundamental role in particle accelerators. Ultra high vacuum conditions are necessary to minimize gas-beam interactions, which can affect important parameters in particle accelerators as the beam lifetime, the background in the experiments, the trajectory speed of the particle and the radiation hazards related to stray particles [65,66].
The typical testing of the vacuum compatibility of any device prior to installation in the accelerator environment is a crucial procedure. Several precaution steps are usually taken in order to make the mission of achieving good vacuum easier, for example, the choice of separate materials and components used during the device assembly is based on the UHV compatibility condition. In addition, the cleaning process of the individual parts of the device also plays a role in this context.
Molecules landing on the surface of the Rogowski windings (or even the torus) can be adsorbed. In fact, for the Rogowski BPM, airborne water vapour is the main part in the adsorption layer (assuming a good handling in manufacturing steps and in cleaning stages) especially if the device was kept in the air for long times before the installation process. Adsorbed gases under certain conditions of temperature and pressure can be desorbed producing the main source of gas in vacuum systems. In order to get red of the

[¶]The dynamic reserve expresses the relation between the largest tolerable noise to the full scale required signal at the reference frequency. For example, if the required signal was 1 µV, a 120 dB dynamic reserve implies a noise level a million times bigger can be tolerated without affecting the signal accuracy within the specified bandwidth.

[||]Minimum and maximum permissible bandwidths are also subject to the chosen filter order.

surface contamination caused by water vapor molecules, the Rogowski BPM is usually being baked at the time of the vacuum testing up to a temperature of 120 °C. The coil bake-out process usually lasts from few days up to two weeks, depending on the default pressure. After the bake-out process, a pressure down to the level of 1×10^{-9} mbar is usually reached.
A new vacuum test stand has been developed in the laboratory for the purpose of testing the vacuum compatibility of the Rogowski BPM prior to installation in the COSY ring. Figure 4.6 shows the experimental set up of this vacuum test-stand. Different parts of the test-stand such as the vacuum chamber, the storage chamber, the pressure gauges** [67,68], the **Q**uadruple **M**ass **S**pectrometer (QMS)†† [69], the leak detector‡‡ [70], the pump stand§§ [71], the separation valve, the heat controls¶¶, the temperature and pressure readouts and the Rogowski BPM are shown and labeled on the figure.

**Balzers TPR 018 Pirani gauge for pressures down to 10^{-3} mbar for pump down and Balzers IKR 070 cold cathode gauge for high vacuum down to 10^{-10} mbar.

††Ametek Dycor LC-D200M.

‡‡Balzers Instruments, QualyTest HLT260.

§§Pfeiffer HiCube 300, combined membrane pump (for vacuum) and turbomolecular pump (high vacuum).

¶¶HORST heating controls.

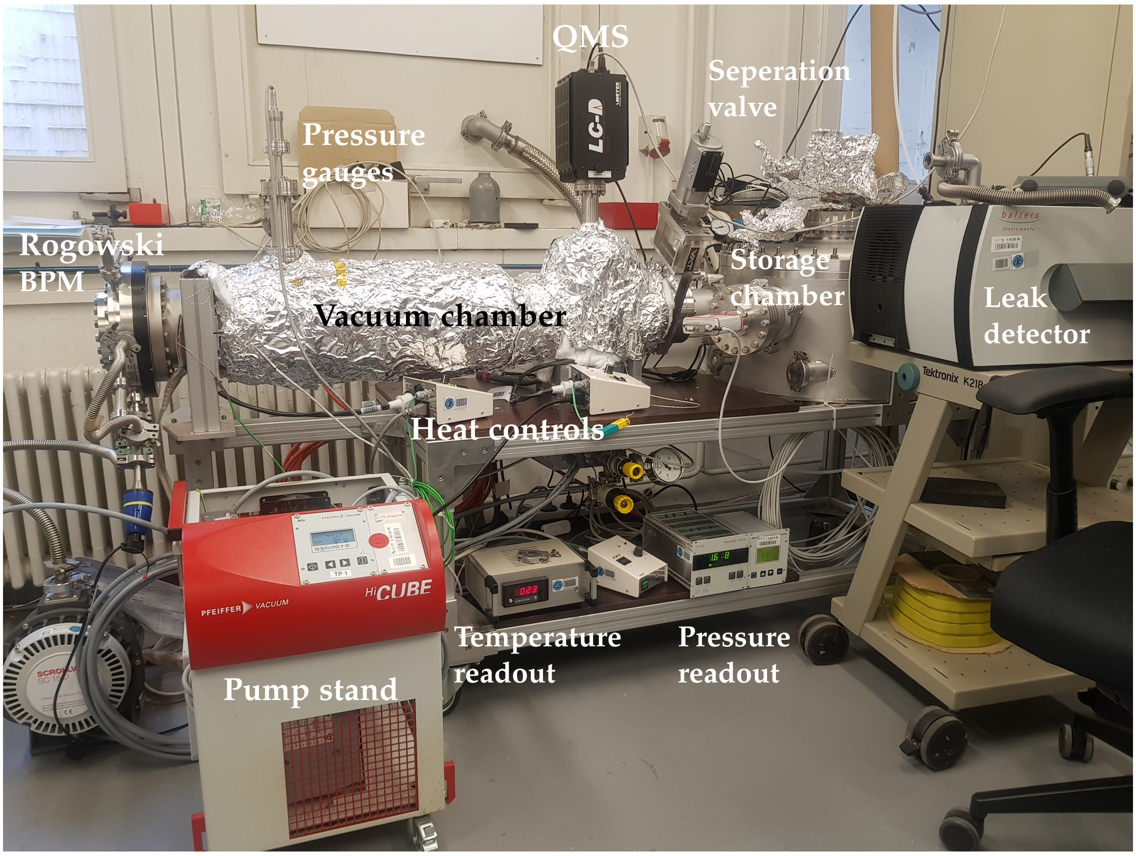

Figure 4.6: Experimental set up of the vacuum test-stand used for testing the Rogowski BPM prior to installation in the COSY ring. Different parts of the test-stand such as the vacuum chamber, the storage chamber, the pressure gauges, the QMS, the leak detector, the pump stand, the separation valve, the heat controls, the temperature and pressure readouts and the Rogowski BPM are shown and labeled on the figure.

Chapter 5

Measurements in the laboratory

5.1 Frequency response

One of the important features that is worth investigating is the frequency response of the single quadrants (which are simply inductor coils) through which the voltage, impedance or lumped elements can be studied in terms of frequency. The resonance structure was measured for each quadrant coil by changing the applied frequency of the AC source and keeping constant values for the rest of the parameters that the measured induced voltage depends on (see figure 5.1 which shows a schematic of the measurement's electrical circuit). Figure 5.2 shows how the induced voltage varies with the source frequency for the four quadrants as measured by the lock-in amplifier. In this measurement, the **D**evice **U**nder **T**est (DUT) included the complete typical Rogowski BPM system where single quadrants, cables and pre-amplifiers are all included.
The effect of electromagnetic coupling between the quadrants is clearly shown around the SRF where the inductance usually peaks up. Tuning the single coils by adding shunt capacitors can help getting the four coils to resonate at the same frequency point which can omit the additional peaks caused by the other coils around the resonance. This procedure also ensures more stability for the system in the long term. Beyond the SRF, capacitive effects become more dominant and the coil stops behaving as an inductor [72,73] *. In fact, this should define the operational bandwidth for such a device to act only as inductor where the energy is stored in magnetic fields. Figure 5.3 shows the measured resistance, inductance and capacitance of a single quadrant coil (similar to the quadrant coils in Figure 5.2) measured by the network analyzer [74] at different frequencies. In this measurement, a full port calibration was made before the test started, meaning that the DUT included the single quadrant coil plus the 16 cm long coaxial cable only.

*The coil's own capacitance can be neglected compared to that from the attached cables in the measurement, where most of the capacitance contribution that usually rises beyond the SRF is coming from.

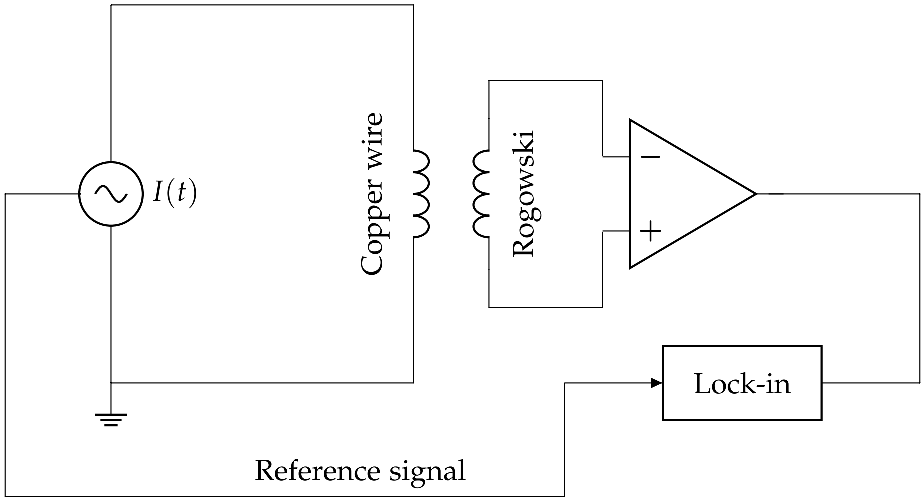

Figure 5.1: A schematic of the electrical circuit of the Rogowski's voltage measurement in the test-stand. The schematic describes all voltage measurement related tests, including the frequency response and the calibration measurement.

To understand the agreement between the measurement and the theoretical model (only as a function of frequency) a single quadrant test coil with 164 windings and a wire diameter of 0.45 mm[†] was investigated. The same measurement as that shown in Figure 5.2 was repeated for the single quadrant coil by varying the source angular frequency and measuring the resulting amplitude. Since the quadrant coil is solely wound around the torus, the governing equation of the response is eq. 2.9 rather than 2.11. Equation 2.8 was modified to account for some background signal which changes with the frequency:

$$U_{\text{out}}(x, y, \omega) = s\omega\gamma(\omega_0, \omega_1, \omega)\alpha + a\omega^3 + b\omega^2 + c\omega + d\,. \tag{5.1}$$

Eq. (5.1) was used in a minimization χ^2 method with ω_0, ω_1, a, b, c, d and s as fitting parameters (see Table 5.1). The factor s is added as a unit-less compensation factor that should equal unity if all given inputs were exactly as expected. These inputs are all frequency independent factors which are implicitly hidden in the α term such as the beam[‡] transverse positions, the amplitude of the beam current, the number of coil windings and the gain factor of the pre-amplifier. Based on the parameters listed in Table 5.1, this quadrant coil is having a quality factor of 81 and a resonance frequency ($\omega_0/2\pi$) of 3.375 MHz. In fact, this resonance frequency value makes a good agreement with the expectations according to the results of the complete four-quadrant coils' measurement, where there in the latter, the quadrant of 445 windings resonated around 1.2 MHz, and a decrease of the quadrant's turn number by a factor of 2.7 should correspond to an increase

[†]Only one single quadrant wound around a PEEK torus without the remaining three neighboring quadrants.

[‡]Whenever the beam is mentioned for tests and measurements carried out in the laboratory, it refers to the excited source or the copper wire which is used to mimic the beam there.

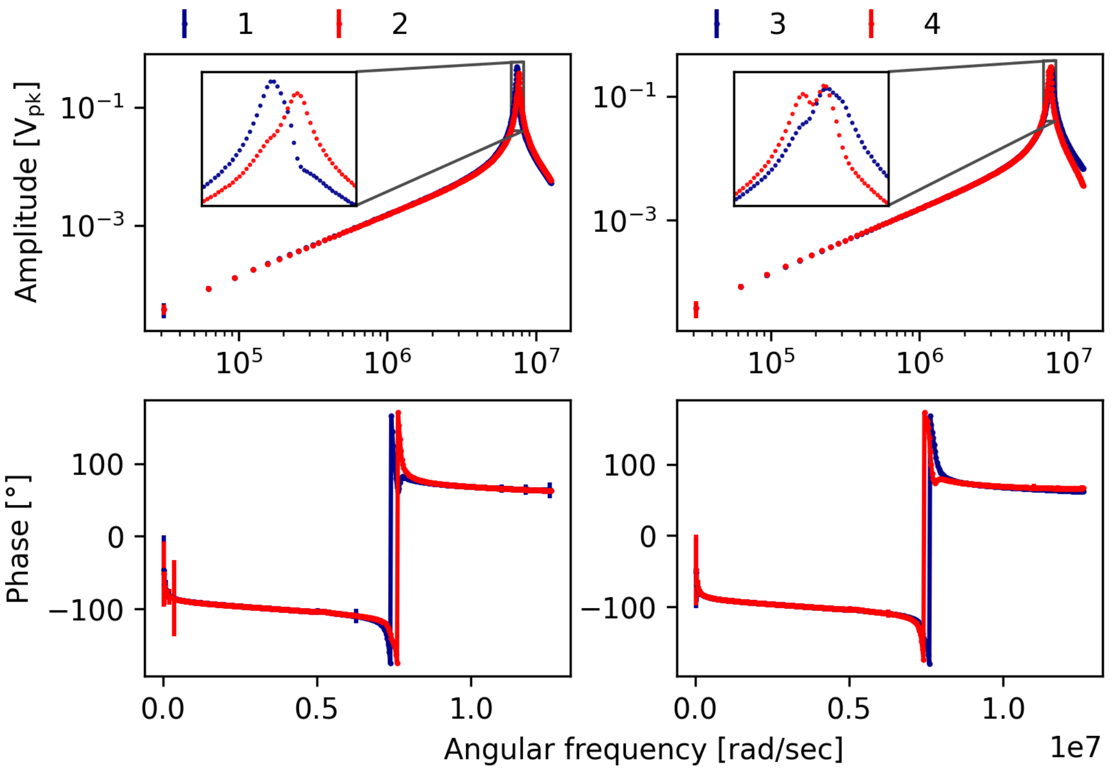

Figure 5.2: The measured frequency response from the four quadrants of the Rogowski BPM. The left two plots show the amplitude (upper) and phase (lower) responses of the quadrants one and two. Similarly, the right two plots show the amplitude (upper) and phase (lower) responses of the quadrants three and four. Electromagnetic coupling between single quadrants is clearly visible around the self resonance frequency. The data entries belong to a sampling time of 1 second. The amplitude's and the phase's error bars are multiplied by a factor of 100 and 20, respectively.

by a similar factor in the resonance frequency.[§]. The value of the parameter s means that there was an uncertainty of about 6% in the value of the frequency independent user-defined inputs, as stated earlier.
Figure 5.4 shows both the measured and fitted frequency responses from the solely wound quadrant coil. The fit function is based on eq. 2.8 (panel (a)) while is governed by eq. 5.1 (panel (b)) with a polynomial background included. In each panel, the lower subplot shows the difference between the measured and the fitted data points. The error bars represent the measurement errors multiplied by a factor of 100. When the polynomial background was added, the residuals were improved by a factor of five.

[§]This is assuming that the capacitance barely changed, as the measurement cables (which are the same in both measurements) are the major source of this capacitance compared to the two quadrants self capacitance.

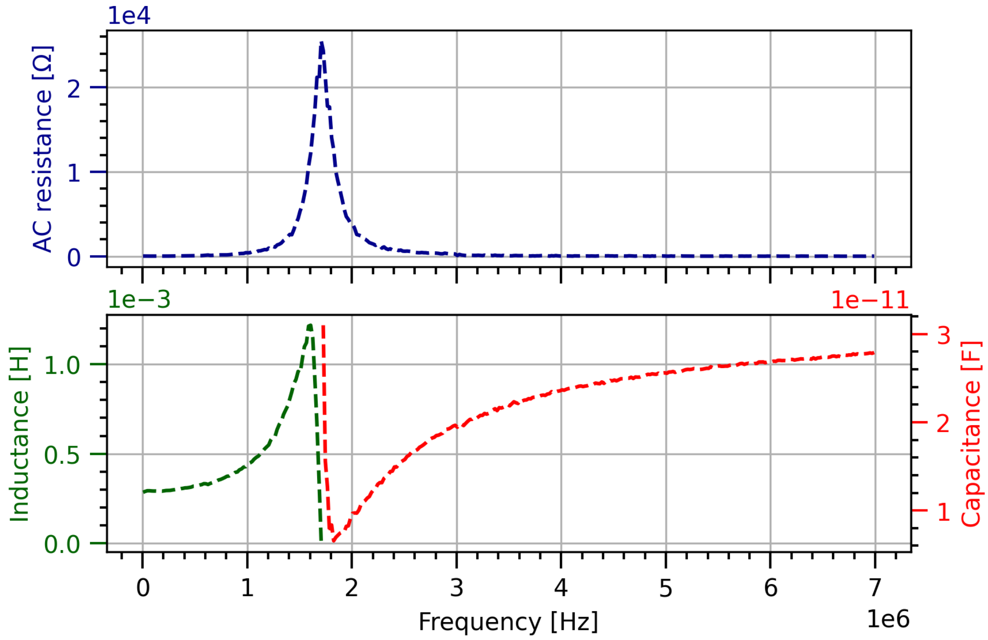

Figure 5.3: AC resistance (upper subplot), inductance and capacitance (lower subplot) of one single quadrant plus 16 cm long coaxial cable calculated through the impedance as measured by the network analyzer. Full port calibration was made prior to measurement.

Table 5.1: The fit parameters obtained from the frequency response measurement (see figure 5.4) of the single quadrant coil with a turn number of 164 and a winding wire diameter of 0.45 *mm*.

Parameter	Value
ω_0	$(2.1206500 \pm 0.0000001) \times 10^7$ rad/s
ω_1	$(1.71754 \pm 0.00001) \times 10^9$ rad/s
a	$(1.1187 \pm 0.0001) \times 10^{-25}$ Vs^3/rad^3
b	$(3.3441 \pm 0.0005) \times 10^{-18}$ Vs^2/rad^2
c	$(-1.36925 \pm 0.00004) \times 10^{-10}$ Vs/rad
d	$(2.2673 \pm 0.0009) \times 10^{-5}$ V
s	1.055890 ± 0.000002

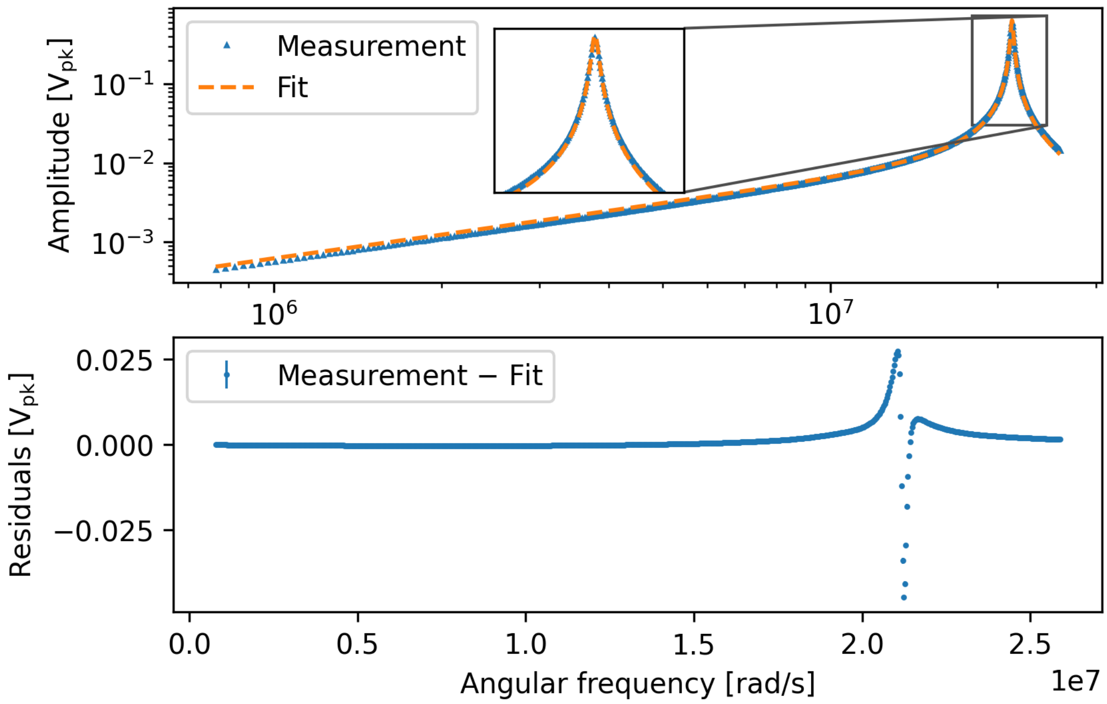

(a)

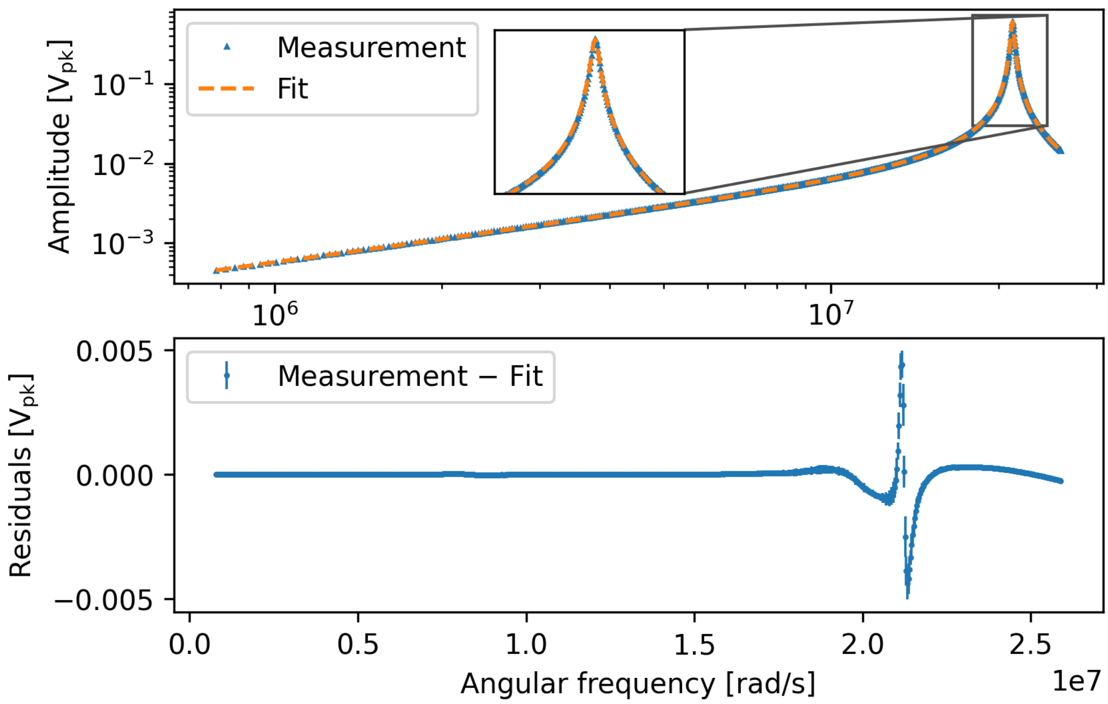

(b)

Figure 5.4: The measured frequency response from the solely wound quadrant coil. The fit function is based on eq. 2.8 (panel (a)) while is governed by eq. 5.1 (panel (b)) with a polynomial background included. In each panel, the lower subplot shows the difference between the measured and the fitted data points. The error bars represent the measurement errors multiplied by a factor of 100. When the polynomial background was added, the residuals were improved by a factor of five.

5.2 Calibration measurement

The main goal behind the calibration measurement is to provide a good knowledge about the device induction signals and how their levels relate to different beam coordinates. When calibrating the Rogowski BPM, an alternating signal is applied through the copper wire (which mimics the beam in the laboratory). The stepping drives over which the BPM is supported, are programmed in a way that the xy plane is scanned. A relative position will result for the copper wire each time a point is scanned. The amplified induced voltage from each quadrant is measured by the lock-in amplifier device. The reference frequency of the lock-in amplifier is provided from the external wave form generator (same generator that produces the excitation signal) as a **T**ransistor-**T**ransistor **L**ogic (TTL) signal through the **D**igital **I**nput **O**utput (DIO) source within the Lock-in device. To ensure a direct relation between the scanned positions and the measured voltages, the data polling starts only after 2 s from the end of the drives' motion. The size of positions mapped in a calibration measurement can vary up to the limit of the device's inner radius. Normally, a map of $(\pm 10, \pm 10)$ mm, with steps of 1 mm for both Cartesian axes is sufficient to calibrate the device.
For the calibration model, the theoretical expansions in eqs. 2.11 through 2.14 were used for describing the measured voltage signal from each quadrant accordingly. A combined minimization method was used in a model that considers all the voltage-position information from all quadrants at each scanned point. Few modifications were introduced for these four equations based on more realistic measurement conditions as the following:

- It is very probable that the center point measured by the calibrated stepping motors is not exactly producing a relative beam position which goes in the geometrical center of the BPM. This should imply a possible offset in both axes.

- It is also possible that the alignment of the wire along the longitudinal Z axis was tilted by some distance, this will also introduce an offset which adds to the previously mentioned one.

- It is possible that during the assembly of the device, or even at the time it was mounted on the test-stand, a rotation angle in the xy-plane was introduced. This will imply a rotational transformation of the transverse beam positions.

- Similar to the frequency response measurement, a unit-less factor describing the uncertainty in user-defined inputs shall be considered.

Based on the above mentioned possible conditions, eq. 2.11 becomes:

$$
\begin{aligned}
U'_{\text{out1}}(x',y',\omega) = \; & s_1 g_1(\omega)\omega\gamma_1(\omega_0,\omega_1,\omega)n\mu_0 c_0 I\Bigg[\bigg(1 + c_1(x'+y') + c_2x'y' + c_3(-x'^3 - y'^3 + 3y'x'^2 \\
& + 3x'y'^2) + c_4(x'^5 + y'^5 - 10x'^3y'^2 - 10y'^3x'^2 + 5y'^4x' + 5x'^4y')\bigg) \\
& + k_{12}\bigg(1 + c_1(x'-y') - c_2x'y' + c_3(-x'^3 + y'^3 \\
& - 3y'x'^2 + 3x'y'^2) + c_4(x'^5 - y'^5 - 10x'^3y'^2 + 10y'^3x'^2 + 5y'^4x' - 5x'^4y')\bigg) \\
& + k_{13}\bigg(1 + c_1(-x'-y') + c_2x'y' + c_3(x'^3 + y'^3 \\
& - 3y'x'^2 - 3x'y'^2) + c_4(-x'^5 - y'^5 + 10x'^3y'^2 + 10y'^3x'^2 - 5y'^4x' - 5x'^4y')\bigg) \\
& + k_{14}\bigg(1 + c_1(-x'+y') - c_2x'y' + c_3(x'^3 - y'^3 \\
& + 3y'x'^2 - 3x'y'^2) + c_4(-x'^5 + y'^5 + 10x'^3y'^2 - 10y'^3x'^2 - 5y'^4x' + 5x'^4y')\bigg)\Bigg] .
\end{aligned}
\tag{5.2}
$$

The above stated equation represents quadrant number 1 (see the relations in chapter 2 to construct the equations for the remaining quadrants). The γ, which should be constant for a constant beam frequency, has been given an index to distinguish between the separate quadrants (see table C.1 in appendix C for an estimate for γ at 750 kHz). Each quadrant was connected with a pre-amplifier with a gain factor of $g(\omega)$[¶]. In addition, the beam signal amplitude, beam angular frequency and the quadrant's turn number are all user known inputs which stay constant during the measurement time. The left hand side of eq. 5.2 is what the lock-in device measures from quadrant number 1 at the reference frequency (750 kHz). The prime notation in x and y comes from allowing for possible rotation and positional offsets:

$$x' = (x - x_{off})\cos(\theta) - (y - y_{off})\sin(\theta)\,, \tag{5.3}$$

$$y' = (x - x_{off})\sin(\theta) + (y - y_{off})\cos(\theta)\,. \tag{5.4}$$

Where x_{off} and y_{off} represent positional differences between the beam's electrical center and the BPM's (or more precisely, the toroidal coil's) geometrical center in the horizontal and vertical directions, respectively. The angle θ describes a possible rotation of the torus (winding) and/or the complete assembled device when mounted on the test-stand. The terms x and y stand for the transverse beam positions as scanned by the stepping drives and determined in a relative motion. The calibration algorithm takes in a combined

[¶]The gain factor changes with the frequency and it equals a value of around 18 at 750 kHz (see figure C.1 in the appendix C).

method eq. 5.2 and the remaining three equations for the other quadrants. This will result in a total of 19 unknown parameters; two positional offsets, one rotational angle, four unit-less compensation parameters, and twelve coupling coefficients (three for each quadrant). The values of these parameters are listed in Table 5.2. The small values of the offset parameters are in agreement with the attention that was given for aligning the copper wire during the measurement. The values of the compensation parameter s express that the substitution for the user-given inputs was wrong by 10% for quadrants 2 and 3 and by 7% for quadrants 1 and 4. In fact, some of these known inputs are common between the four quadrants but not all of them, i.e. if they were all common, then it would not make sense to have different values of s for the four quadrants. The gain factor for instance should not be common as we are referring to four distinct pre-amplifiers[11]. Also, the estimated γ factor is a non-common parameter which may hold some uncertainty. The values of the coupling factors (see eq. 3.18) were ranging from a few percent and a few per-mill. In fact, if the system was symmetric, or in other words, if the quadrants amplified responses were all the same for a beam passing through the center point, then one can expect that the coupling coefficients are also symmetric ($k_{ij} = k_{ji}$). But this is not the case here, i.e. a very small change in quadrants' responses as well as the pre-amplifiers' gains can justify why $k_{ij} \neq k_{ji}$ especially for opposite quadrant coils. The negative sign of the coupling coefficients implies two things; the first is that all the quadrant coils were having the same polarities, the second thing is that the fraction of the magnetic field lines (expressed through coupling factors) linking from the ith quadrant to the jth is in fact in an opposite direction to the net magnetic field on the jth quadrant, this also makes sense according to Lenz law, where the induced magnetic fields are generated in a direction that opposes the primary source causing them (excitation current source). The value of 1.8° for the rotational angle agrees with the precision reached in aligning the coil on the test-stand where a special leveling tool was used, as well as the care in aligning the torus during assembly time.

Figure 5.5 shows the results from one calibration measurement with 441 scanned grids in both transverse axes. Panel (a) shows the measured (blue) and the fitted (red) voltage ratios. The vertical ratios are plotted against the horizontal ratios. A very good agreement between the measurement and the theory can be seen. The theoretical model was based on eq. 5.2 and the corresponding remaining three equations for the other quadrant coils. The green-highlighted upper line of grids where the beam vertical position was constant at 10.15 mm while its horizontal position was varying from −8.71 mm up to 11.29 mm is plotted in panel (b) which clearly shows a non-linearity in the position dependence. The good agreement between measurement and theory is pictured through the residuals plot in figure 5.6 where the differences are on the level of a few μV_{pk}. The upper two subplots represent quadrants 1 (left) and 2 (right), the lower two subplots represent quadrants 3 (left) and 4 (right).

The level of deviation between the measured ratios and expectations (blue and red

[11] By 'distinct', a physical distinct is meant, they were manufactured to have the same gain, but in reality variations are possible.

Table 5.2: The fit parameters obtained from the calibration measurement (see figure 5.5), based on the theoretical model describing a realistic measured response from the four quadrants of the Rogowski BPM.

Parameter	Value
x_{off}	$(0.129 \pm 0.007)\ mm$
y_{off}	$(0.199 \pm 0.007)\ mm$
s_1	(0.9293 ± 0.0002)
s_2	(0.9008 ± 0.0001)
s_3	(0.9048 ± 0.0002)
s_4	(0.9333 ± 0.0002)
k_{12}	$(-1.5712 \pm 0.0087) \times 10^{-2}$
k_{13}	$(-9.27 \pm 0.04) \times 10^{-3}$
k_{14}	$(-5.347 \pm 0.091) \times 10^{-3}$
k_{21}	$(-1.3798 \pm 0.0087) \times 10^{-2}$
k_{23}	$(-1.3512 \pm 0.0091) \times 10^{-2}$
k_{24}	$(-1.41 \pm 0.04) \times 10^{-3}$
k_{31}	$(-5.713 \pm 0.038) \times 10^{-3}$
k_{32}	$(-2.440 \pm 0.089) \times 10^{-3}$
k_{34}	$(-7.081 \pm 0.086) \times 10^{-3}$
k_{41}	$(-6.560 \pm 0.088) \times 10^{-3}$
k_{42}	$(-1.588 \pm 0.004) \times 10^{-2}$
k_{43}	$(-6.7 \pm 0.1) \times 10^{-3}$
θ	(-31.026 ± 0.056) mrad

grids in Figure 5.5) in terms of transverse positions is displayed in Figure 5.7 where the differences between the measured positions and those calculated from the theoretical model are shown. The two sub-plot histograms represent the Probability Density Function (PDF) of the horizontal differences (down) and vertical differences (left). The central figure is a two-dimensional histogram of the differences in both transverse axes (vertical against horizontal). The $1 - \sigma$ covariance ellipse is drawn on the same central figure (red curve). Form the figure, a resolution of 142 nm and 103 nm is achievable for the horizontal and the vertical directions, respectively (considering the total of 441 entries according to $\sigma/\sqrt{441}$).
Developing a calibration model for later use of the Rogowski BPM in accelerators through which positions can be constructed can be either made based on using the previously mentioned voltage ratios or using the pure individual voltage signals from the four quadrants. The first method is more preferable as it is independent of the beam current amplitude as well as of beam wave form. In both of the two methods, one can rely on the theoretical model or use non-linear interpolations (lookup tables).

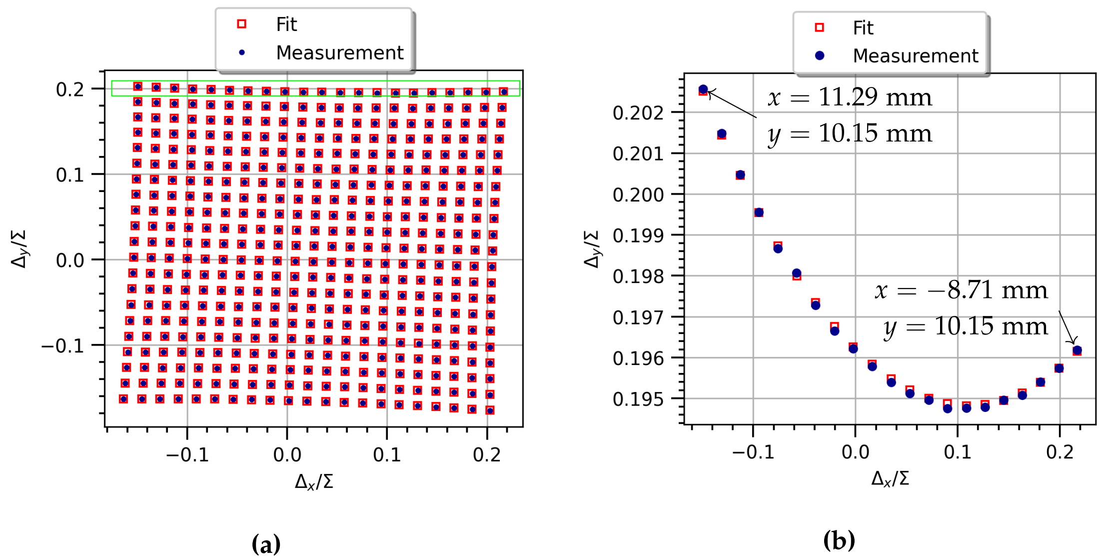

Figure 5.5: Panel (a): the measured (blue) and fitted (red) voltage ratios from one calibration measurement with 441 scanned positions in steps of 1 mm. The vertical ratios are plotted against the horizontal ratios. A bi-variate polynomial up to the 5th degree was used in a combined minimization method for describing the fitted grids (based on eq. 5.2 and the corresponding remaining three equations for the other quadrant coils). A very good agreement between the measurement and theory can be seen. The green-highlighted upper line of grids where the beam vertical position was constant at 10.15 mm while its horizontal position was varying from −8.71 mm up to 11.29 mm is plotted in panel (b) which clearly shows a non-linearity in the position dependence.

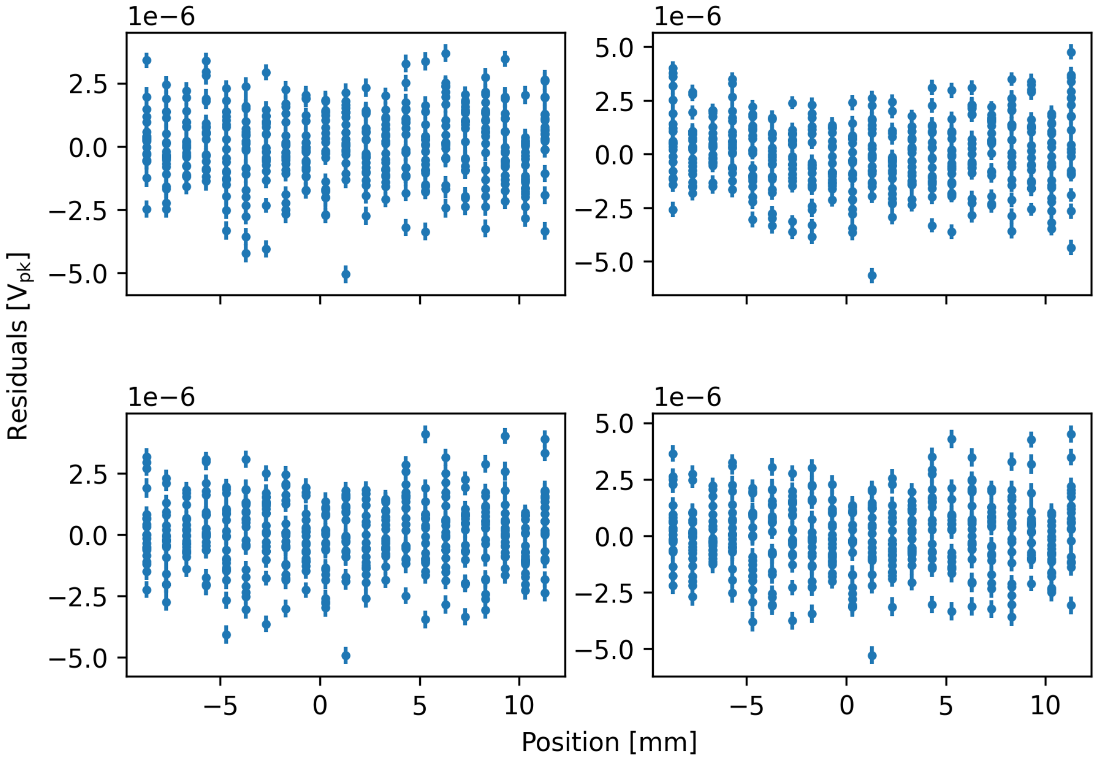

Figure 5.6: The residuals plot showing the difference between measurement and theory as displayed in figure 5.5. The upper two subplots represent quadrants 1 (left) and 2 (right), the lower two subplots for quadrants 3 (left) and 4 (right).

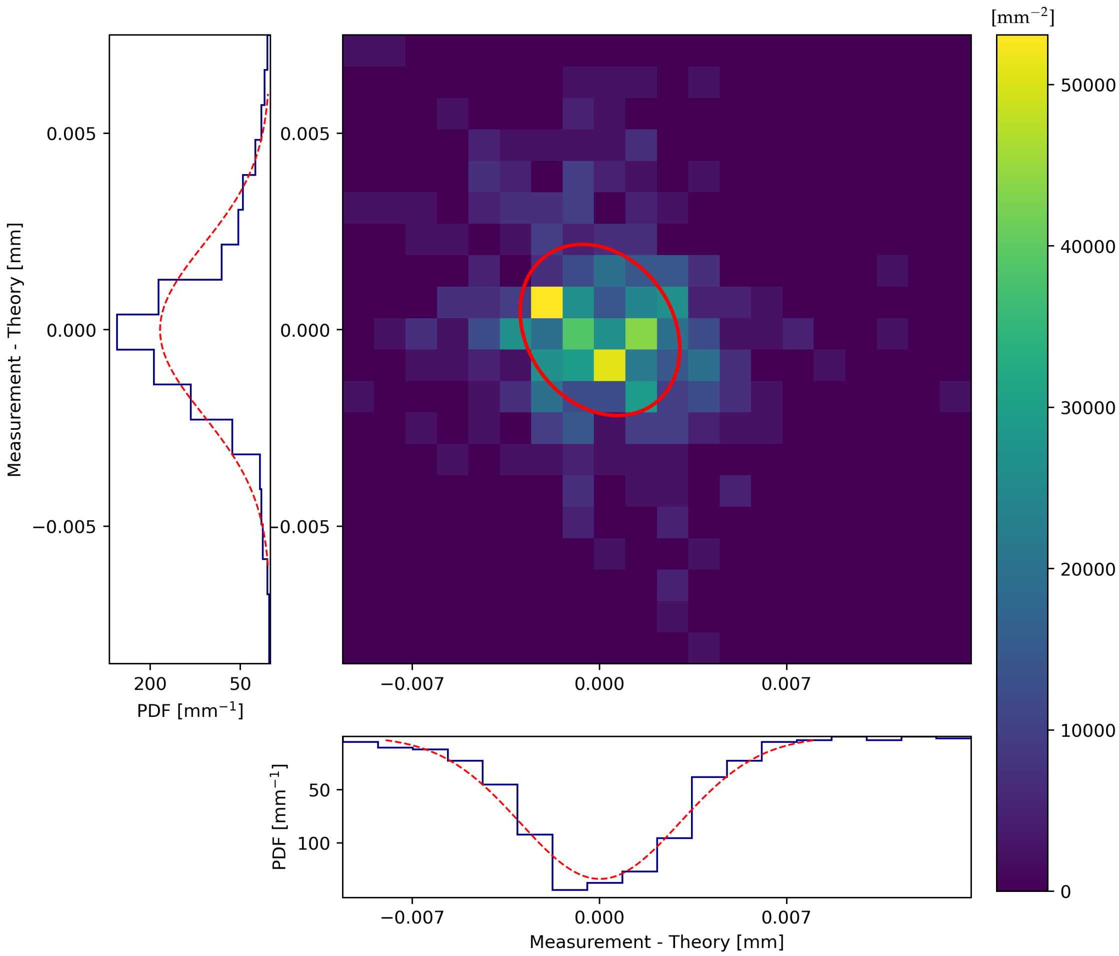

Figure 5.7: The differences between the measured positions and those calculated from the theoretical model. The two sub-plot histograms represent the probability density function of the horizontal differences (down) and the vertical differences (left). The central figure is a two-dimensional histogram for the differences in both transverse axes (vertical against horizontal). The covariance ellipse is drawn with one sigma radii on the same central figure (red curve). From the figure, a resolution of 142 nm and 103 nm is achievable for the horizontal and the vertical directions, respectively (for the total of 441 entries according to $\sigma / \sqrt{441}$).

5.3 Rogowski BPM with tuning capacitors

The first developed Rogowski BPM had a turn number and a self resonance frequency** for a single quadrant coil of 445 and 1.2 MHz, respectively. With these specifications, this BPM was sufficient for the operation in the single bunch mode with a beam momentum of 0.97 GeV/c which corresponds to a revolution frequency of 750 kHz. For the COSY beam in the four bunch mode, a new Rogowski BPM had to be developed where the operational bandwidth is at least a factor of three higher. One possibility to increase the frequency bandwidth (keeping the torus geometrical parameters unchanged) is by using a thicker wire for winding the coil which in turn results in a decreased number of windings. This can help decreasing the coil's overall inductance by a factor of the change introduced in the turn number and hence, can increase the system's natural frequency by the same factor††.
The winding wire diameter of the new coil was increased from 140 µm to 400 µm. The winding angular coverage range was around 60° which resulted in an overall single quadrant turn number of 132 (see Figure 5.8 panel (a)). Mechanical or human-related imperfections, mainly in winding the four quadrants or during the assembly process where electrical connections are made with the help of twisted wire extensions, can introduce a non ideal scenario for the resonance curves of the four quadrants where they do not resonate at the same frequency‡‡. To help improving this, an adjustable capacitor (see Figure 5.8 panel (b)) was connected in parallel with each quadrant coil (just before amplification). In an attempt to get the system of four quadrants resonating at the same frequency, the trimmers were adjusted by introducing a few pico Farad (each quadrant required a unique capacitance as they were all showing slightly different frequency curves in their default circuits). Figure 5.9 shows the frequency curves of the four quadrants of the Rogowski BPM before and after tuning the system to resonate at 3.229 MHz. The tuning was successful with a phase shift of less than 1° on resonance for all quadrants. Clearly, the distortions in both amplitude and phase responses were greatly minimized after the tuning process.
After tuning the four-quadrant system, the Rogowski BPM was calibrated by scanning the two dimensional map of $(\pm 10, \pm 10)$ mm in steps of 1 mm. A comparison between the measured positions and those reconstructed from theoretical expectations for two calibration measurements (performed at 750 kHz and 3 MHz) is illustrated in Figure 5.10. The distributions of these differences for horizontal and vertical beam coordinates are showing a resolution (for 441 data points) of < 100 nm for the lower frequency case and of several hundred nano meter for a calibration at 3 MHz. The discrepancy between the two cases can be attributed to the higher electromagnetic interference between individual quadrants as the frequency gets larger.

**Measured for the complete realistic single quadrant system, including the cables' as well as the pre-amplifier's effects.

††The inductance is proportional to the turn number squared, meanwhile, the self resonance goes inversely with the square root of the inductance [40–42].

‡‡The system's lumped elements are sensitive to, for example, an uneven introduced spacing between individual quadrant's windings or even a possible unequal length in the twisted wire extensions.

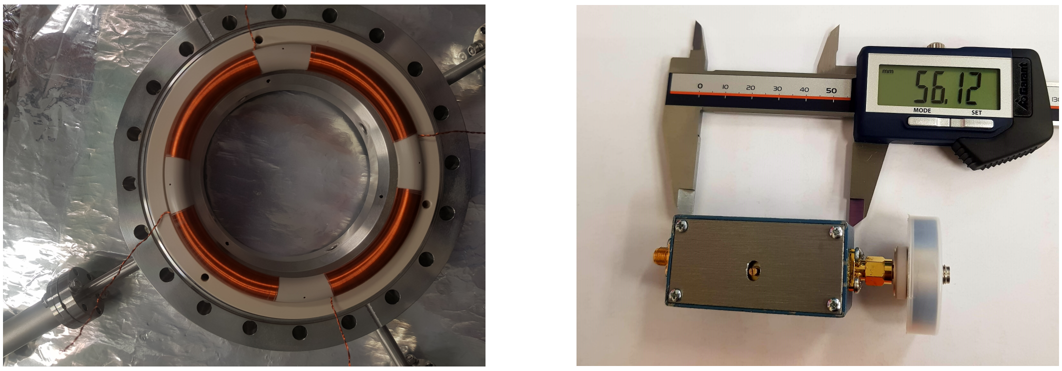

(a) **(b)**

Figure 5.8: Winding of a Rogowski BPM with higher operational bandwidth. Each quadrant coil has 132 turns and covers an angular range of around 60° (panel a). Adjustable capacitor (trimmer) used in parallel connection with each quadrant coil in order to tune the four-quadrant system at 3.229 MHz (panel b).

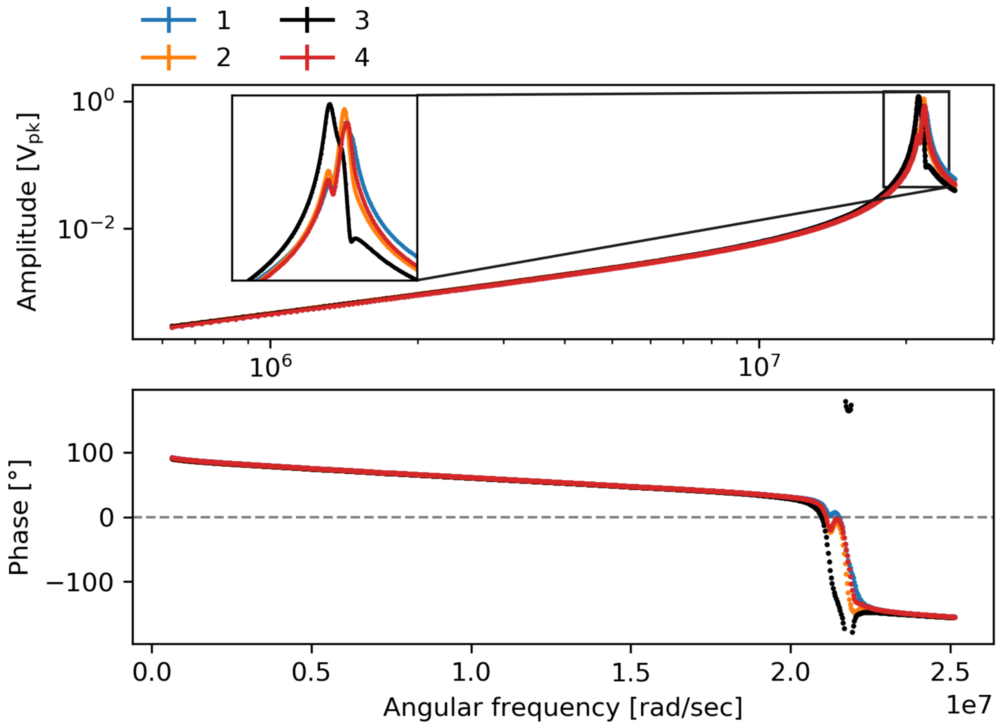

(a)

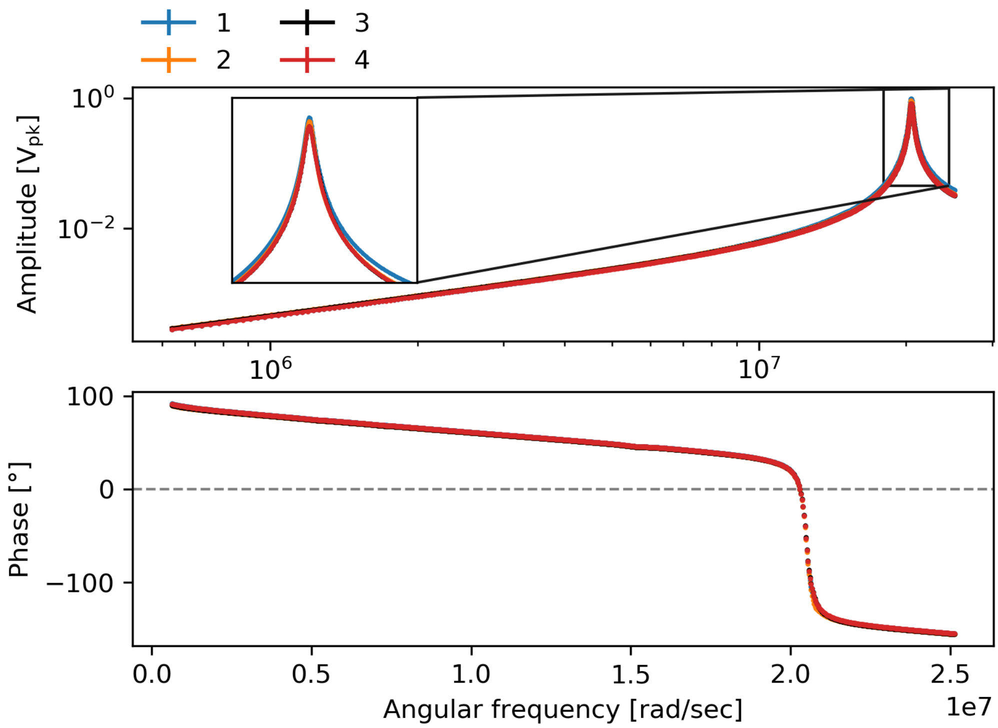

(b)

Figure 5.9: The measured frequency responses of the four quadrants before (panel a) and after (panel b) tuning. In each panel, the upper subplot shows the voltage amplitudes in logarithmic scale and the lower subplot shows the phase responses in linear scale. The numbers in the legend indicate the four quadrants.

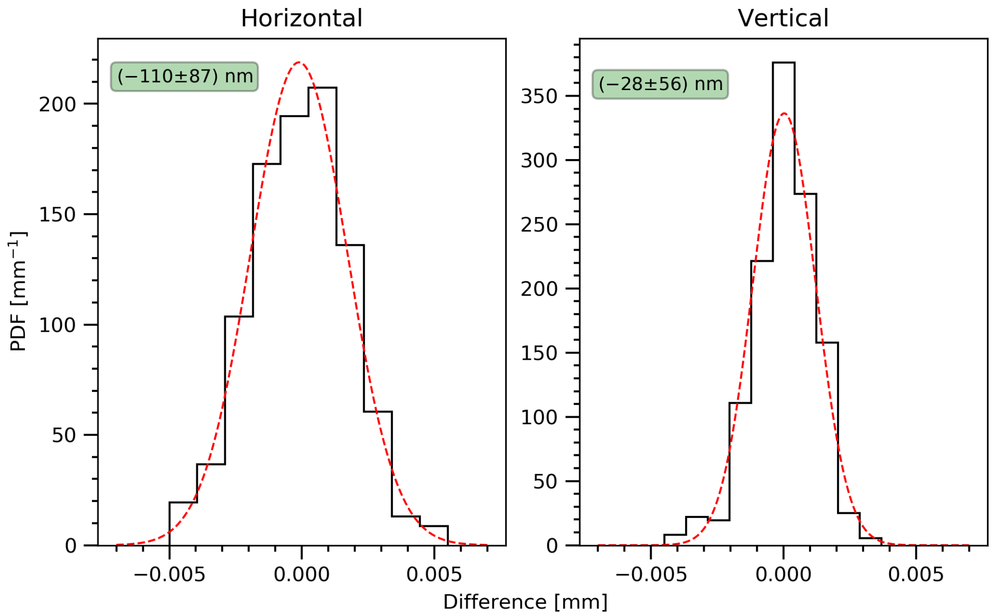

(a)

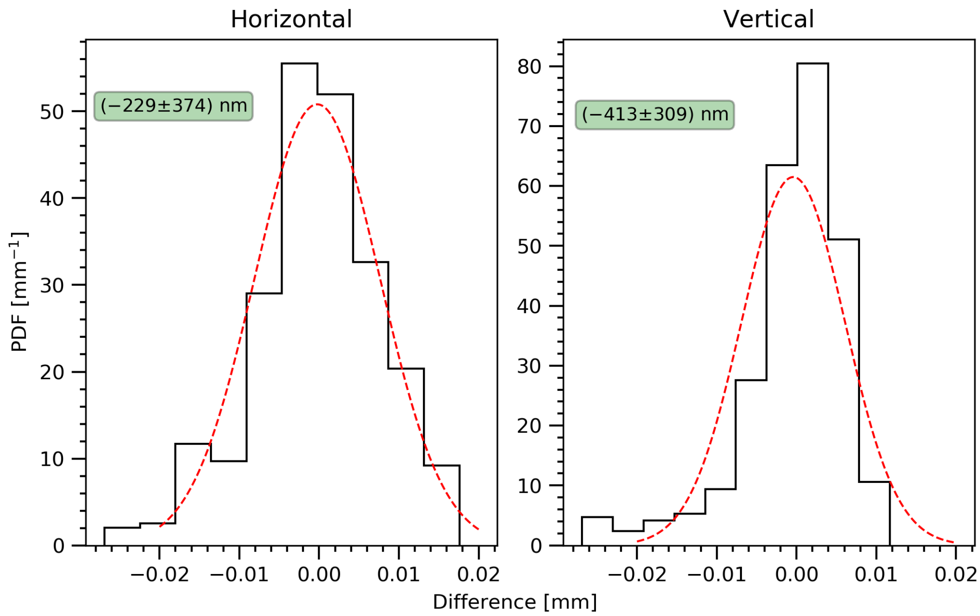

(b)

Figure 5.10: The distribution of difference between the measured and the reconstructed (using the theoretical model) positions at 750 kHz (panel a) and at 3 MHz (panel b). Gaussian fits for the calibration at 750 kHz show a resolution of 87 nm and 56 nm for the horizontal and the vertical beam coordinates, respectively. While for the calibration at 3 MHz a resolution of 374 nm and 309 nm for the horizontal and the vertical beam coordinates, respectively is shown. Each distribution in the figure has a total of 441 data entries and the resolution is according to $\sigma/\sqrt{441}$.

5.4 Evaluation of experiments

5.4.1 Stability of calibration measurement

The consistency in the voltage measurement is one of the important probes that can be used to check the device's stability over time. In fact, having a device with a good repeatability is one of the most important prerequisites for a reliable usage, in addition, it can be considered as a direct indicator to its accuracy. Figure 5.11 (left panel) shows how the voltage response from each quadrant coil changed when the same calibration measurement was repeated 30 times. The difference between all the corresponding voltage entries (of the total 441) that belong to the same scanned positions was calculated from one selected reference measurement (the first) and the remaining twenty-nine other repeated measurements. Each blue dot is showing the mean of the distribution of the differences (441 voltage deviations) between two repeated calibration maps while the error bar indicates its width (standard deviation). The arithmetic means were varying from a few hundred of nV up to seven µV, while the value of sigma was roughly similar ($5 - 6$ µV) for all the distributions of compared repetitions. The values of difference in responses are within the typical statistical jitter in voltage measurements. The level of change experienced by different quadrants was relatively similar. To estimate the error introduced by a possible drift in the voltage signal over time, the test repetition number 12 during which the maximum voltage change was observed (highlighted in red) was used to reconstruct the positions. Differences between reconstructed positions and true ones are shown on the right panel, where the left side is the distribution of the horizontal errors and the right side for the vertical ones. The maximum positional error introduced by temporal drifts was in the range of $15 - 20$ µm (denoted by σ_1 in subsection 5.4.6) for one single position measurement when the beam was off-centered by about 1 cm .

5.4.2 Signal temporal changes

Observing the change of voltage signals from the the Rogowski BPM over time without necessarily performing a calibration measurement is also an important probe for temporal stability. This test was performed for fixed beam positions, a fixed beam current and frequency and in addition, attention was given not to introduce any human related interruptions during data polling. An AC source with a frequency of 750 kHz and an amplitude of 50 mV was used for exciting the central wire (which mimics a beam). For this investigation, the BPM with a turn number of 445 was used with the full circuitry as in a typical calibration (with pre-amplifiers, cables and lock-in amplifiers as readout electronics).

Figure 5.12 shows the temporal changes of the four electrical signals over 24 hours. Each data entry represents a Fast Fourier Transform (FFT) component for the signal at 750 kHz sampled over 3 seconds. All data entries were polled continuously over the entire 24 hours.

Histograms of temporal distributions (as shown in figure 5.12) are plotted in figure 5.13. The vertical axes represent the probability density function plotted against the signal

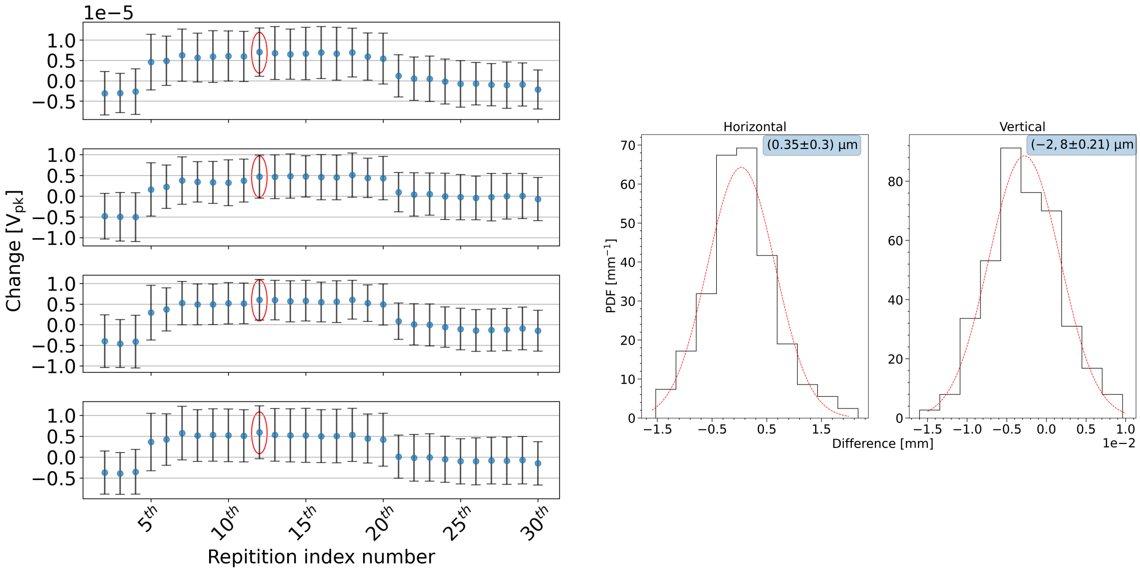

Figure 5.11: Assessment of stability of the voltage measurement from the four quadrants of the Rogowski BPM when the same calibration measurement is repeated thirty times. Left: the difference between all the corresponding voltage entries (of the total of 441) that belong to the same scanned positions was calculated from one selected reference measurement (the first) and the remaining twenty-nine other repeated measurements. Each blue dot is showing the mean of the distribution of the differences (441 voltage deviations) between two repeated calibration maps while the error bar indicates its width (standard deviation). The upper subplot represents quadrant 1 and so on until the lower subplot for quadrant 4. The arithmetic means were varying from a few hundred of nV up to seven µV, while the value of sigma was roughly similar ($5 - 6$ micro Volt) for all distributions of compared repetitions. The level of change experienced by the different quadrants was relatively similar. To estimate the error introduced by a possible drift in the voltage signal over time, the test repetition number 12 during which the maximum voltage drift was observed (highlighted in red) was used to reconstruct the positions, the difference between reconstructed positions and true positions is shown on the right panel, where the left side is the distribution of the horizontal errors and the right side of the vertical ones. The maximum positional error introduced by temporal drifts (σ_1, see section 5.4.6) was in the range of $(15 - 20)$ µm for one single position measurement when the beam is off-centered by about 1 cm.

amplitude. The projected data shows an overlap between more than one Gaussian. The level of variations in the electrical signal (taking the means from the different Gaussians) is of a few micro volts.

A similar test was repeated for a different coil with a turn number of 132 where tuning

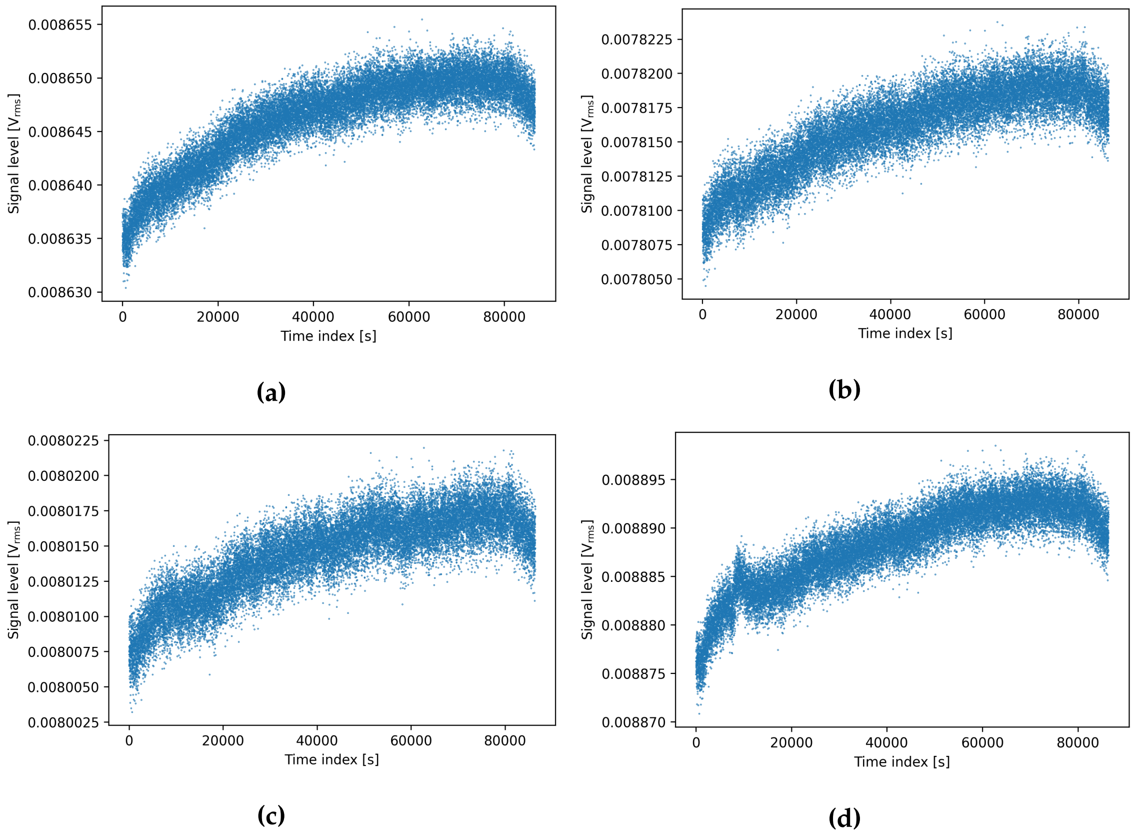

Figure 5.12: Temporal changes of the electrical signal from the Rogowski quadrant 1 (panel a), quadrant 2 (panel b), quadrant 3 (panel c) and quadrant 4 (panel d) polled over 24 hours. Each data entry represents an FFT component for the signal at 750 kHz sampled over 3 seconds. All the data entries were polled continuously over the entire 24 hours.

capacitors were used in the circuitry. The test lasted for 20 hours and the measurement conditions were kept the same as for the previous test. The results for temporal variations and their histograms in this test are addressed in the figures 5.14 and 5.15. Clearly, the multi Gaussian distribution is also there in the case of tuned quadrants. Similar to the previous test when the coils were not tuned, the level of variations in the electrical signal (taking the means from the different Gaussians) is of a few micro volts. During the data polling of this test, a data logger was set to start recording the temperature and the humidity variations over time. The purpose here was to check if there was any link between the temporal changes of the electrical signal and possible temperature and/or humidity changes in the laboratory. Figure 5.16 shows the temporal variations of the temperature (panel a) and the relative humidity (panel b) in the laboratory during the time of the data polling of this test (see figure 5.14). From figure 5.16, there is no direct

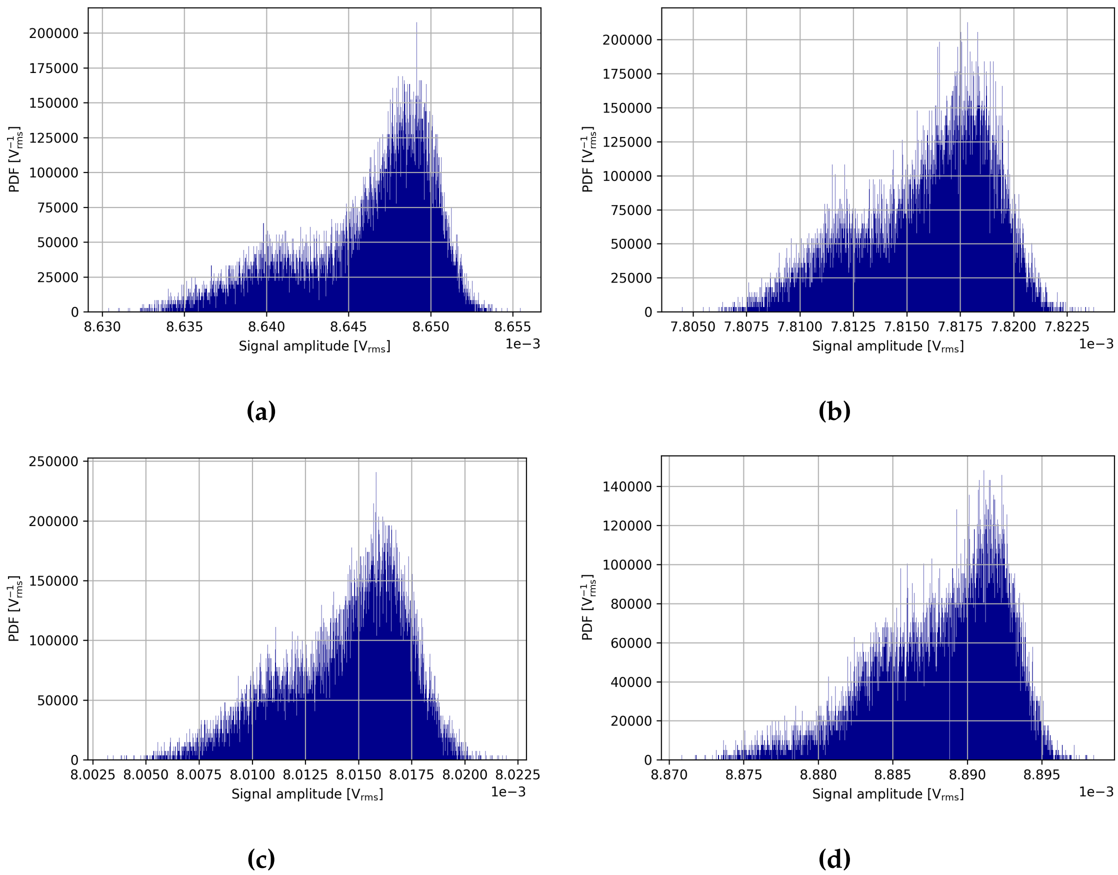

Figure 5.13: Histograms of the temporal distributions shown in figure 5.12. The vertical axes represent the probability density function plotted against the signal amplitude. The projected data shows an overlap of more than one Gaussian.

link between the temporal changes in the electrical signal and the change in temperature or relative humidity inside the test environment.

The results from the previous two tests for the signal temporal variations have shown similar behaviors for the multi-Gaussian distributions of the signals. However, the level of variations (taking the means) is in the range of a few micro volts (which is within the noise permissible jitter level of an amplified signal). It is also clear that the shape of these overlapping Gaussians are similar for all separate quadrants (or in other words, the time content of the temporal change is similar) which should reduce errors that can happen as a result of such a change since the calibration of the device is usually based on the voltage ratios (the difference over the sum, where a change by a common factor can simply drop out).

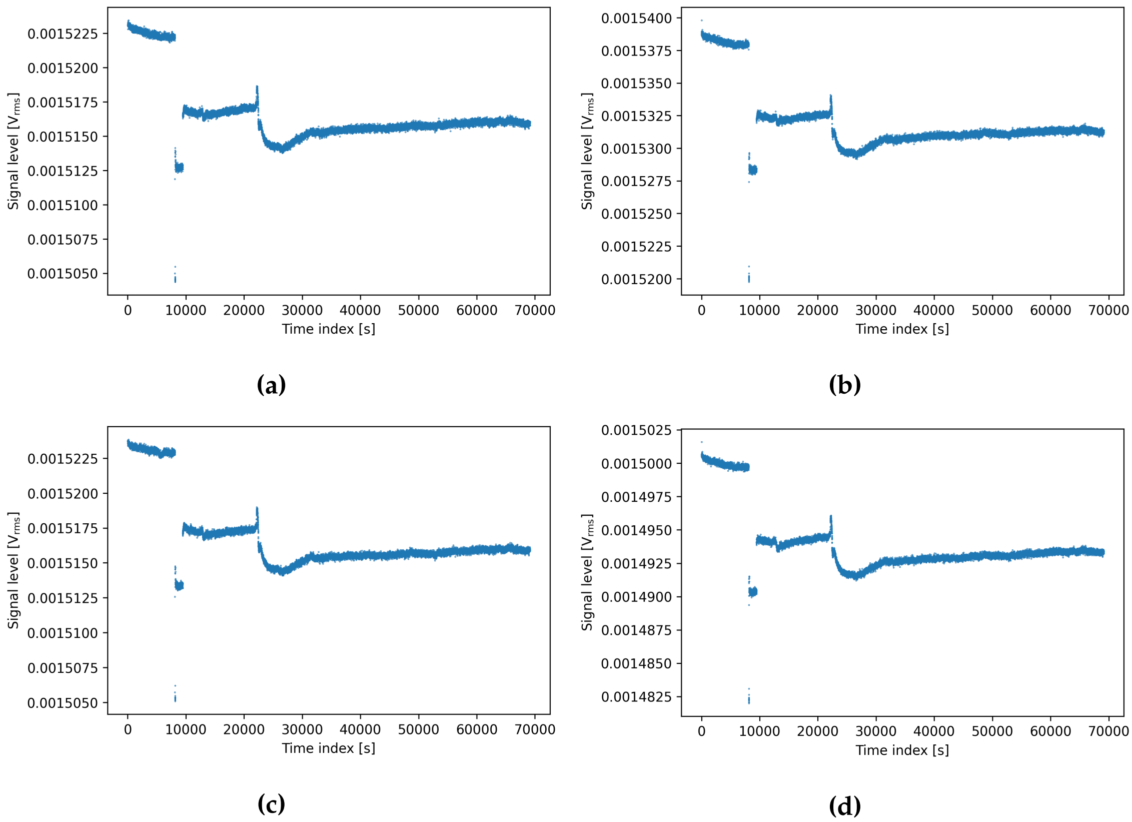

Figure 5.14: Temporal changes of the electrical signal from the Rogowski BPM's quadrant 1 (panel a), quadrant 2 (panel b), quadrant 3 (panel c) and quadrant 4 (panel d) polled over 20 hours. The four tuning capacitors were used during the measurement time. Each data entry represents an FFT component of the signal at 750 kHz sampled over 3 seconds. All data entries were polled continuously over the entire 20 hours.

5.4.3 Stability of resonance

This subsection introduces the stability of resonance curves from the four quadrant coils of the Rogowski BPM after using the tuning capacitors (see section 5.3). The response (voltage and phase) was measured as a function of the frequency using the lock-in amplifier on one day and then was repeated a day later to check the stability over time. During the measurement times, attention was given to keep the test conditions the same. Figure 5.17 shows the stability of the resonance for quadrants 1 (left panels) and 2 (right panels) of the Rogowski BPM with tuning capacitors. The upper and lower panels represent the voltage ratio (the ratio between the ith voltage from day 1 and the corresponding jth voltage entry from day 2) and the phase difference for the same data entries when repeated after one day, respectively. Similarly, figure 5.18 shows the results for quadrants 3 and 4.

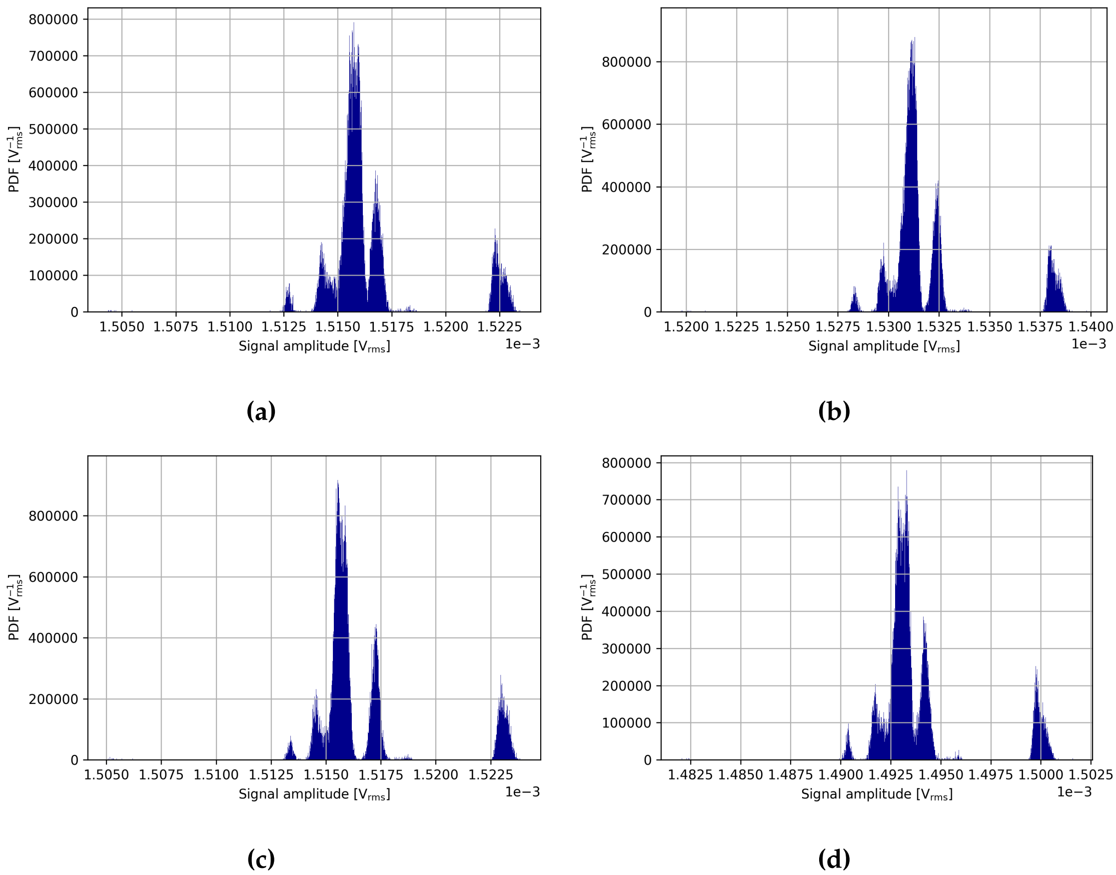

Figure 5.15: Histograms of the temporal distributions shown in figure 5.14. The vertical axes represent the probability density function plotted against the signal amplitude. The projected data shows an overlap of more than one Gaussian.

Clearly, the greatest change in signal after one day happens as expected around the SRF where the voltage changes by a few per mill (except for quadrant 3 where the change reaches about 1 percent). The maximum difference in the phase shift (also happens at the SRF) for all the quadrants is less than one degree. In the lower frequency range, the change in the voltage signal or even in the phase shift for all the quadrants is very small and there the system shows the maximum stability, this makes an agreement with the fact that these quadrants are there in the inductive region (away from the SRF) where parasitics are minimal.

5.4.4 Calibration vs. source wave form

This subsection investigates the effect of the wave form of the excitation source on the BPM calibration, typically a sinusoidal source is used for testing purposes in the

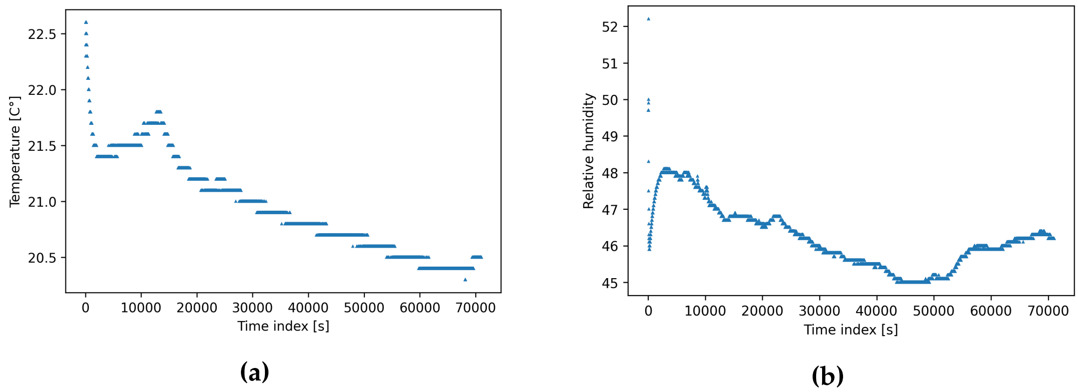

Figure 5.16: Temporal variations of temperature (panel a) and relative humidity (panel b) in the laboratory during the time of data polling for the test in figure 5.14.

laboratory. However, a realistic wave form of a beam in COSY in the single bunch mode has a pulse wave form (see figure 5.19). To test if the wave form can introduce effects on the calibration, two calibration measurements were performed with two different sources; a sinusoidal with a frequency of 750 kHz and a pulse wave form with rise and fall times of 42 ns, and a width of 210 ns. The amplitude for both wave forms was kept the same. Figure 5.20 shows the histograms of the difference between calibrating the Rogowski BPM at these two different wave forms. The effect on the calibration is represented as the differences in $\frac{\Delta_x}{\Sigma}$ (blue) and $\frac{\Delta_y}{\Sigma}$ (orange) for the two cases. From the histograms, it can be seen that the effect shows a non perfectly normal distribution (especially for the vertical ratio). The peak difference (with maximum number of counts) corresponds to an error in the position of about 30 µm considering the linear approximation in the position dependence.

5.4.5 Signal to Noise Ratio (SNR)

The SNR represents the ratio between the wanted signal and the unwanted noise level. The signal from one single quadrant coil in the Rogowski BPM is described in eq. 5.2. An unavoidable noise signal can be described by a combination of thermal noise, electronic noise from the measuring devices, ground loops and any pickups caused by electromagnetic interference. In fact, the unintentional pickups between the individual quadrants is one significant source of noise, as it happens at the same reference frequency. The thermal noise through a resistor R at a temperature T can be given by $\sqrt{4K_B T R \Delta f}$ where K_B is the Boltzmann constant and Δf is the measurement bandwidth. The SNR then becomes (e.g. for coil number 1):

$$\mathrm{SNR} = \frac{U'_{\mathrm{out1}}(x', y', \omega)}{\sqrt{4K_B T R \Delta f + \mathrm{other}}}, \tag{5.5}$$

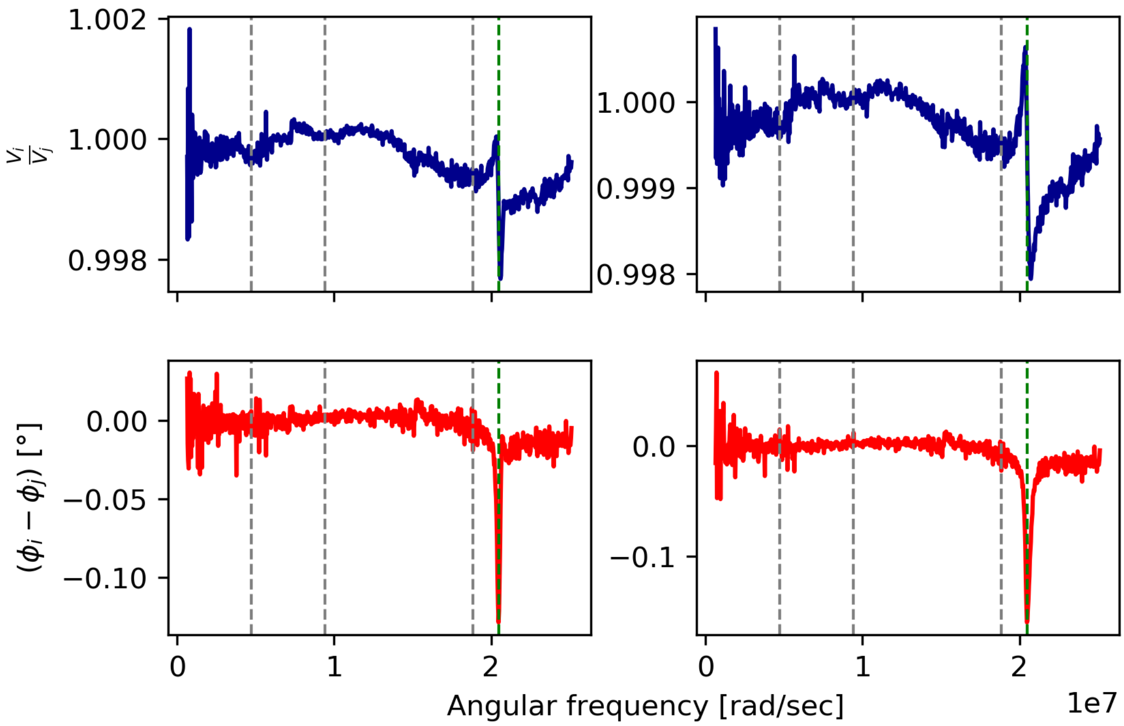

Figure 5.17: Stability of the resonance for quadrants 1 (left panels) and 2 (right panels) of the Rogowski BPM with tuning capacitors. The upper and the lower panels represent the voltage ratio and the phase difference for the same data entries when repeated after one day, respectively. The gray dashed vertical lines indicate the locations of the operational frequencies 750 kHz, 1.5 MHz and 3 MHz. The green dashed vertical line indicates the location of the resonance frequency.

where "other" indicates the remaining noise contributions[§§] from other sources as mentioned earlier. For a bandwidth of 6.81 Hz which means an equivalent noise bandwidth (ENBW) of 7.69 Hz, the thermal noise (assuming a single quadrant's resistance of 19.5 Ω) is about 1.58 nV at room temperature, which is then raised to 28.37 nV if the pre-amplifiers were used. The pre-amplifiers have an input noise level around 3 nV [75]. The lock-in amplifier can introduce

which varies from a few nano Volts up to around one micro Volt depending on the used settings, as the input voltage level, the input impedance and the 3 dB bandwidth used for the low pass filter. Usually, an amplified induced signal as measured by the lock-in device at 750 kHz jitters on the level of few micro Volt. However, this jitter level depends strongly on the frequency characteristics of the inductor coil itself, i.e. if the frequency was much lower than its SRF (or in other words, if it had a bigger operational bandwidth)

[§§]Mathematically, as a sum of quadratures of other possible noise contributions.

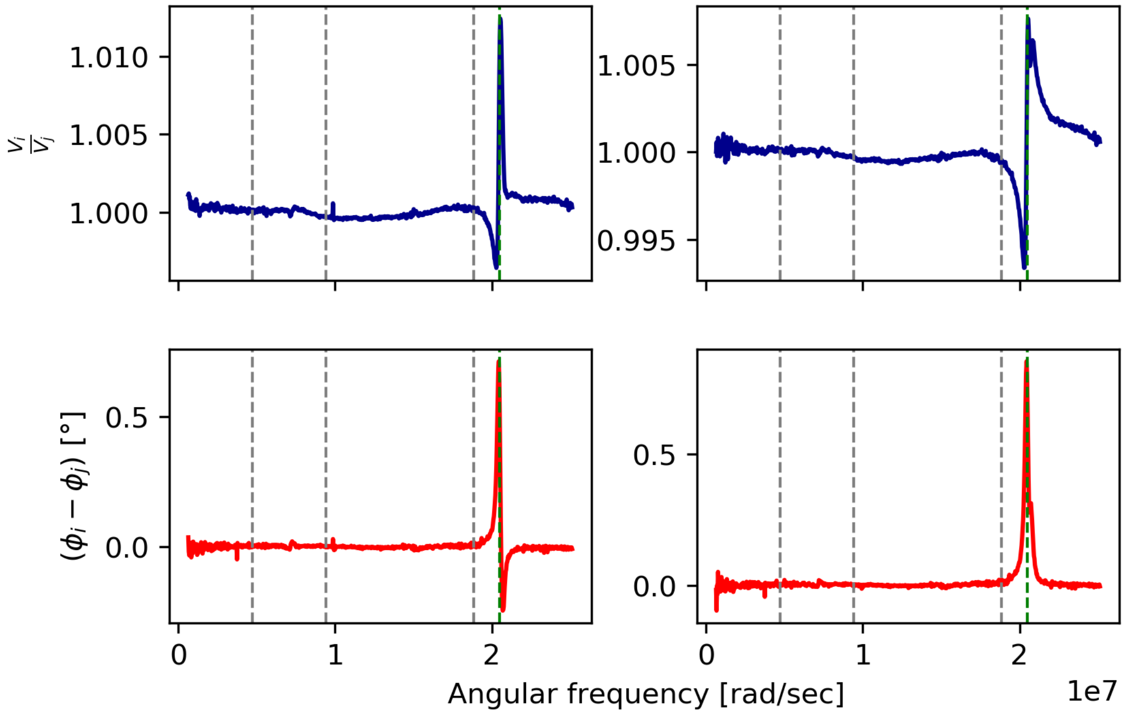

Figure 5.18: Stability of the resonance for quadrants 3 (left panels) and 4 (right panels) of the Rogowski BPM with tuning capacitors. The upper and the lower panels represent the voltage ratio and phase difference for same data entries when repeated after one day, respectively. The gray dashed vertical lines indicate the locations of the operational frequencies 750 kHz, 1.5 MHz and 3 MHz. The green dashed vertical line indicates the location of the resonance frequency.

then the noise contribution caused by the electromagnetic interference between separate quadrants will be much smaller. In general, the SNR can be in the level of a few thousands (for a signal level around a few mV, 1 MΩ input impedance, 7.69 Hz ENBW, for a coil with 445 turns per quadrant and a beam current with an amplitude and a frequency of 0.24 mA and 750 kHz, respectively). However, it can be also worse or even much better depending on the factors affecting both the signal and the noise levels as stated earlier. As an example of the SNR distribution, figure 5.21 shows the histograms of the SNR for the four quadrant coils of the Rogowski BPM during the measurement time of the test shown in figure 5.15. Despite the multi-Gaussian distributions observed in the four signals' amplitudes, the SNR is still normally distributed with an average around 2×10^3.

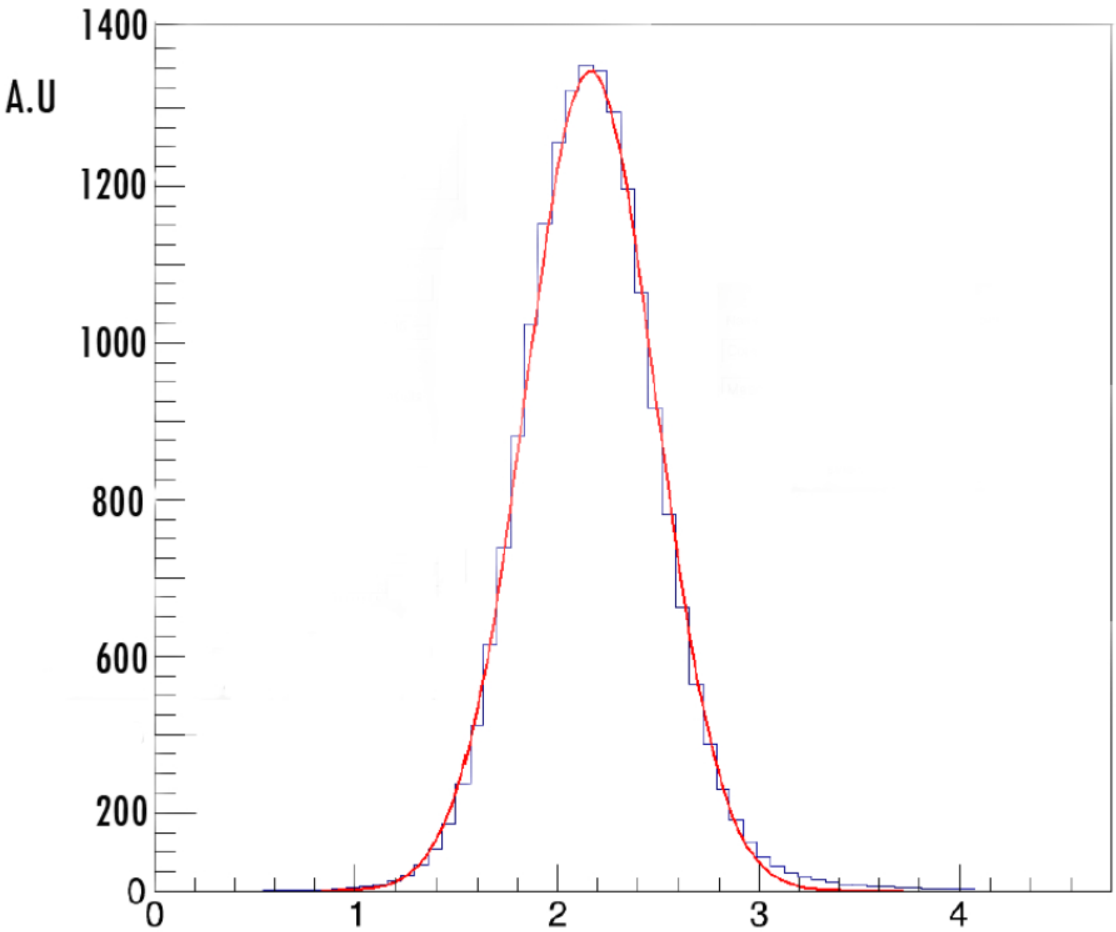

Figure 5.19: The bunch profile for COSY beam in the single bunch mode. The Gaussian fit (red) has a width (3σ) of 0.96 radian.

5.4.6 Accuracy

The accuracy is the ability to define the beam position relative to some absolutely known or defined axis, e.g. the mechanical axis of the BPM device, the axis of a quadruple magnet or the central axis of the beam pipe in an accelerator. Usually, the accuracy is affected by mechanical alignment errors, interference caused by electromagnetic pickups, reflections or attenuation through measurement cables, calibration errors and in addition to short term and long term drifts [76–78].
With careful handling during the device installation along with the procedure mentioned in chapter 4 where the laser tracker is used to measure reference fiducials on the top of the device, mechanical errors can be reduced. Errors caused by interference, pickups, impedance change or reflections can be minimized if the device circuitry was exactly the same during calibration and later after installation. An example of errors introduced

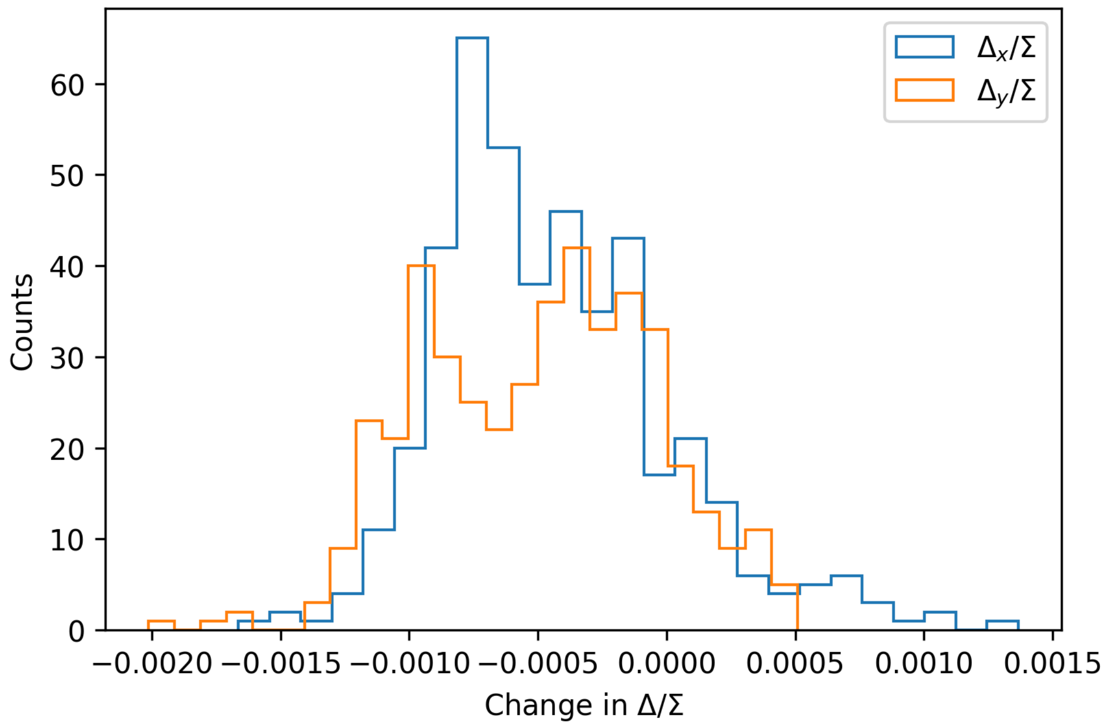

Figure 5.20: Histograms of the difference between calibrating the Rogowski BPM at two different wave forms; a sinusoidal with a frequency of 750 kHz and a pulse wave form with rise and fall times of 42 ns and a width of 210 ns. The effect on the calibration is represented as the differences in $\frac{\Delta_x}{\Sigma}$ (blue) and $\frac{\Delta_y}{\Sigma}$ (orange) for both cases. From the histograms, it can be seen that the effect shows a non perfectly normal distribution (especially for the vertical ratio). The peak difference (with maximum number of counts) corresponds to an error in the position of about 30 µm considering the linear approximation in the position dependence.

by the calibration of the device can be given through the repeatability test, where the change in the voltage signal from each separate quadrant coil once the measurement is repeated is used to reconstruct the positions (σ_1, see Figure 5.11). The value of this positional error also represents an estimate for the level of errors introduced by means of short temporal drifts. Another possible source of calibration errors can be coming from the mismatch between the image current distributions on the beam pipe in the laboratory and in the accelerator environment.
Considering the accuracy of stepping drives used in the calibration procedures, an estimate for the accuracy of the Rogowski BPM can be given through:

$$\sigma \approx \sqrt{{\sigma_1}^2 + {\sigma_2}^2}\,, \tag{5.6}$$

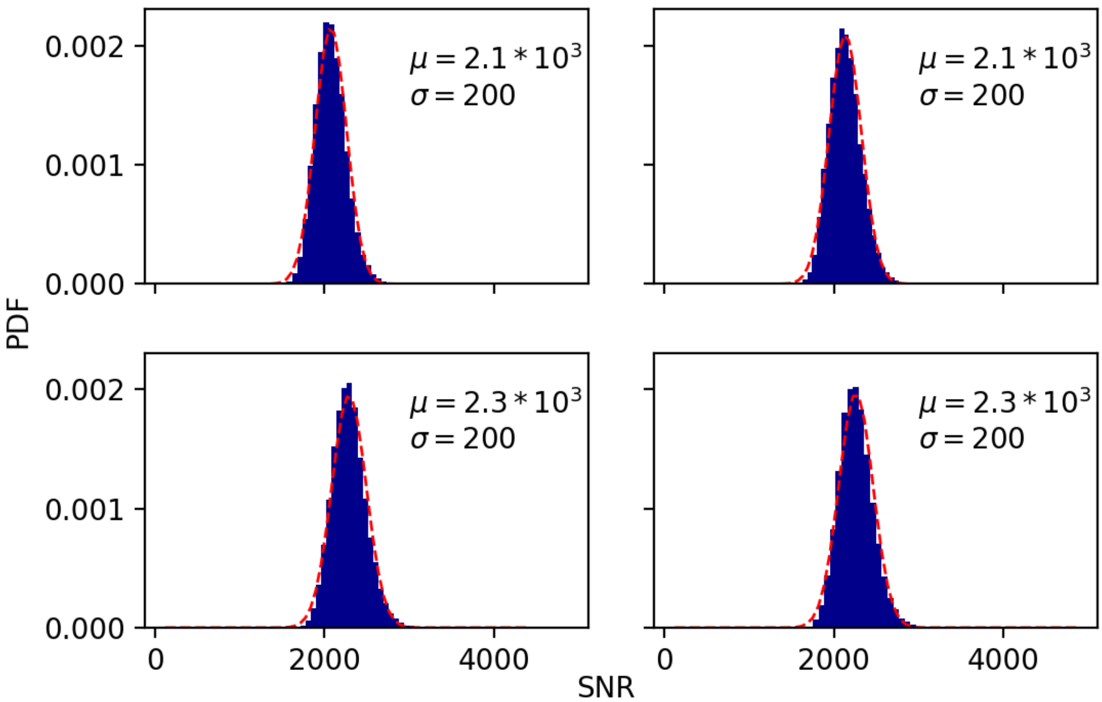

Figure 5.21: Histograms of the SNR from the measurement in figure 5.15 for the Rogowski BPM's four quadrants. Despite the multi-Gaussian distributions observed in the four signals' amplitudes, the SNR is still normally distributed with an average of around 2×10^3.

where σ_1 is the error caused by short term drifts and σ_2 is the error caused by stepping drives (see section 4.2). This means for one single position measurement, the positional accuracy is:

$$\sigma_{x,y} \approx 21\ \mu\text{m}\,. \tag{5.7}$$

Of course, this is assuming that other error sources are well controlled, i.e. in a realistic case, other errors are just as probable, and if they were present then they must be considered in the quadratic error sum in eq. 5.6

5.4.7 Resolution

The spacial resolution is the minimum position change that can statistically be resolved. It is affected by the noise level (and hence by the signal to noise ratio) as well as short term or long term drifts [79, 80]. The resolution is also dependent on the averaging time which makes it much better than the accuracy in most of the cases. In many cases resolution is more important than the accuracy itself, e.g. for clockwise counter-clockwise

beams, knowing the relative change between the two beams is more important than knowing the absolute positions of either beams.
To estimate the spacial resolution while neglecting the differences between individual coils (for simplicity) and assuming that the beam position is somewhere around the center where the linear position dependence is just sufficient, the $\frac{\Delta}{\Sigma}$ (see Appendix C) becomes:

$$\frac{\Delta_x}{\Sigma} = c_1 x\,, \tag{5.8}$$

$$\frac{\Delta_y}{\Sigma} = c_1 y\,. \tag{5.9}$$

The positional error then becomes:

$$\delta_x = \frac{\delta_{\frac{\Delta_x}{\Sigma}}}{c_1}\,, \tag{5.10}$$

$$\delta_y = \frac{\delta_{\frac{\Delta_y}{\Sigma}}}{c_1}\,. \tag{5.11}$$

By substituting the values of $\delta_{\frac{\Delta_x}{\Sigma}}$ and $\delta_{\frac{\Delta_y}{\Sigma}}$ from appendix C, the positional resolution as determined by the noise limit becomes:

$$\begin{aligned} \delta_x = \delta_y &= \frac{\delta_{U_i}}{2c_1 U_i}\,, \\ &= \frac{1}{2c_1 \times \mathrm{SNR}}\,, \end{aligned} \tag{5.12}$$

where the index i represents any of the four quadrants. Clearly, from the above equation, the spacial resolution goes inversely with the signal to noise ratio. As stated before, the SNR can vary depending on the settings of the measuring device, the beam current and the operational frequency but in general it can be in the range of some few thousands.
For a value of sensitivity parameter c_1 of 0.0175 mm^{-1} and assuming an SNR value of a few thousands, the resultant positional resolution is a few µm for one single measured beam position. This estimate assuming a beam current of 0.24 mA which corresponds to a beam intensity (particles per bunch) of 2×10^9, meaning that a beam intensity with few factors higher can easily bring positional resolution down to the sub µm regime for one single position readout and an averaging time of one second.

Chapter 6

Installation and tests in the accelerator facility COSY

6.1 Installation

Two prototype Rogowski BPMs were installed in the COSY ring. The installation was made at the entrance and the exit of the RF **W**ien **F**ilter (WF)* in order to measure the coordinates of the beam entering and leaving the WF, where a vanishing net Lorentz force is expected for a beam passing along the WF central axis. Figure 6.1 shows the integrated Rogowski BPMs in the COSY ring where each BPM is installed between a quadruple magnet and a one side of the WF device.
These two Rogowski BPMs were in fact not identical. The first difference was in the winding number for the separate quadrants of each BPM where the first (BPM51) and the second (BPM52) were made with 445 and 132 turns per quadrant, respectively. The second difference was the diameter of the copper wire used in winding the coils which was 140 µm for the BPM51 and 400 µm for the BPM52. These two differences mean that also the two devices are having different operational bandwidths. In addition, the BPM52 was connected with tuning capacitors while the BPM51 was not.

*For more information on the RF WF see the reference [22].

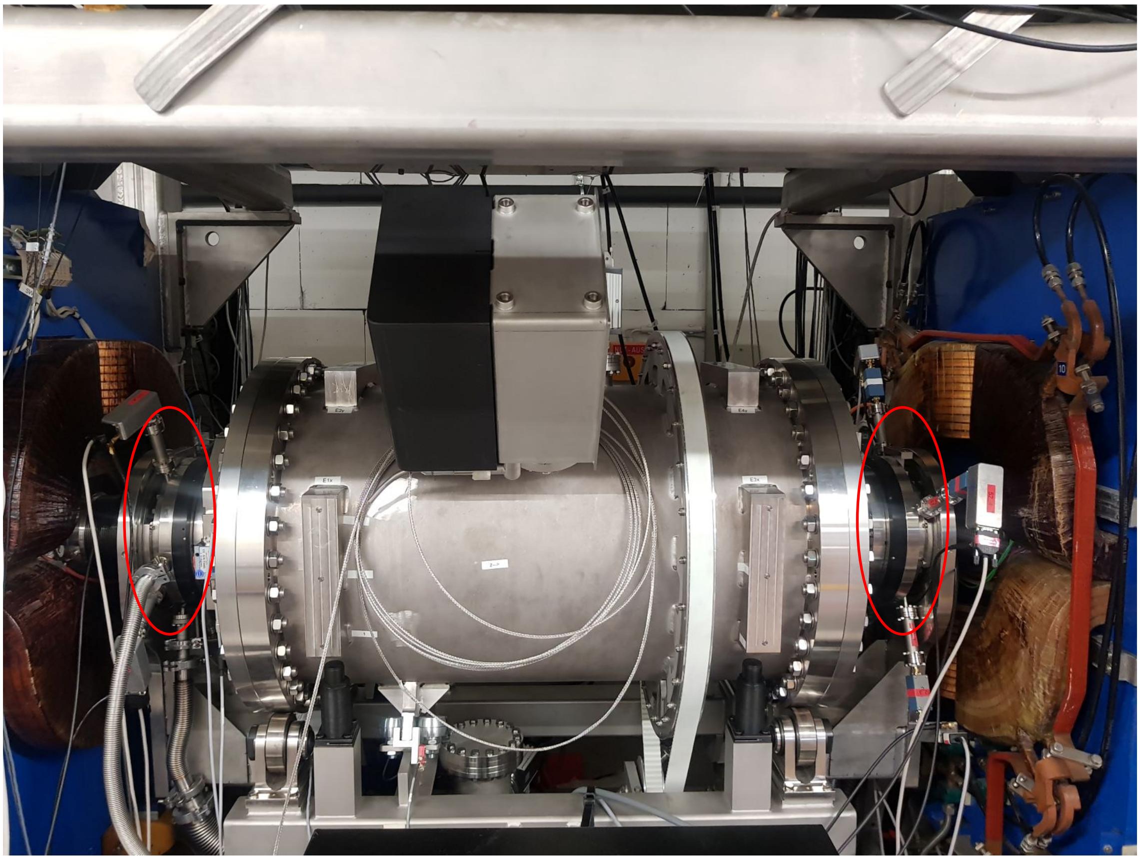

Figure 6.1: Picture of the Rogowski BPMs installed in the COSY ring. The red ovals indicate the Rogowski BPMs, each is integrated between a quadruple magnet from one side and the RF WF device from the other side. The BPM51 is to the left of the picture and the BPM52 is to the right.

6.2 Electrical offset

Before setting up the system for delivering position readouts, it is important to check the existence of any potential voltage offset (which can introduce positional errors). This voltage offset is defined as the measured response from each quadrant coil in the absence of an excitation beam current. Figure 6.2 shows the effect of an existing voltage offset on the $\frac{\Delta}{\Sigma}$ (blue for horizontal and green for vertical). The upper two panels and the lower two panels (plotted against the COSY beam current) are representing the ratios before and after voltage offsets correction, respectively. Clearly, following offsets' suppression (around the level of 700 µV for each quadrant), the ratios became current independent and the maximum deviation between measured ratios changed by one order of magnitude, while the difference between data points was within the statistical error's level (around 2×10^{-4}).

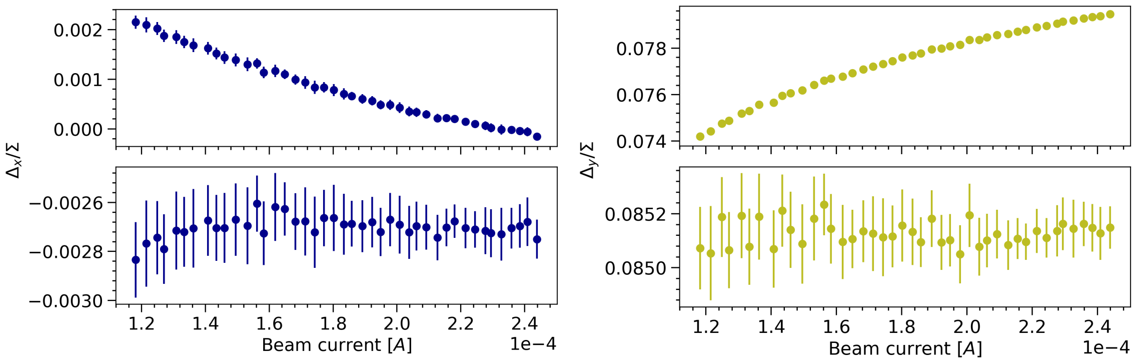

Figure 6.2: The $\frac{\Delta}{\Sigma}$ (blue for horizontal and green for vertical) before (upper two panels) and after (lower two panels) voltage offset correction, plotted against the COSY beam current. Clearly, following offsets' suppression, the ratios became current independent and the maximum deviation changed by one order of magnitude, while the difference between data points was within the statistical error's level (around 2×10^{-4}).

6.3 Local orbit bump

Another import measurement that is needed before setting the system for position measurements, is the local orbit bump test. By this test, the orbit is being manipulated by applying a nearby positional change which is introduced by a kick from corrector magnets. Theoretically, the orbit response upon this change should be linear with the applied corrector current (bump setting) [81]. Figure 6.3 shows the results of the vertical positions† measured by the BPM51 (upper plot) after applying a parallel vertical local bump around the WF. Similarly, the lower plot shows the vertical orbit measured by the BPM52 during the same time of the local bump. The statistical resolution of the BPM51 was in the range of $1 - 3$ µm while it was ranging from few hundreds of nm up to 1 µm for the BPM52. During this test, the bumps' settings were varied in the range of ± 5 mm, and the COSY was running in the single bunch mode (triggering at 750 kHz). A linear response is achieved as can be seen from figure 6.3. In addition, the difference between the measured positions by the two BPMs is about 200 µm at the maximum (which is expected to be small since the bump was parallel).

Another test of parallel local orbit bumps was performed around the WF in both vertical and horizontal planes when the COSY was running in the four bunches mode (triggering at 3 MHz). During this test, the bumps were applied in steps of 200 µm in the range of $\pm$ 2 mm. Figure 6.4 shows the horizontal positions measured by the BPM51 (upper plot) and the BPM52 (lower plot) after applying the horizontal bumps. Similarly, results for

†All measured positions in this chapter are based on a sampling time of 1 s (unless stated differently).

the vertical positions after the vertical bumps are shown in figure 6.5.
From figures 6.4 and 6.5, one can see that despite the fluctuations in position readouts over the single cycles, the linearity in orbit responses is still preserved to some extent. The deviation between the two BPMs was sometimes as large as 400 μm. The measured response was sometimes away from the expected line, this can be attributed to a potential failure in some of the steerers (especially if observed in both BPMs). It's worthwhile to mention that at the frequency of 3 MHz, the BPM52 is getting close to its SRF while the BPM51 is already behind its SRF. This may justify the higher fluctuations in measured orbits during single cycles, also it may justify the fact that the response of BPM51 was less linear with respect to different bumps' settings which caused larger differences in measured responses by the two BPMs compared with the case when the COSY was running in the single bunch mode.

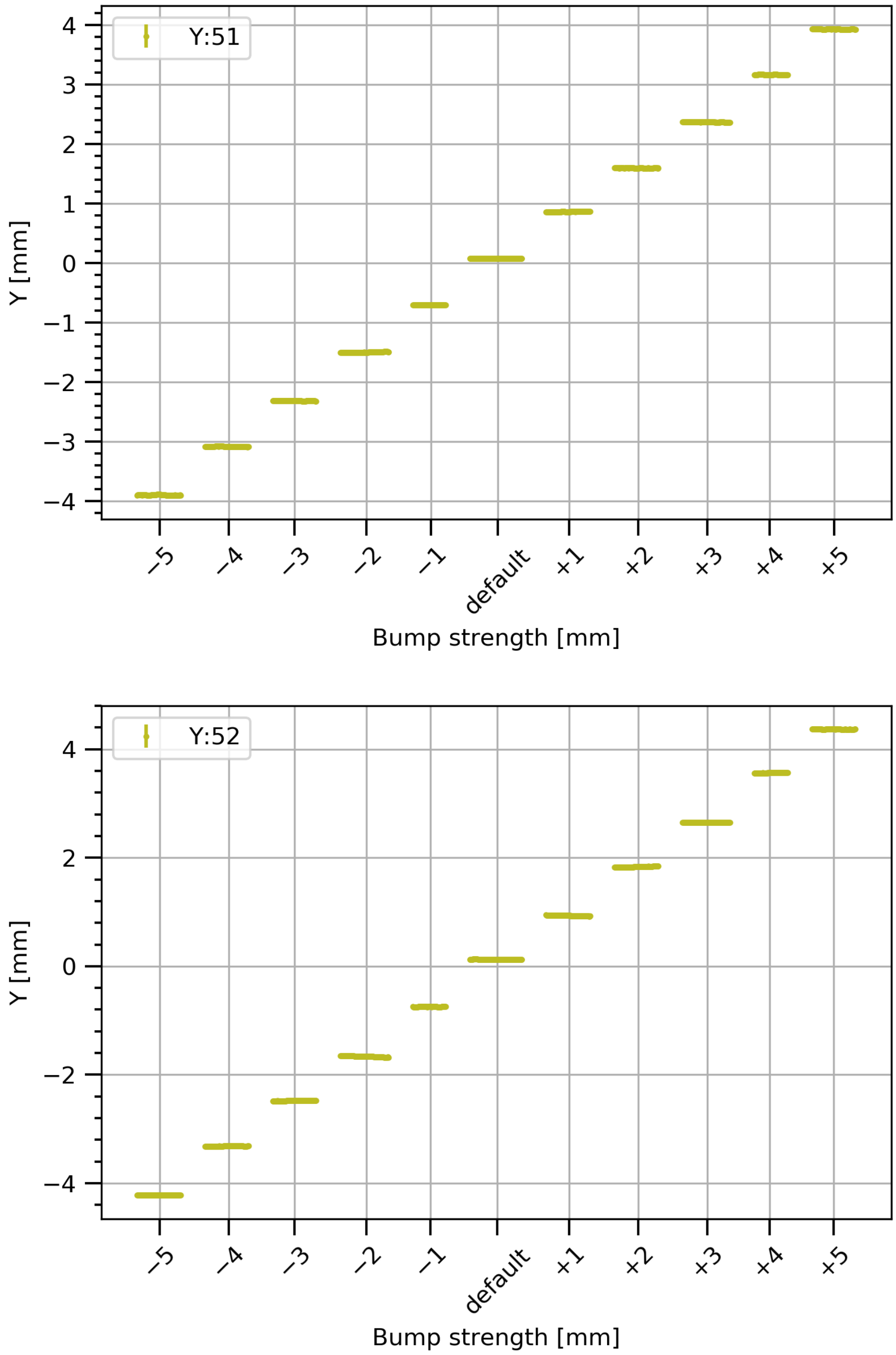

Figure 6.3: The vertical orbit measured by the BPM51 (upper plot) after applying parallel vertical local bumps around the RF WF. Similarly, the lower plot shows the vertical positions measured by the BPM52 during the same time of applying the local vertical bumps. During this test, the bumps' settings were varied in the range of ±5 mm, and the COSY was running in the single bunch mode.

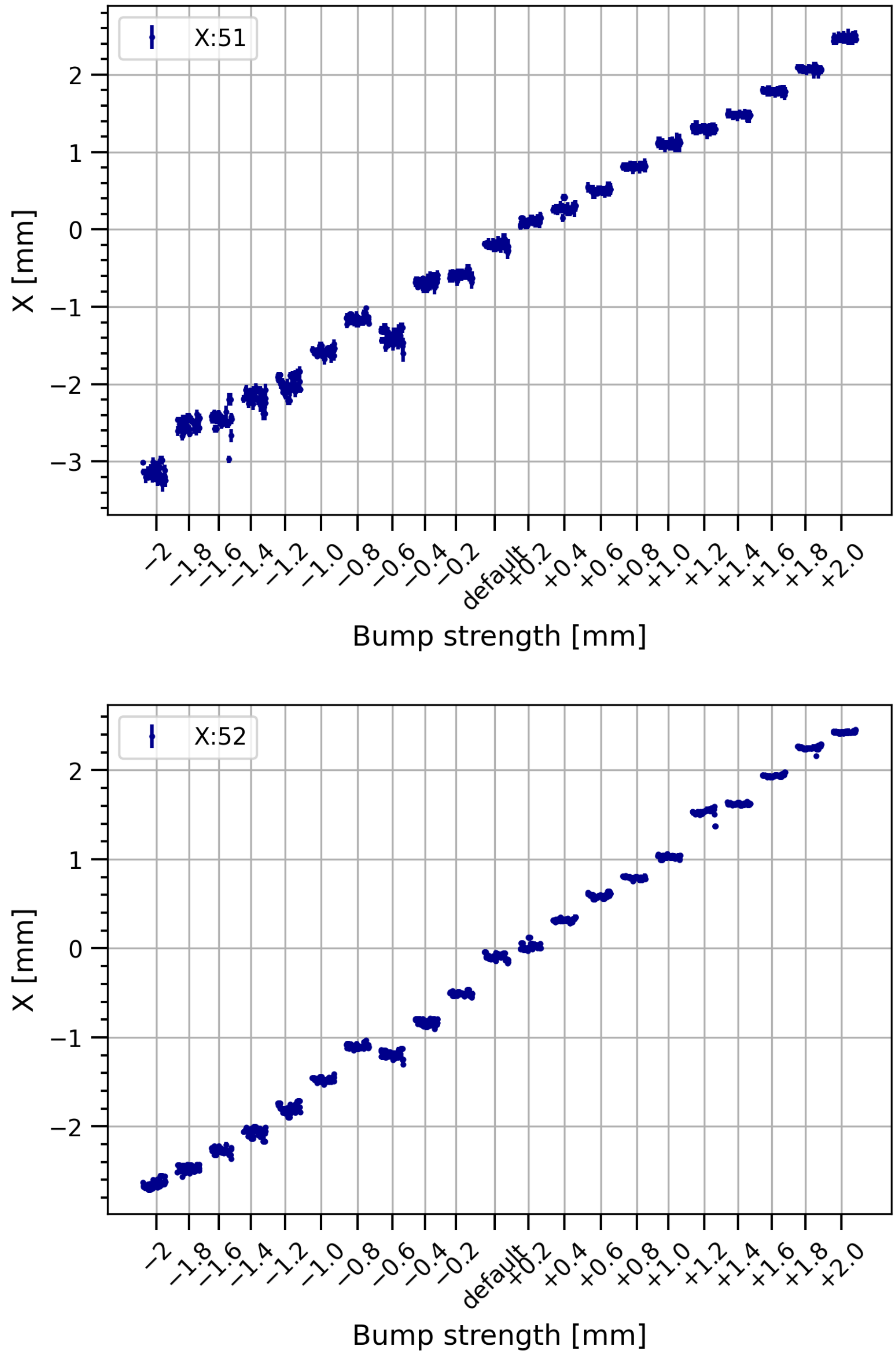

Figure 6.4: The horizontal positions measured by the BPM51 (upper plot) after applying parallel horizontal local bumps around the RF WF. Similarly, the lower plot shows the horizontal positions measured by the BPM52 during the same time of applying the local horizontal bumps. During this test, the bumps' settings were varied in the range of ± 2 mm with steps of 200 μm, and the COSY was running in the four bunches mode.

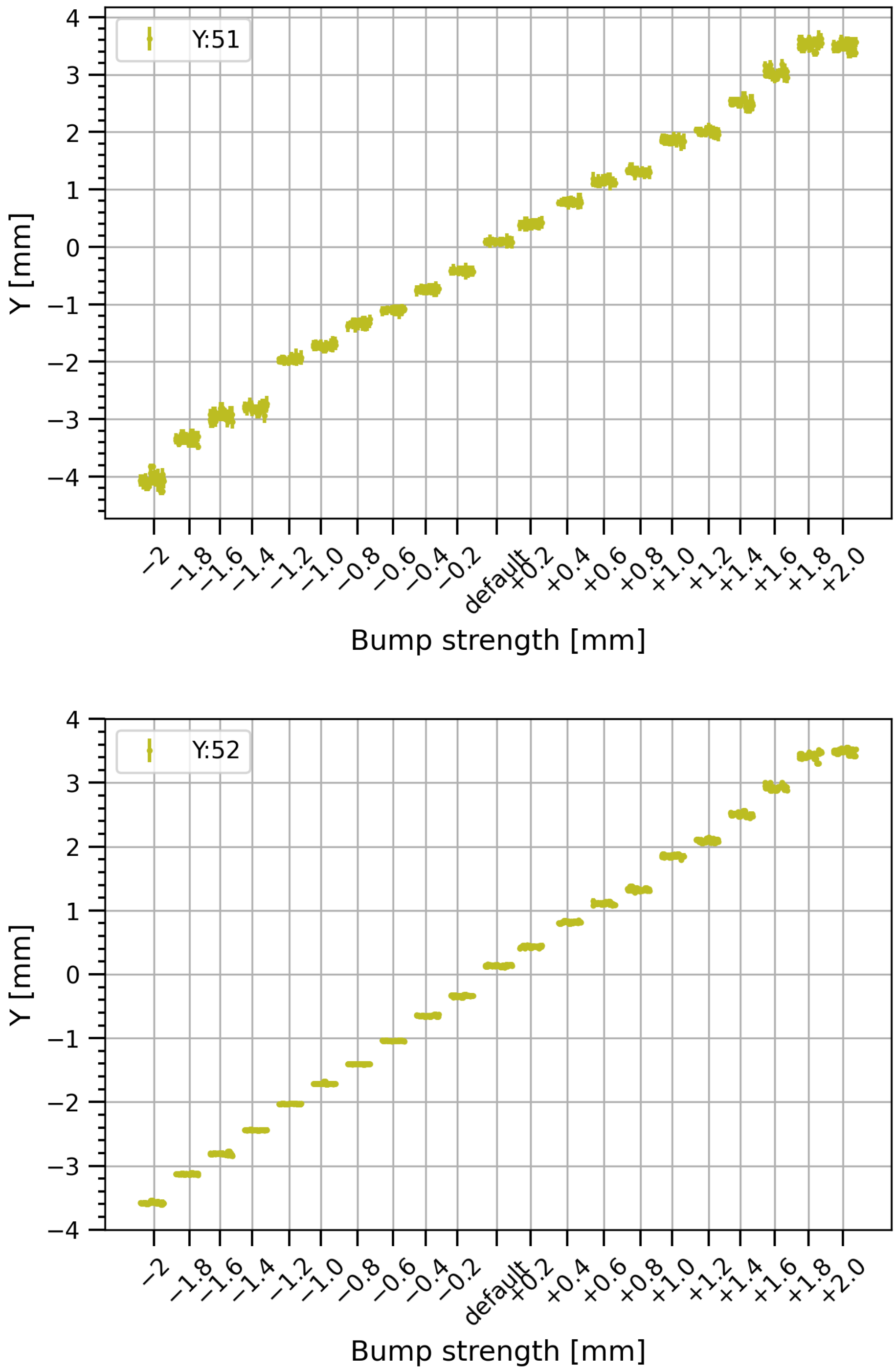

Figure 6.5: The vertical positions measured by the BPM51 (upper plot) after applying parallel vertical local bumps around the RF WF. Similarly, the lower plot shows the vertical positions measured by the BPM52 during the same time of applying the local vertical bumps. During this test, the bumps' settings were varied in the range of ±2 mm with steps of 200 µm, and the COSY was running in the four bunches mode.

6.4 Measured positions

Figure 6.6 shows the positions measured by BPM51 during November/December run in 2018 (at that time, BPM52 was not yet installed). The upper two panels for horizontal (blue) and vertical (green) beam coordinates. The arrows point to the part of the cycle where beam is bunched (during which correct positions should be returned, also highlighted in red oval). The third panel shows the COSY beam current. All figure panels are plotted against the time within three consecutive cycles. To have a closer look at the bunched beam positions only, figure 6.7 is magnifying the bunched beam coordinates from figure 6.6 over the time during the three different cycles. The vertical response (green) is showing a linear increase (about $10 - 15$ µm outside the statistical jitter level) in positions over the time. This change, during one single cycle might be linked to some dependency on the bunching shape (which is not the same at the end of the cycle compared to the beginning) or to some potential voltage offset that might drift with time. Each position data point corresponds to a sampling time of half a second. The errors on single position readouts were in the range of $1 - 3$ µm.

An example of the positions measurement by the BPM52 during the second precursor

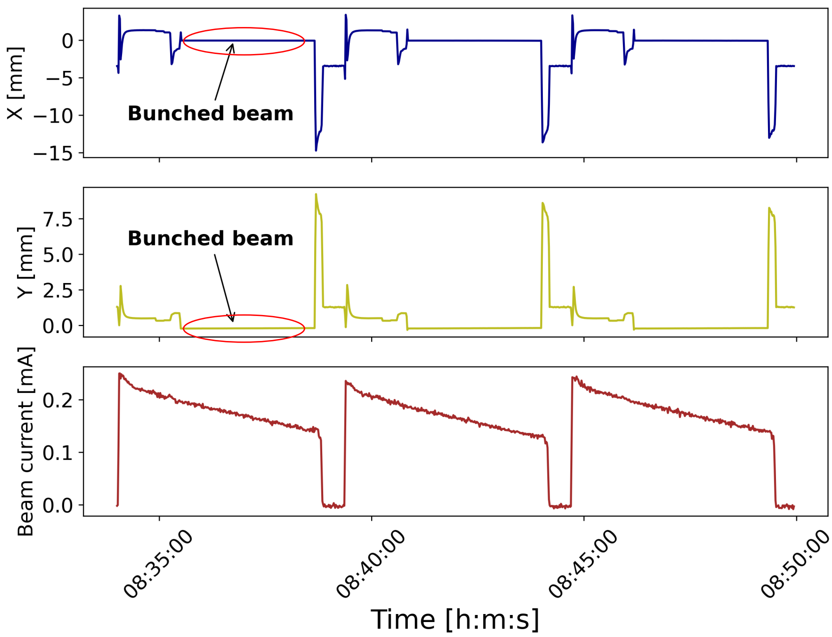

Figure 6.6: Beam positions measured by the BPM51. The upper two panels for the horizontal (blue) and the vertical (green) beam coordinates. The arrows point to the part of the cycle where the beam is bunched (during which correct positions should be returned). The third panel shows the COSY beam current. All figure panels are plotted against the time within three consecutive cycles. Each position data point corresponds to a sampling time of 0.5 s.

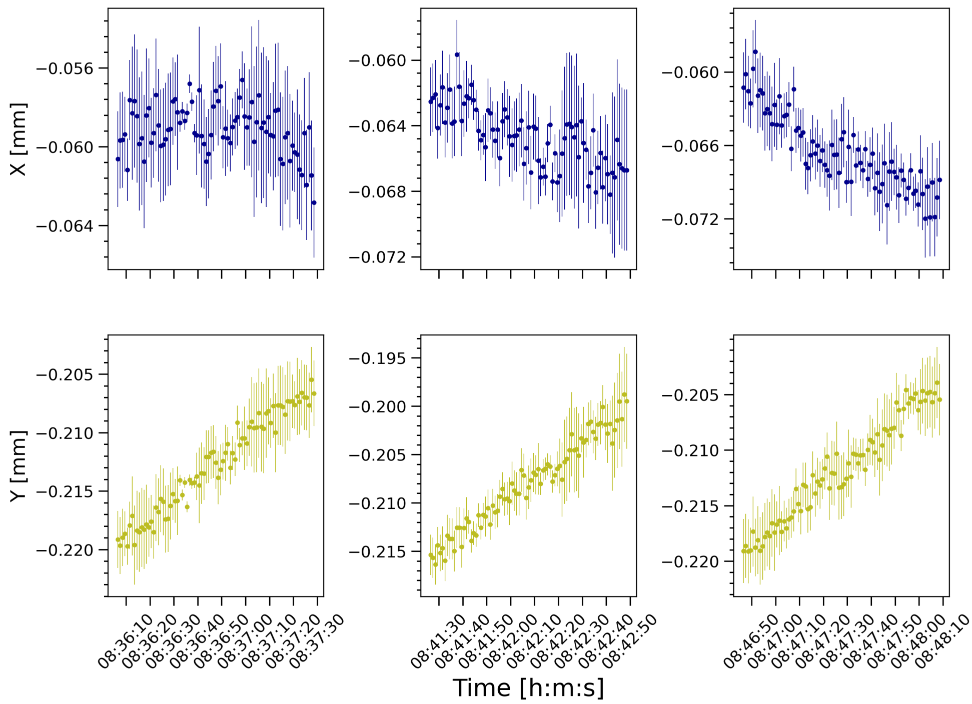

Figure 6.7: A magnified figure for bunched beam positions from figure 6.6 over the time in the three different cycles. The vertical orbit (green) is showing a linear increase (about $10-15$ µm outside the statistical jitter level) in positions over the time.

run in 2021 is shown in figure 6.8 (horizontal positions) and figure 6.9 (vertical positions). The two figures represent the transverse beam coordinates over four consecutive cycles (on March 27) when the COSY was running in the two bunches mode. From figures 6.8 and 6.9, there is a common feature in the shape of the transverse beam coordinates over the different cycles. The positions change by about 20 µm between the beginning and the end of each cycle. However for this change, is not absolutely known whether it is a true change, a faulty change due to some temporal drifts in voltage offsets or even if linked to the bunching state over the course of the cycle.

The resolution, as was stated in the previous chapter, is inversely proportional to the level of the SNR, meaning that more beam intensity should result in better precision. Figure 6.10 shows the horizontal resolution of the BPM51 during two different cycles, one from March 27, 2021 (upper panel) with some beam intensity $I(t)$ (beam current in the range of $0.5-0.65$ mA) while the other cycle from March 12, 2021 when the beam intensity was about a factor of $0.4-0.5$ of the intensity on March 27. The better resolution is clearly achieved for the case of the higher beam intensity. Similarly, results for the horizontal resolution of the BPM52 from the same two cycles are shown in figure 6.11. The vertical resolution for both BPMs were very comparable with the horizontal resolution for each BPM accordingly.

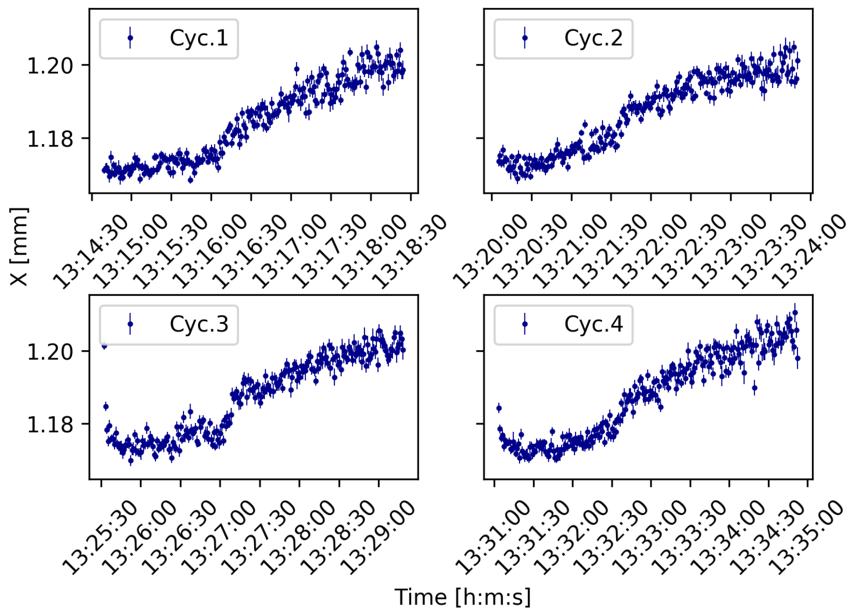

Figure 6.8: Horizontal bunched beam positions measured by the the BPM52 over four consecutive cycles on March 27, 2021. During that run, the COSY was in the two bunches mode.

By comparing the positional resolutions of the two Rogowski BPMs for the same conditions, one can see that the resolution is better by a factor of three for the BPM52 compared with the BPM51. This is attributed to the fact that the two coils are having different bandwidths. The resolution plots correspond to the COSY in the two bunches mode, meaning that the trigger frequency was about 1.5 MHz ($2 \times f_{rev}$). For this particular frequency, the BPM52 is still operating in the inductive region while the BPM51 is behind its self resonance frequency where paracitics and capacitive effects can influence the signal quality.

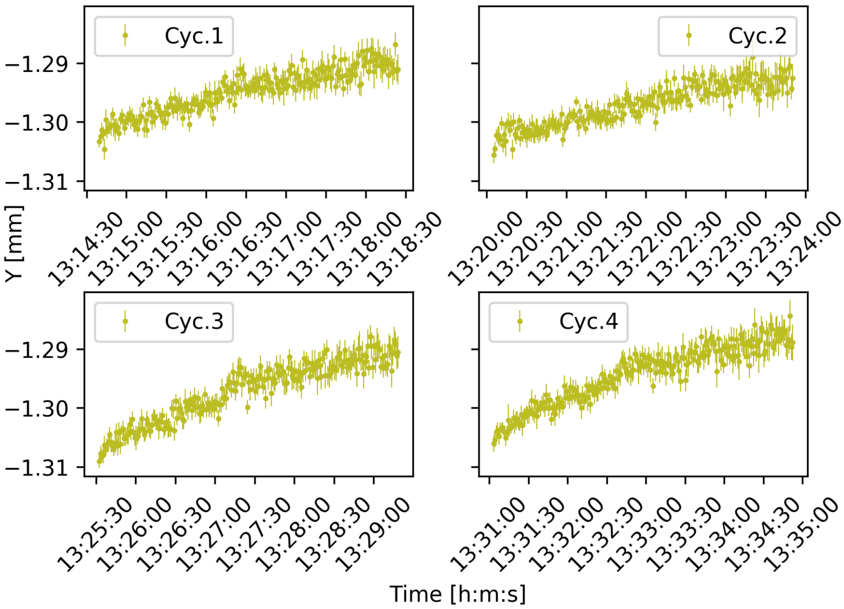

Figure 6.9: Vertical bunched beam positions measured by the BPM52 over four consecutive cycles on March 27, 2021. During that run, the COSY was in the two bunches mode.

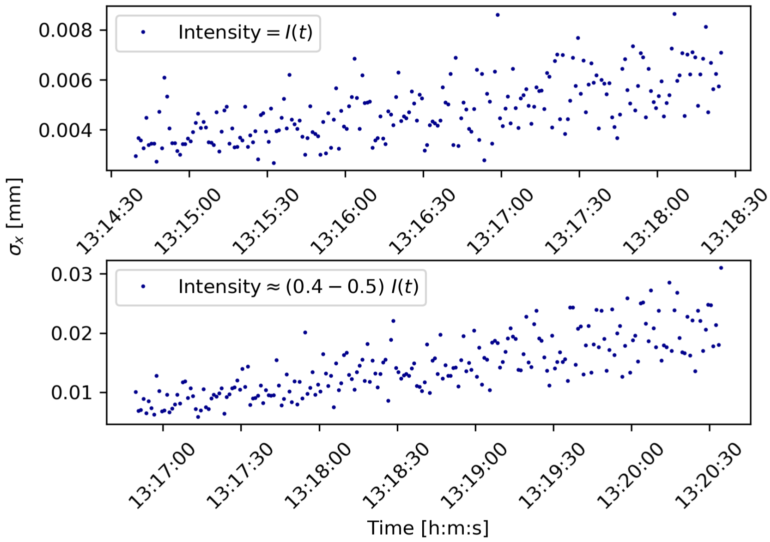

Figure 6.10: The horizontal resolution of the BPM51 during two different cycles. The upper panel from March 27, 2021 with a beam intensity $I(t)$. The lower panel for a cycle from March 12, 2021 when the beam intensity was less ($\approx (0.4-0.5)I(t)$). Each data point in the figure corresponds to a sampling time of 1 s.

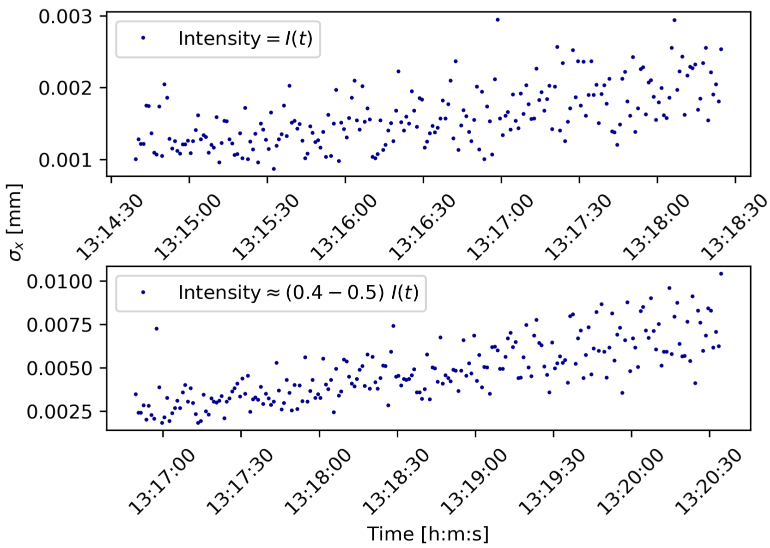

Figure 6.11: the horizontal resolution of the BPM52 during two different cycles. The upper panel from March 27, 2021 with a beam intensity $I(t)$. The lower panel for a cycle from March 12, 2021 when the beam intensity was less ($\approx (0.4-0.5)I(t)$). Each data point in the figure corresponds to a sampling time of 1 s.

6.5 Challenges

Despite the fact that the installed Rogowski BPMs have been successfully tested for a valid operation as position monitors in the accelerator environment, some challenges have been faced during operation times. The installation location of these BPMs next to the WF, for example, is one challenge. The Rogowski BPM were very sensitive to any nearby changes as the rotation of the WF, the operation of the WF or even the operation of some of the WF electronics as the amplifiers and the RF switches [82]. The reason behind sensitivity to such nearby changes can be of several forms. Operating the WF can result in different background especially that the WF operates at the frequency of 871 kHz which is not far away from the beam revolution frequency. The RF switches were operated at the revolution frequency during 2021 precursor run, and this could influence electrical signals from the Rogowski BPMS in close vicinity. Rotation of the WF could result in different background or even different image current distribution‡. For all previously mentioned sources of perturbations in electrical signals, a possible change (faulty) in positional readouts can consequently occur.
An example of such positional faulty changes can be seen in figure 6.12 which shows the change in the Rogowski positions after turning the WF and the RF switches on. The blue and red plots represent the horizontal and vertical positions measured by the BPM52 plotted against the time. The black plot represents the beam current of the COSY signal. The change happened around the second 155 from the beginning of each cycle (the time when the WF was switched on). During the first four cycles, the WF was not operating (no perturbations in positions).
Figure 6.13 shows an example of the Rogowski voltage signal in the time domain from one single quadrant coil (upper left plot) and its FFT (lower left plot) when the WF was switched off. To the right is a magnified plot of the FFT in the left side. The two red dots indicate the peaks at the two frequencies 750 kHz and 871 kHz. Similar demonstration for the same quadrant coil when the WF was switched on is given in figure 6.14. Since the operation of the WF and the RF switches happened later during the cycle, it is expected to see a decreased level of the voltage signal as we move forward in the cycle's time compared with the level before (see beam extraction in figure 6.12). However, what is observed from figures 6.13 and 6.14 is an increase in the signal level at 750 kHz after the operation of the WF and the RF switches (when they were switched on). This can justify the occurrence of some faulty positional changes as was seen in figure 6.12.

One other challenge, was that sometimes the positions measured by the Rogowski BPM used to vary periodically during the cycle's time, which might be linked to a dependence on the beam extraction, or in other words on the beam current. Since the calibration is based on using the $\frac{\Delta}{\Sigma}$, it is then expected to have positions independent from the beam current, especially that the test for voltage offsets is usually performed prior to setting the system for delivering positions. An example for such change of positions during single

‡However, a dedicated test using the laser tracker and the reference fiducials on the top of each Rogowski monitor, was performed in order to insure not having a physical rotation of the BPMs during the rotation of the WF itself. No observations for the move of the BPMs were noticed.

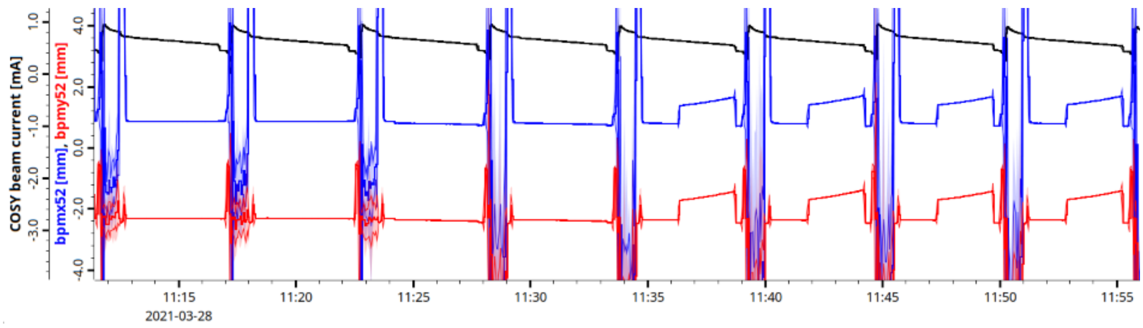

Figure 6.12: The change in Rogowski positions after turning the WF and the RF switches on. The blue and red plots represent the horizontal and vertical positions measured by the BPM52 plotted against the time. The black plot represents the beam current of the COSY signal.The change happened around the second 155 from the beginning of each cycle (the time when the WF was switched on). During The first four cycles, the WF was not operating (no perturbations in positions).

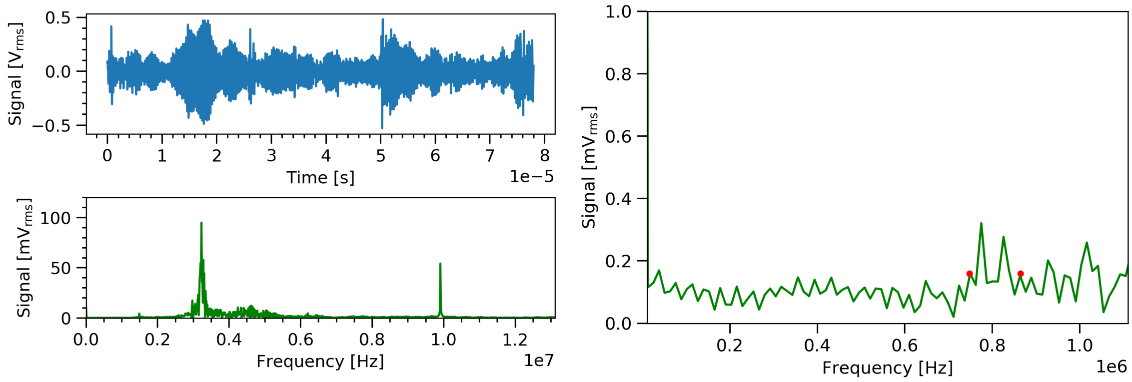

Figure 6.13: Left: the Rogowski's voltage signal in the time domain from one single quadrant coil (upper plot) and its FFT (lower plot) when the WF was switched off. Right: a magnified plot for the FFT in the left side. The two red dots indicate the peaks at the two frequencies 750 kHz and 871 kHz.

cycle's time is manifested in figure 6.15, which shows the horizontal beam coordinates measured by the Rogowski BPM (left side) and by a different capacitive BPM (right side) plotted against the time from one day during an engineering run in November 2020. The insets on the figure are magnifying around the bunched beam positions during one single cycle. Unlike the capacitive typical BPM, the Rogowski BPM's positions showed a change by more than 150 µm during the single cycle. In fact, the actual reason behind such change is not certainly known to be dependence on beam current itself. Other possible reasons can be for example, that the voltage offsets might differ as a result of

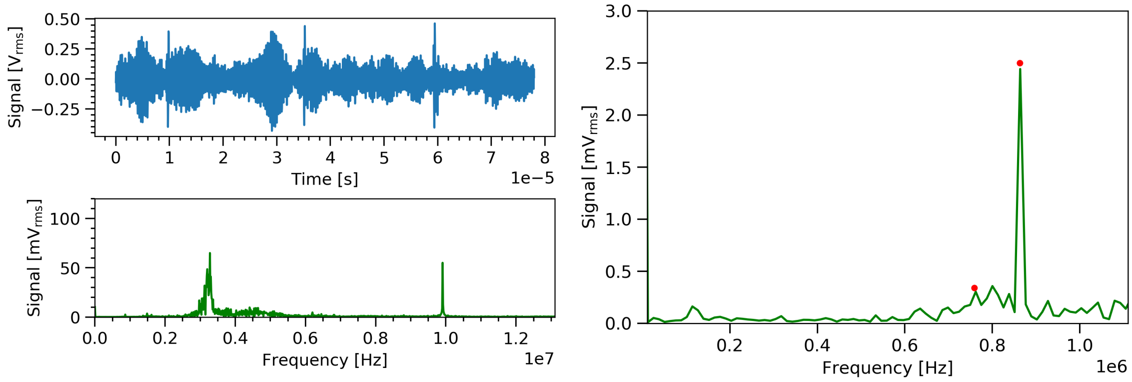

Figure 6.14: Left: the Rogowski'S voltage signal in the time domain from one single quadrant coil (upper plot) and its FFT (lower plot) when the WF was operating. Right: a magnified plot for the FFT in the left side. The two red dots indicate the peaks at the two frequencies 750 kHz and 871 kHz.

having different image current distribution for different beam coordinates.

One of the important things that was investigated (although not deeply), is the possibility of using the Rogowski BPM as a **B**eam **C**urrent **T**ransformer (BCT) at the same time. This was successfully checked in the laboratory and the slope for a linear relation between the sum signal (sum of voltages from the four quadrant coils) made an agreement with theoretical expectations (see the left part of figure 6.16). Unfortunately, the calibration carried out in the laboratory for the Rogowski as a BCT was based on a sinusoidal wave form. The wave form should play a role in the case of the sum signal and the individual quadrants' voltages (unlike the case of the difference over the sum needed for the BPM calibration). Simply because the wave form's time content can differ between distinct wave form sources for the same frequency. Later after installation, the slope was checked again in COSY (see the right part of figure 6.16). The beam profile of COSY pulse is different from a sinusoidal, thus, the slopes are different in the lab and in the COSY environment.
But it is still possible to calibrate the Rogowski as a BCT based on a pulsed wave form in the COSY after installation. In principle, the slope in such a case should not change over time. Figure 6.17 shows the COSY beam current measured by the Rogowski BPM after calibration as a BCT (blue graph) and by a current transformer installed in the COSY ring (orange graph). The graphs represent data from nine consecutive cycles on September 17, 2020. Only when the beam is bunched, a valid comparison between the two current transformers can be made. The dashed black rectangle shows the parts of the two graphs when the beam is bunched during the first cycle (a similar pattern needs to be followed for the remaining cycles). A good agreement between the two monitors can be seen.

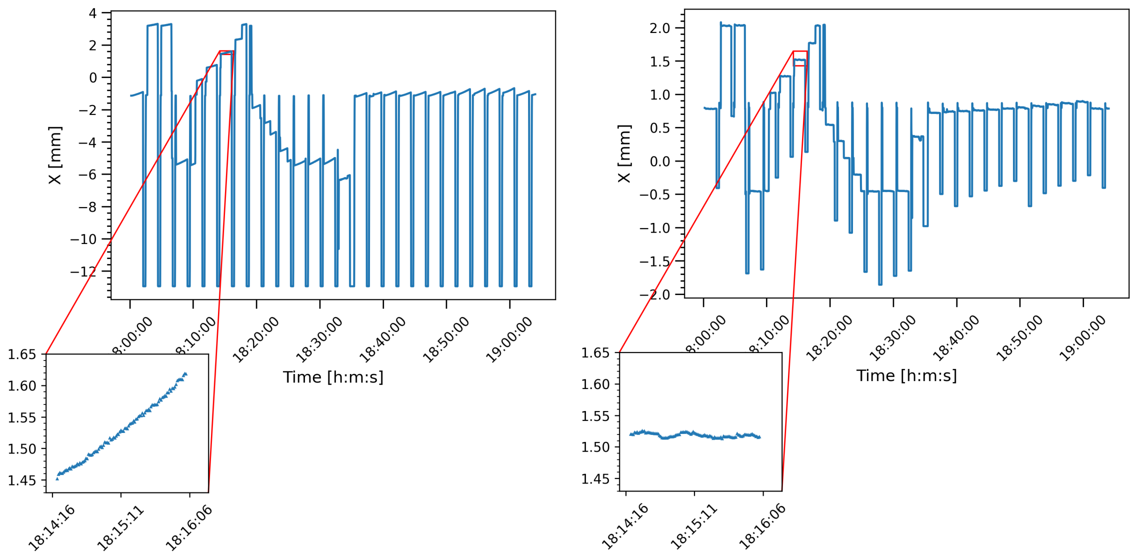

Figure 6.15: The horizontal beam coordinates measured by the Rogowski BPM (left side) and by a different capacitive BPM (right side) plotted against the time from one day during an engineering run in November 2020. The insets on the figure are magnifying around the bunched beam positions during one single cycle. Unlike the capacitive typical BPM, the positions from the Rogowski BPM showed a change with the beam extraction.

However, this agreement, unfortunately, came to an end. It was noticed that, later, after some beam optimization in the bunching, the slope from the Rogowski BCT has increased arriving at a discrepancy of about 200 µA when compared with the COSY BCT values (see figure 6.18). As this was against expectations, it is still not clear why the slope from the sum signal should be different for different bunching state.

Another important issue was the fact that the two installed Rogowski BPMs were originally different and had for instance different bandwidths. This made comparing the transverse beam positions at the entrance and the exit of the WF a challenging mission. Naively, one would expect having same or very similar beam coordinates for such short distance (about one meter, only WF separating them and without steerer magnets in between). However, different coordinates were observed at the two locations reaching in some times a discrepancy of about 2 mm.

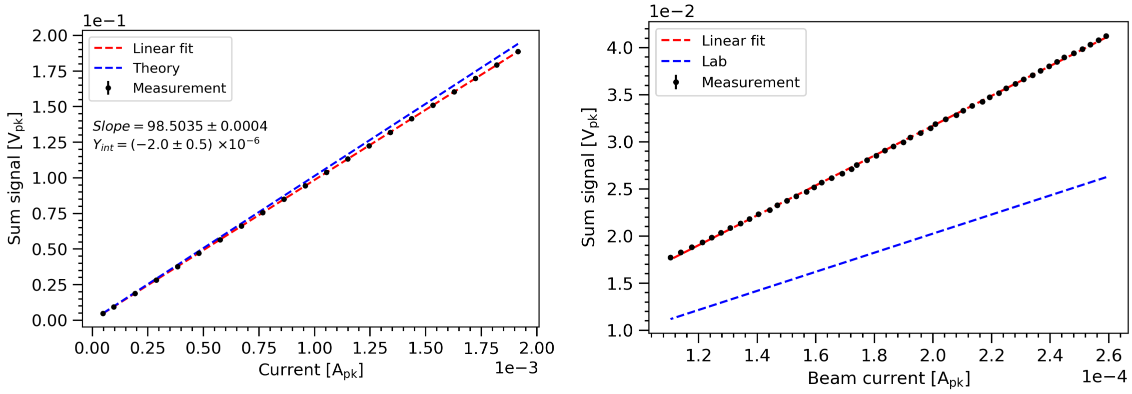

Figure 6.16: Left: the sum signal of the Rogowski BPM as a function of excitation source's current in the laboratory. The source was chosen as a sinusoidal wave form. Black dots represent measurement points, red dashed line represents the linear fit and the blue dashed line represents the theoretical expectation. The slopes of both: the linear fit and the expectation were off by about 2.7%. Similarly, the right side shows the sum signal versus the current of the COSY beam (pulsed wave form). The dashed blue line represents the slope based on the measurement in the laboratory. The effect of the beam wave form on the slope for a BCT usage is clearly seen from the mismatch between the lines on the right side.

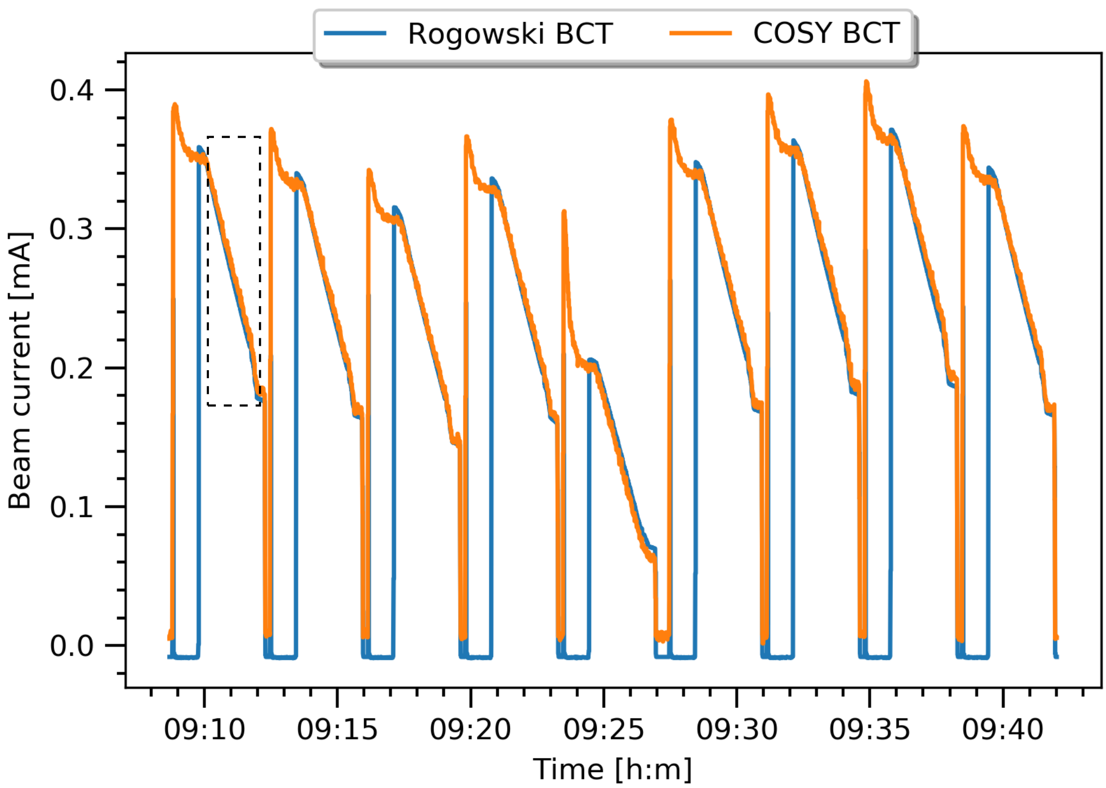

Figure 6.17: The COSY beam current measured by the Rogowski BPM after calibration as a BCT (blue graph) and by a current transformer installed in the COSY ring (orange graph). The graphs represent data from nine consecutive cycles on September 17, 2020. Only when the beam is bunched, a valid comparison between the two current transformers can be made. The dashed black rectangle shows the parts of the two graphs when the beam is bunched during the first cycle (a similar pattern needs to be followed for remaining cycles).

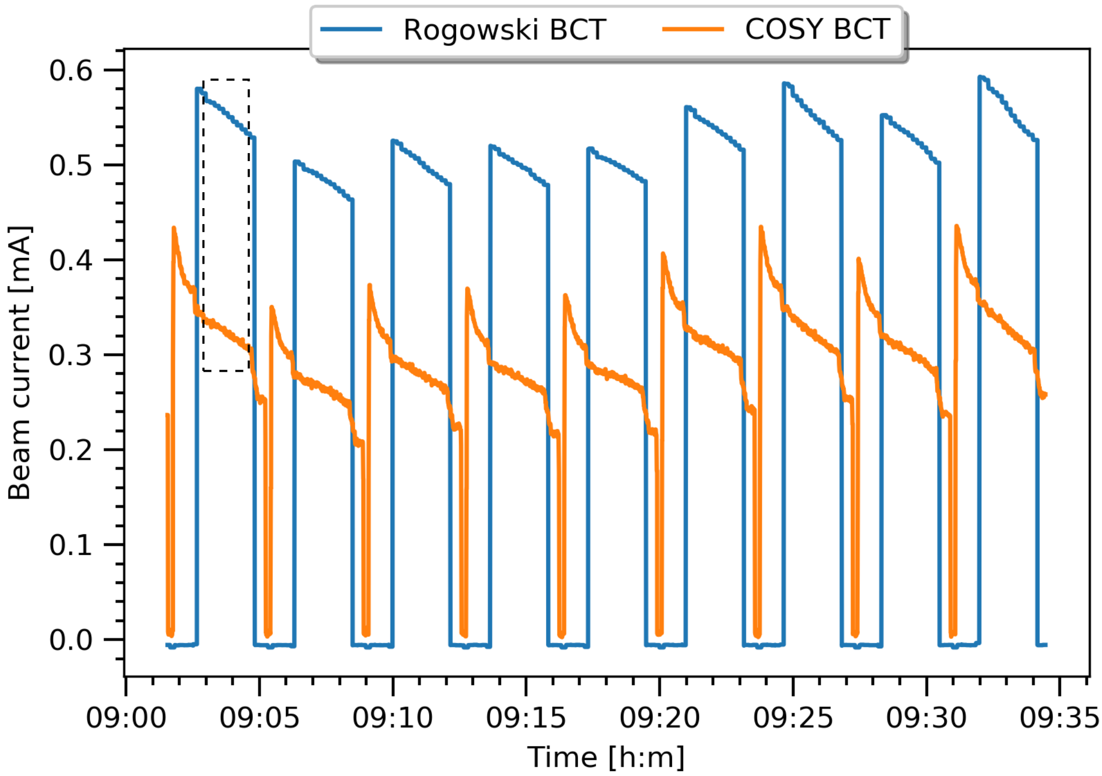

Figure 6.18: The COSY beam current measured by the Rogowski BPM after calibration as a BCT (blue graph) and by a current transformer installed in COSY ring (orange graph). Data was taken from nine consecutive cycles on September 19, 2020 after some optimization in the bunching. Only when the beam is bunched, a valid comparison between the two current transformers can be made. The dashed black rectangle shows the parts of the two graphs when the beam is bunched during the first cycle (a similar pattern needs to be followed for remaining cycles). A discrepancy of about 200 µA between the two monitors is seen.

Chapter 7

Summary and outlook

7.1 Summary

Within the scope of this thesis, a new type of inductive BPM based on a segmented toroidal coil (Rogowski coil) was developed. Different aspects of this Rogowski BPM as a non destructive monitor for measuring beam transverse coordinates are elaborated. The development of the Rogowski BPM comes as a part of the upgrade in the BPM system which is needed for the search for charged particle EDM investigations carried by the JEDI collaboration using the COSY storage ring.
The theoretical model that describes the induced voltages from the Rogowski BPM has been extended using the lumped model approximation to provide a description of induced voltages after measurement. In this extended model, the coupling between individual quadrant coils was included based on the results of magnetic flux derivations. Further theoretical investigations were also carried out to study the effect of the winding angular coverage on the electrical response. In addition, the sensitivity to beam positions was investigated from the windings' orientation point of view.
Electromagnetic simulations carried within COMSOL Multiphysics were used to investigate a simple 3D model for the Rogowski BPM. The simulations were performed in both time and frequency domains. Different boundary conditions were applied to individual quadrants in order to study the coils' electrical features in the frequency domain. The results from a parametric sweep study with a positional grid of a size of $\pm$ 1 cm are in agreement with the theoretical derivations that included the coupling between separate quadrant coils. Furthermore, two models with different winding configurations were investigated and the results for sensitivity of calibration ratios to beam coordinates make an agreement with the theoretical expectations. Another simplified model for a single quadrant coil in the Rogowski BPM was studied assuming a 2D axisymmetric geometry. In this analysis, the impedance and inductance of a single coil were studied over a frequency span of 10 MHz. Based on the results from different analysis in the frequency domain, it is important to pay attention to the geometrical specifications of windings

and to the way the full circuitry is connected. For example, a small change of 10 µm in windings' spacing or even a small capacitance (in the level of few pF) added to the system as a result of terminating the coil with some short coaxial cable, is capable of shifting the effective inductance and thus the expected behavior of a quadrant coil.
Several hardware developments and improvements starting from a simple toroidal coil and arriving at the complete BPM with its feedthroughs, flanges and connectors were achieved. So far, two Rogowski BPMs were developed with different operational bandwidths. One with a turn number of 445 per quadrant and a SRF around 1.2 MHz and the other with a turn number of 132 per quadrant and a SRF around 3.229 MHz. In fact, the motivation behind building the second Rogowski BPM was to ensure having a wider bandwidth that enables using such a monitor for COSY in the four bunches mode, which requires triggering at the fourth harmonic (3 MHz) of the beam revolution frequency.
Developments in the laboratory test-stand enabled more precise calibrations. With the help of the newly developed knife-edged cylindrical structure, the stepping drives and the laser tracker, absolute BPM calibration (with accuracy of few micro meters) is possible after installation in the accelerator. In addition, a new vacuum test-stand has been developed for testing the vacuum of the Rogowski BPM (or any of its separate parts) before installation in the COSY ring.
Different important experiments were carried out in the laboratory. The frequency response (voltages versus frequencies), the position response (voltages versus positions), the stability of resonance curves, and signal temporal variations were all investigated.
The calibration measurement of the Rogowski BPM was performed in the test-stand and compared with the theoretical model. Deviations between measurement and model were on the level of few micro volts (for an amplified signal).
Stability of the calibration measurement was studied by repeating the same calibration 30 times. The maximum positional error introduced by temporal drifts which were observed from repeating the calibration, was in the range of $15 - 20$ µm (which represents three standard deviations for one single position measurement when the beam was off-centered by about 1 cm).
The behavior of voltage signals from the Rogowski BPM over the time without necessarily performing the calibration measurement as a probe for temporal stability was also investigated. The voltage signal was recorded over $20 - 24$ hours. The distributions of recorded data have shown an overlapping of multiple Gaussians. The level of temporal variations in electrical signal (taking the means from different Gaussians) was about few micro volts. However, no observations for a link between the temporal change in voltages and the temperature or the humidity changes inside the test environment. Furthermore, despite the multiple Gaussians in voltage distributions, the SNR was normally distributed for the same recorded data, which means that the several Gaussians are attributed to some noise or background related reasons.
The effect of the source signal wave form on the BPM calibration was also tested. Two wave forms were selected, one as sinusoidal and the other as pulse which looks similar to a realistic beam signal in COSY. The resulting effect on the calibration ratios introduced a positional error of about 30 µm considering the linear approximation in the position

dependence. Therefore, it is more advisable when calibrating the BPM to use a waveform which is identical to a beam signal in COSY especially if the BPM was intended to be exploited as a BCT, where the effect of the time content of the source wave form on the sum signal plays a major role.
The SNR from one single quadrant coil can vary depending on many factors as the frequency of operation, measurement settings as the input impedance and input level of measuring devise or the low pass filter cut-off frequency, in additions to the amplitude of beam current. In general, the SNR for the Rogowski BPM can be in the range of few thousands.
The two developed Rogowski BPMs (BPM51 and BPM52) were successfully installed and tested in the COSY ring. The installation was made at the entrance and the exit of the RF WF. The results from local and parallel orbit bumps around the WF when COSY was running in the single bunch mode (triggering at 750 kHz) have shown reasonable position responses measured by the two BPMs as the responses were linear with the applied bump strength, in addition to the agreement between the positions of the two BPMs.
Another test of local and parallel orbit bumps was also applied when COSY was running in the four bunches mode (triggering at 3 MHz). With bump steps of 200 µm, linearity in response was still conserved to some extent. In addition, the maximum difference between the measured positions at the two BPM locations was bigger than the case of the single bunch. At the frequency of 3 MHz, the BPM52 is getting close to its SRF (but still in the inductive region) while the BPM51 is already behind its SRF. This may justify the higher fluctuations in measured positions during single cycles, also it can justify the fact that the BPM51 was less linear with respect to different bump settings which also led to bigger differences between the positions at the two BPM locations compared with the results of the single bunch case where both BPMs were below their SRF (in the inductive region).
With the newly proposed procedure for absolute device calibration, and considering both the accuracy of stepping drives used in calibration procedures, and the errors introduced by temporal drifts, the accuracy of the Rogowski BPM is expected to be around 20 µm, arriving at an improvement by a factor of five when compared with the accuracy of the typical BPMs. Moreover, the compactness of these Rogowski BPMs with an insertion factor of about 10 cm is a significant advantage.
A change in positions during single cycles (up to 20 µm) was observed sometimes during the operation in COSY. This change might be a true change (although not very probable), linked to some dependency on the bunching shape which is not the same at the end of the cycle compared to its beginning or linked to some potential voltage offset that might drift with time. However this change was even much bigger some other times exceeding the 150 µm (unlike typical capacitive BPMs where positions used not to vary with beam extraction over single cycles). This big observed change is not certainly known to be dependent on the beam current itself, other possible reasons can be for example that the voltage offset might differ as a result of having different image current distribution for different beam coordinates.

It was also observed that the Rogowski BPMs are very sensitive to any nearby physical change, as the rotation and operation of the WF. A special attention has to be given to the location of installation in order to have a previous understanding and control for all possible factors that might influence the signal or the background level which thus can introduce some positional errors. Another critical parameter that has to be considered, is the electrical properties of the sensor itself. When building or assembling a Rogowski BPM, it is very important to make sure that the sensor is in the inductive region and below its SRF at the frequency of operation which can help improving the system stability and the positional resolution.
For precision EDM searches, JEDI aims at an experimental goal with systematic errors to be in the same level as that of the statistical sensitivity (10^{-29} e cm per year of data taking). The MDM is many orders of magnitude greater than the EDM, this necessarily requires a good control for systematic errors as radial magnetic fields, magnets misalignment or non-radial electric fields. Such sources can result due to MDM in an out of plane spin precession which is indistinguishable from a true EDM signal. According to the investigations carried out in [24], quadruples misalignments can lead to a vertical polarization build up when using the RF WF such that a vertical orbit RMS of 130 μm (as a result of misaligned magnets) can induce a polarization build up (by MDM effect) with the same strength of a true EDM signal of 5×10^{-20} e cm. This raises the importance of having a beam orbit very close to the magnetic center. The orbit RMS should be as close to the zero as possible. To this end, a system of highly precise BPMs will be needed. With the Rogowski BPMs, resolution down to few hundreds of nano meters is achievable, which means an improvement by one order of magnitude in the resolution in comparison with typical capacitive BPMs in COSY. A summary of the resolution* of the Rogowski BPM based on different measurements in the laboratory and the accelerator COSY is given in table 7.1. The values of I in the last column represent the magnitude of the source current (laboratory) or the beam current (COSY). The SRF represents the SRF of a single quadrant coil in Rogowski BPM.

*The values of the measured resolution listed in table 7.1 correspond to one single position measurement based on a sampling time of 1 s. The theoretical limit for the spacial resolution is given by eq 5.12 as described in chapter 5.

Table 7.1: The Resolution of the Rogowski BPM based on different measurements in the laboratory and the accelerator COSY for a sampling time of 1 s.

Subject	Value	Measurement frequency	Notes
Resolution laboratory	2.94 µm	750 kHz	$I = 0.24$ mA SRF = 1.2 MHz
Resolution laboratory	1.83 µm	750 kHz	$I = 0.46$ mA SRF = 3.229 MHz
Resolution laboratory	7.85 µm	3 MHz	$I = 0.46$ mA SRF = 3.229 MHz
Resolution accelerator	$1-3$ µm	750 kHz	$I = 0.4-0.6$ mA SRF = 1.2 MHz
Resolution accelerator	$0.4-1$ µm	750 kHz	$I = 0.4-0.6$ mA SRF = 3.229 MHz
Resolution accelerator	$3-8$ µm	1.5 MHz	$I = 0.6-0.7$ mA SRF = 1.2 MHz
Resolution accelerator	$1-3$ µm	1.5 MHz	$I = 0.6-0.7$ mA SRF = 3.229 MHz

7.2 Outlook

As a follow up for the ongoing EDM studies in COSY, the construction of a prototype ring is anticipated to start after 2022 [83]. With the compactness advantage (insertion factor of less than 10 cm) of the Rogowski BPM, several of such Rogowski BPMs in the design of the prototype ring are required to be installed in different locations.
In this proposed ring, two beams will be injected, one in the clockwise (CW) direction and the other in the counter-clockwise (CCW) direction. The radial magnetic fields represent one major source of systematics which cause a vertical splitting for the two counter-rotating beams [84, 85]. This means that equipped BPMs should have suitable sensitivity low enough to the desired level that meets the EDM experimental goals. In fact, since only relative positions of the two counter-rotating beams matter to the first place, the effect of the absolute accuracy will drop out and only the resolution plays a role. As stated earlier, a resolution of around 400 nm is possible for the Rogowski BPM (for sampling time of 1 s with beam current of about 0.6 mA which translates into a particle intensity of about 5×10^9). For a beam intensity of the order of 4×10^{10} as proposed for the future operation in the prototype ring, the SNR can be improved by a factor of 8 which means that a resolution of about 50 nm will be possible. As a part of future steps, the operation of the Rogowski BPMs in the case of CW/CCW beams needs to be fully investigated in order to fulfill the requirements of the EDM measurement.
When designing the Rogowski BPMs, it is very important to understand the complete system and its limitations. Also, in order to provide the required measurement, one needs to take into account all operating conditions of the accelerator environment. A deep understanding for reasons behind the observed positional change during single cycles is required in order to have a calibration perfectly independent from the beam extraction. Further investigations are also needed to study the effect of bunch shape on the behavior of the Rogowski coil as both a BPM and a BCT.

Additionally, the existing electronics can provide bunch-to-bunch positions (μs time scale), but on the other hand the resulting resolution will be very bad (wider filter window). For this, an upgrade in the readout electronics where both good spacial and time resolutions are achieved, will be needed for future developments.

Appendix A

A.1 Rogowski lumped model

A.1.1 Transfer function

From the Rogowski lumped model as illustrated in Figure A.1 panel (b), one can write the transfer function $H(s)$ as:

$$\begin{aligned} H(s) &= \frac{U_{\text{out}}}{U_{\text{in}}}, \\ &= \frac{-i/LC}{s^2 + s\frac{L+RR_1C}{R_1LC} + \frac{R+R_1}{R_1LC}}, \end{aligned} \tag{A.1}$$

with U_{out} and U_{in} are the measured and induced voltages, respectively. i is the imaginary unit number. s is the Laplace variable and R_1 is the input impedance of the measuring devise. The frequency response of a system relates the output to a sinusoidal input at some angular frequency ω. Going from the transfer function $H(s)$ into the frequency response $H(i\omega)$ by substituting the Laplace s with $i\omega$ yield in:

$$H(s)|_{s=i\omega} = |H(i\omega)|e^{i\angle H(i\omega)}\,. \tag{A.2}$$

$|H(i\omega)|$ and $\angle H(i\omega)$ represent the amplitude and the phase response, respectively. The amplitude response from eq. (A.2) is expressed as:

$$|H(i\omega)| = \frac{1}{\sqrt{(1-(\frac{\omega}{\omega_0})^2)^2 + (\frac{\omega}{\omega_1})^2}}, \tag{A.3}$$

$$|H(i\omega)| = \left|\frac{U_{\text{out}}}{U_{\text{in}}}\right|. \tag{A.4}$$

For simplicity, we can write the right side of eq. (A.3) as $\gamma(\omega_0, \omega_1, \omega)$. The expressions for ω_0 and ω_1 are:

$$\omega_0 = 1/\sqrt{LC}\,, \tag{A.5}$$

$$\omega_1 = \frac{R_1}{L + R_1RC}\,. \tag{A.6}$$

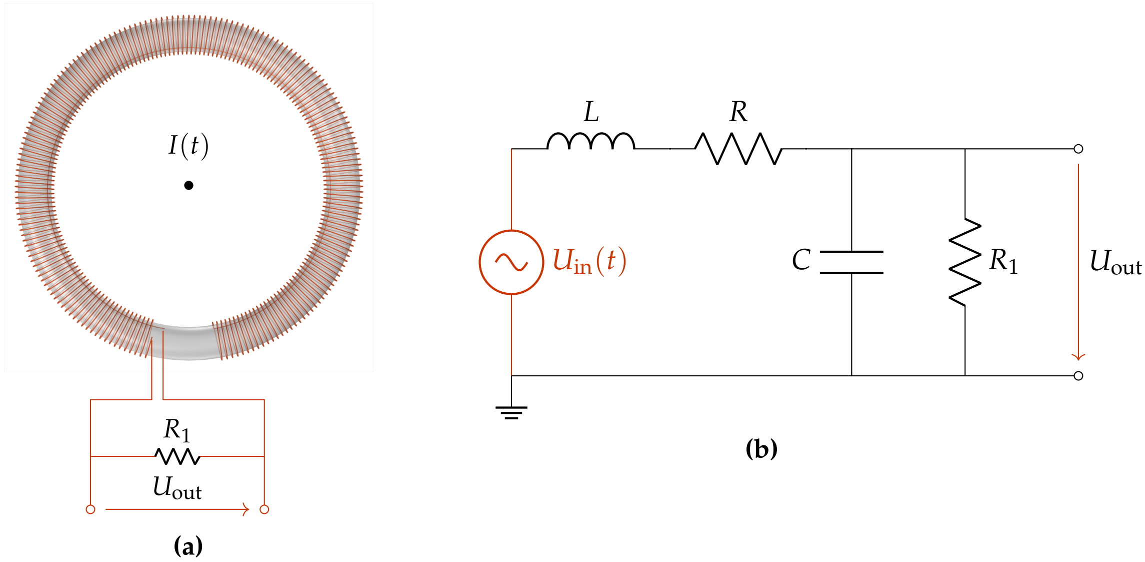

Figure A.1: Realization of typical Rogowski winding used for sensing a current $I(t)$ and how its output signal results (a). Equivalent circuit for the induced voltage measurement using the lumped elements (R L and C) approximation. U_{in} is the induced signal, U_{out} is the measured one and R_1 is the input impedance of the measuring device (b).

If the input impedance of the measuring devise is very high ($1\,\text{M}\Omega$), then $\frac{L}{R_1} << 1$ and ω_1 reduces to $\frac{1}{RC}$.
Eq. (A.3) allows for expressing the measured induced voltage signal from a single Rogowski quadrant as:

$$U_{\text{out}} = \gamma(\omega_0, \omega_1, \omega) U_{\text{in}} \,. \tag{A.7}$$

For simplicity again, eq. (A.7) can be written as:

$$U_{\text{out}}(x, y, \omega) = \omega\gamma(\omega_0, \omega_1, \omega)\alpha \,, \tag{A.8}$$

where α represents a product of all frequency independent factors including the beam transverse positions.

A.1.2 Resonance frequency

At the resonance frequency ω_r, the Rogowski quadrant coil reaches its maximum output level ($U_{\text{out max}}$). From eq. (A.8), $U_{\text{out max}}$ occurs when $\omega\gamma(\omega_0, \omega_1, \omega)$ reaches its maximum possible value . This should imply:

$$\frac{\partial}{\partial\omega}\,\omega\gamma\,\Bigg|_{\omega=\omega_r} = 0\,,$$

$$\gamma - \omega\gamma^3\left[-2\frac{\omega}{\omega_0^2}\left(1 - \frac{\omega^2}{\omega_0^2}\right) + \frac{\omega}{\omega_1^2}\right] = 0\,. \tag{A.9}$$

Since $\gamma \neq 0$, then both sides of eq. (A.9) can be safely multiplied by γ^{-3} (γ is used as a shortcut for $\gamma(\omega_0, \omega_1, \omega)$) leading to:

$$\frac{1}{\gamma^2} - \omega\left[-2\frac{\omega}{\omega_0^2}(1 - \frac{\omega^2}{\omega_0^2}) + \frac{\omega}{\omega_1^2}\right] = 0\,. \tag{A.10}$$

From the above Equation we arrive at:

$$1 - \frac{\omega_r^4}{\omega_0^4} = 0\,. \tag{A.11}$$

It is clear from eq. (A.11) that the resonance occurs when $\omega_r = \omega_0$. At this particular frequency, $\omega\gamma$ is peaking up as mentioned earlier. At this peak level, the maximum value yielded is equal to:

$$\begin{aligned} U_{\text{out max}} &= U_{\text{out}}\big|_{\omega=\omega_0}\,, \\ &= \omega_1 \alpha\,. \end{aligned} \tag{A.12}$$

A.1.3 Quality Factor

In order to investigate the quality factor, the bandwidth at which the maximum power is reduced by a factor of half has to be determined. When the power P is halved, the voltage squared should be halved as well ($P \propto U_{\text{out}}^2$) and hence at this level:

$$|U_{\text{out}}|^2 = |U_{\text{out max}}|^2/2\,. \tag{A.13}$$

By substituting eqs. (A.8) and (A.12) into eq. (A.13) we arrive at:

$$\omega^2 = \omega_1^2(1 - \frac{\omega^2}{\omega_0^2})^2\,, \tag{A.14}$$

and then taking the square root for both sides of eq. (A.14), two possible solutions are encountered:

$$\omega = \omega_1(1 - \frac{\omega^2}{\omega_0^2})\,, \tag{A.15}$$

$$\omega = -\omega_1(1 - \frac{\omega^2}{\omega_0^2})\,. \tag{A.16}$$

The solutions for eqs. (A.15) and (A.16) are:

$$\omega_{+1} = \frac{-\omega_0^2}{2\omega_1} + \frac{\omega_0^2}{2\omega_1}\sqrt{1+\frac{4\omega_1^2}{\omega_0^2}}\,, \tag{A.17}$$

$$\omega_{-1} = \frac{-\omega_0^2}{2\omega_1} - \frac{\omega_0^2}{2\omega_1}\sqrt{1+\frac{4\omega_1^2}{\omega_0^2}}\,, \tag{A.18}$$

$$\omega_{+2} = \frac{\omega_0^2}{2\omega_1} + \frac{\omega_0^2}{2\omega_1}\sqrt{1+\frac{4\omega_1^2}{\omega_0^2}}\,, \tag{A.19}$$

$$\omega_{-2} = \frac{\omega_0^2}{2\omega_1} - \frac{\omega_0^2}{2\omega_1}\sqrt{1+\frac{4\omega_1^2}{\omega_0^2}}\,. \tag{A.20}$$

Clearly, the quantity $\sqrt{1+\frac{4\omega_1^2}{\omega_0^2}}$ is greater than 1, for this reason, the solutions in eqs. (A.18) and (A.20) are disregarded since they represent negative values. By this, the bandwidth at half maximum power becomes:

$$\begin{aligned} \Delta\omega \quad &= \omega_{+2} - \omega_{+1}\,, \\ &= \frac{\omega_0^2}{\omega_1}\,. \end{aligned} \tag{A.21}$$

Arriving at the quality factor expression:

$$\begin{aligned} Q \quad &= \omega_0/\Delta\omega\,, \\ &= \omega_1/\omega_0\,, \\ &= \frac{\sqrt{L}}{R\sqrt{C}}\,. \end{aligned} \tag{A.22}$$

A.2 Incomplete winding coverage

Following the magnetic flux derivations made in Ref. [39], the induced voltage for a single quadrant coil reads:

$$
\begin{aligned}
U_{\text{in}}(x,y,\omega) = \; & \frac{n\mu_0}{2\Delta\psi}\omega I\Big[2\Delta\psi(R-u) + 2r_0\big[\sin(\psi_1-\phi_0+\Delta\psi) - \sin(\psi_1-\phi_0)\frac{R-u}{u}\big] \\
& + \frac{r_0^2}{2}\big[\sin(2(\psi_1-\phi_0+\Delta\psi)) - \sin(2(\psi_1-\phi_0))\frac{a^2}{u^3}\big] \\
& + \frac{r_0^3}{3}\big[\sin(3(\psi_1-\phi_0+\Delta\psi)) - \sin(3(\psi_1-\phi_0))\frac{Ra^2}{u^5}\big] \\
& + \frac{r_0^4}{4}\big[\sin(4(\psi_1-\phi_0+\Delta\psi)) - \sin(4(\psi_1-\phi_0))\frac{a(a^2+4R^2)}{u^7}\big] \\
& + \frac{r_0^5}{5}\big[\sin(5(\psi_1-\phi_0+\Delta\psi)) - \sin(5(\psi_1-\phi_0))\frac{a^2R(3a^2+4R^2)}{4u^9}\big]\Big],
\end{aligned}
\tag{A.23}
$$

where R and a are the radii of the coil as stated earlier (see figure 2.2), $u = \sqrt{R^2-a^2}$. r_0 represents the magnitude of the vector pointing from the origin towards the beam center. The angle ψ_1 spans the range between the vector to the start of winding of the quadrant coil and the positive x-axis. The angle $\Delta\psi$ covers the range between the vectors to the start and the end of windings in the quadrant coil. The angle ϕ_0 is made by the vector to beam position with respect to the positive x-axis. A representation in the xy-plane for the coil and the different angles ψ_1, ϕ_0 and $\Delta\psi$ is shown in figure A.2.
If we start with the quadrant coil 1, from symmetry (for all quadrants), one can use:

$$\Delta\psi = \frac{\pi}{2} - 2\psi_1\,. \tag{A.24}$$

And using the following trigonometric relations:

$$
\begin{aligned}
&\sin(2x) = 2\sin(x)\cos(x)\,,\\
&\cos(2x) = -\sin^2(x)+\cos^2(x)\,,\\
&\sin(3x) = 3\sin(x)\cos^2(x) - \sin^3(x)\,,\\
&\cos(3x) = -3\sin^2(x)\cos(x)+\cos^3(x)\,,\\
&\sin(4x) = 4(\sin(x)\cos^3(x) - \cos(x)\sin^3(x))\,,\\
&\cos(4x) = \cos^4(x)+\sin^4(x) - 6\cos^2(x)\sin^2(x)\,,\\
&\sin(5x) = \sin^5(x) - 10\sin^3(x)\cos^2(x) + 5\sin(x)\cos^4(x)\,,\\
&\sin(5x) = \cos^5(x) - 10\sin^2(x)\cos^3(x) + 5\sin^4(x)\cos(x)\,,\\
&\sin(A+B) = \sin(A)\cos(B)+\cos(A)\sin(B)\,,\\
&\cos(A+B) = \cos(A)\cos(B)-\sin(A)\sin(B)\,,\\
&\sin(n\pi+x) = (-1)^n\sin(x)\,,\\
&\cos(n\pi+x) = (-1)^n\cos(x)\,.
\end{aligned}
$$

The linear term (first power in position dependence) where the beam transverse coordinates are implicitly given through r_0 and ϕ_0 ($x = r_0\cos(\phi_0)$ and $y = r_0\sin(\phi_0)$) then reads*:

$$(\cos(\psi_1) - \sin(\psi_1))(x+y)\,. \tag{A.25}$$

While the term with degree two reads:

$$(\cos^2(\psi_1) - \sin^2(\psi_1))xy\,. \tag{A.26}$$

The degree three term is:

$$(\cos(3\psi_1) + \sin(3\psi_1))(-x^3 - y^3 + 3x^2y + +3y^2x)\,. \tag{A.27}$$

The degree four term, which vanishes in the case of full quadrant's angular coverage (when $\Delta\psi = \frac{\pi}{2}$) does not vanish in this case, reads:

$$2\sin(4\psi_1)(-x^4 - y^4 + 6x^2y^2)\,. \tag{A.28}$$

The degree five term reads:

$$(\cos(5\psi_1) - \sin(5\psi_1))(x^5 + y^5 - 10x^2y^3 - 10x^3y^2 + 5yx^4 + 5xy^4)\,. \tag{A.29}$$

Putting all of this together in eq. 1.5 we arrive at:

$$\begin{aligned} U_{\text{in1}}(x,y,\omega) = {} & n\mu_0\omega I c_0^\dagger \Big[1 + c_1^\dagger(x+y) + c_2^\dagger(xy) + c_3^\dagger(-x^3 - y^3 + 3yx^2 + 3xy^2) \\ & + c_4^\dagger(-x^4 - y^4 + 6x^2y^2) + c_5^\dagger(x^5 + y^5 - 10x^3y^2 - 10y^3x^2 + 5y^4x + 5x^4y) \Big]\,. \end{aligned} \tag{A.30}$$

Table A.1: The geometrical parameters for incomplete winding angular coverage.

Parameter	Expression
$c_0^\dagger$	$R - u$
$c_1^\dagger$	$\frac{(\cos(\psi_1) - \sin(\psi_1))}{u\Delta\psi}$
$c_2^\dagger$	$\frac{(\cos^2(\psi_1) - \sin^2(\psi_1))a^2}{4u^3(R-u)\Delta\psi}$
$c_3^\dagger$	$\frac{(\cos(3\psi_1) + 3\sin(\psi_1))Ra^2}{6u^5(R-u)\Delta\psi}$
$c_4^\dagger$	$\frac{\sin(4\psi_1)a(a^2+4R^2)}{4u^7(R-u)\Delta\psi}$
$c_5^\dagger$	$\frac{(\cos(5\psi_1) - \sin(5\psi_1))a^2R(3a^2+4R^2)}{40u^9(R-u)\Delta\psi}$

*The geometrical coefficients that hold R, a and u and other numerals will be added later to full expansion.

For the rest of the quadrant coils, the same way is followed by substituting each coil's initial winding angle as: $\psi_2 = \frac{3\pi}{2} + \psi_1$ for quadrant 2, $\psi_3 = \pi + \psi_1$ for quadrant 3 and $\psi_4 = \frac{\pi}{2} + \psi_1$ for quadrant 4 together with eq. A.24 we arrive again at:

$$\begin{aligned} U_{\text{in1}}(x, y, \omega) \qquad &= U_{\text{in2}}(x, -y, \omega)\,, \\ &= U_{\text{in3}}(-x, -y, \omega)\,, \\ &= U_{\text{in4}}(-x, y, \omega)\,. \end{aligned} \tag{A.31}$$

which are the same for complete angular coverage.
The expression for the geometrical parameters ($c^{\dagger}$ terms) are given in the next table A.1. In contrast to the geometrical parameters obtained for the incomplete angular coverage case as listed in table A.1, the values of these parameters in case of the windings' full angular range are listed in table A.2.

Table A.2: The geometrical parameters for complete winding angular coverage.

Parameter	Expression
c_0	$R - u$
c_1	$\frac{2}{\pi u}$
c_2	$\frac{a^2}{2\pi u^3(R-u)}$
c_3	$\frac{Ra^2}{3\pi u^5(R-u)}$
c_4	$\frac{a(a^2+4R^2)}{4\pi u^7(R-u)}$
c_5	$\frac{a^2R(3a^2+4R^2)}{20\pi u^9(R-u)}$

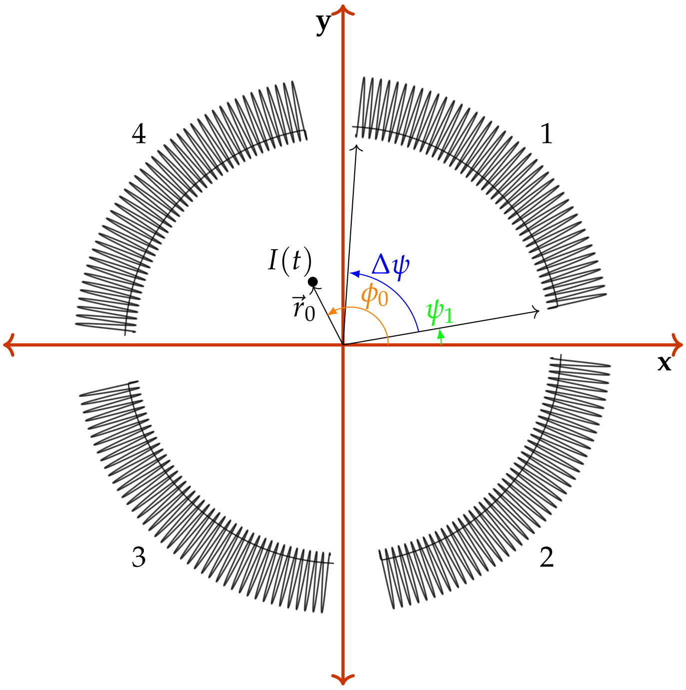

Figure A.2: Rogowski BPM winding viewed in the xy-plane. Numbers 1 to 4 indicate the quadrant coil number 1 through 4. The vector $\vec{r}_0$ points from the origin towards the beam $I(t)$ center which goes in the longitudinal direction. The angle ψ_1 spans the range between the vector to the initial winding of the quadrant coil and the positive x-axis. The angle $\Delta\psi$ covers the range between the vectors to the start and the end of windings in the quadrant coil. The angle ϕ_0 is made by the beam position vector $\vec{r}_0$ with respect to the positive x-axis.

Appendix B

B.1 Transient study

The same time dependent study mentioned in chapter 3 was repeated with the same mesh features, geometry, physics and boundary conditions but with only one difference that the parallel capacitors added to each quadrant coil were excluded. The main goal was to check if the distortions seen in the time response for voltage signals were really coming from the long settling time as a result of the delay caused by the capacitors. Figure B.1 shows the four-voltage response from the four quadrants of the Rogowski BPM over a span of 10 μs. The system settles after less than half a micro second. The number of complete wavelengths also agrees with the excitation signal frequency of 750.6 kHz. This result means that the previously mentioned distortions were indeed caused by the settling time's effect.

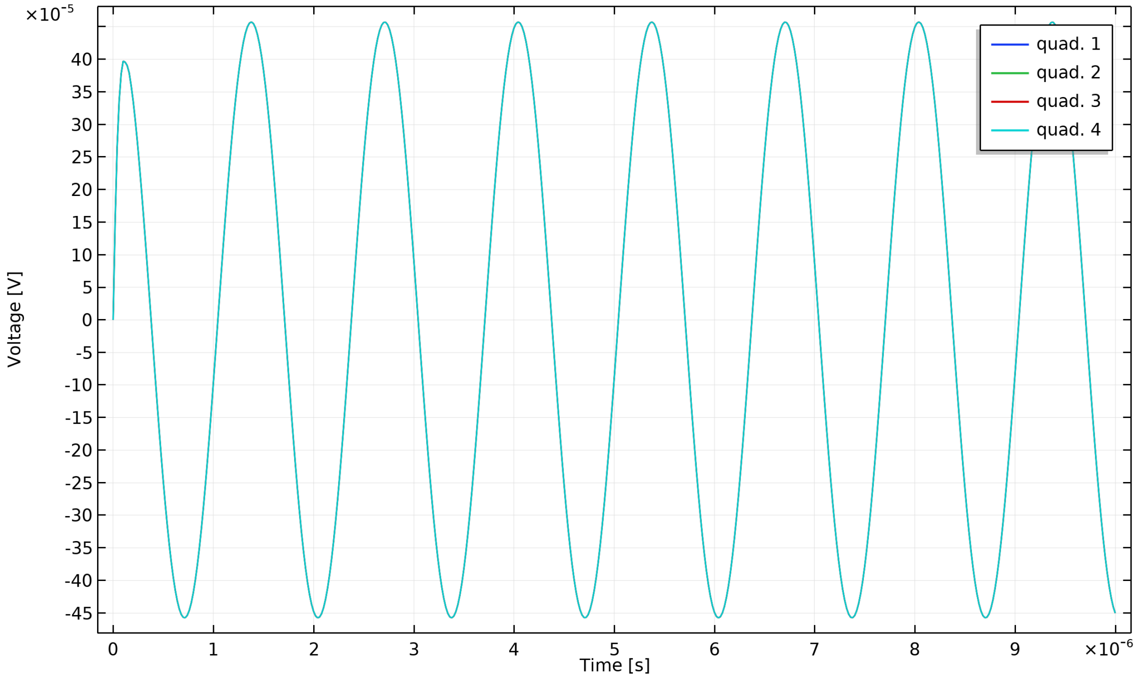

Figure B.1: The four measured induced voltages from the Rogowski BPM versus the time over a span of 10 µs when the parallel capacitors are not connected to coils' terminals.

B.2 Frequency domain analysis (study 2)

Figures B.2 shows the normalized magnetic flux density in the surface domains of the Rogowski windings (a) and the opposite quadrant 3 (b) when the quadrant coil 1 is excited with a current of 292.7 nA while the remaining quadrants are closed ended from the case study 9. The red arrows in figure represent the directional magnetic flux density along the x-,y- and z-axis.
Similarly, figure B.3 shows the normalized magnetic flux density in the surface domain of the neighboring quadrant 2 (a) and the neighboring quadrant 4 (b) from the same case study 9. Notice the smaller sized arrows that represent the magnetic flux lines opposing those created by exciting the quadrant coil 1 (as a result of setting the boundary condition as a closed circuit or $V = 0$).

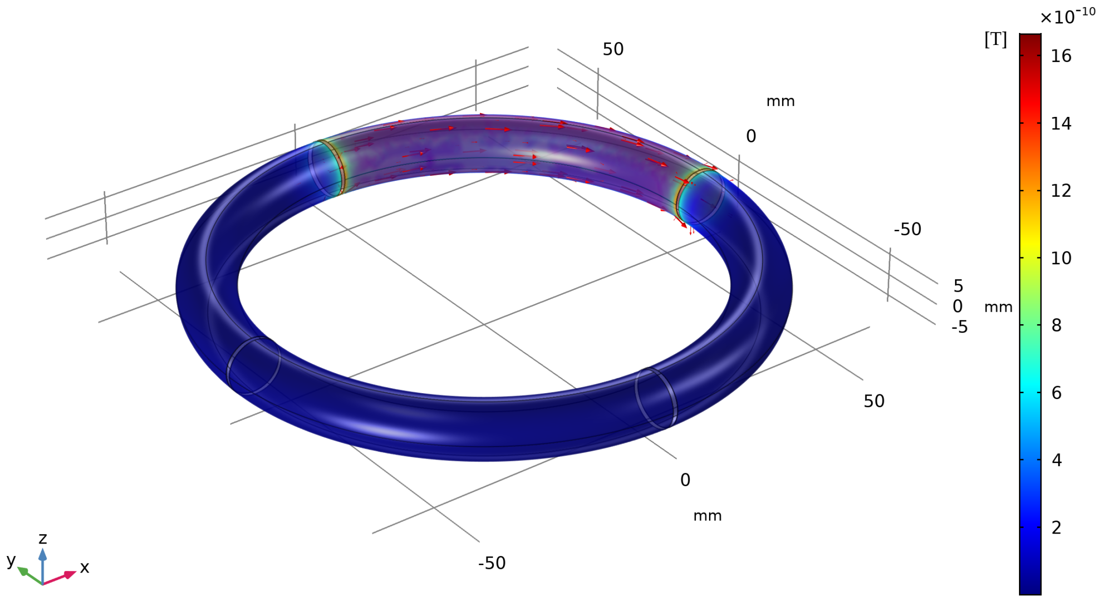

(a)

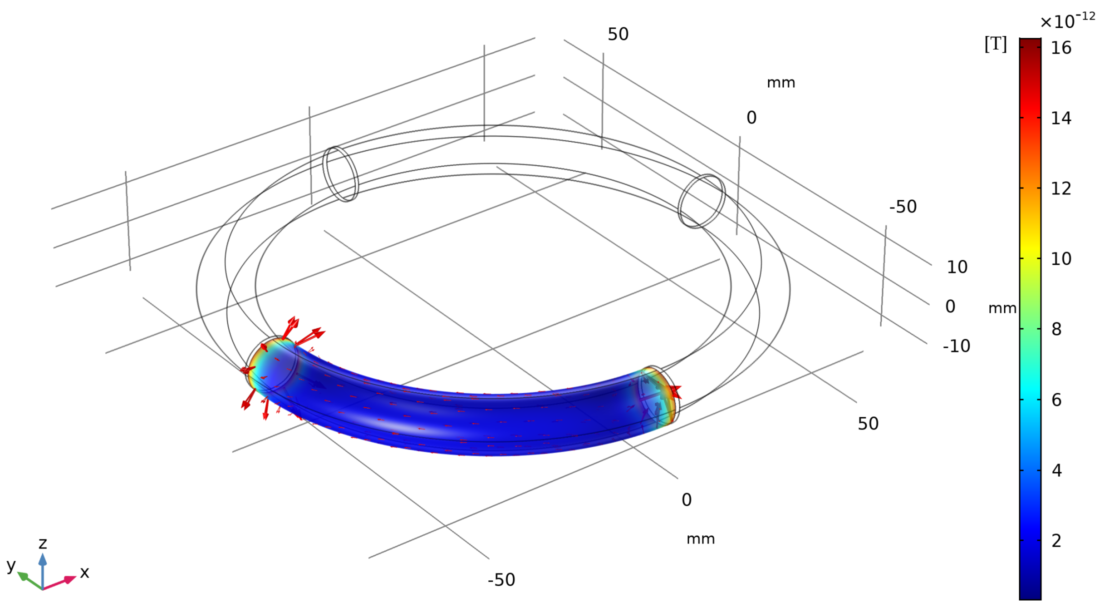

(b)

Figure B.2: Normalized magnetic flux density in the Rogowski's four domains when the quadrant 1 is excited with a current of 292.7 nA and the remaining quadrants are closed ended from the case study 9 (a). The same surface plot as in (a) for the domain of the opposite quadrant 3 (b). The red arrows represent the directional magnetic flux density along the x-,y- and z-axis.

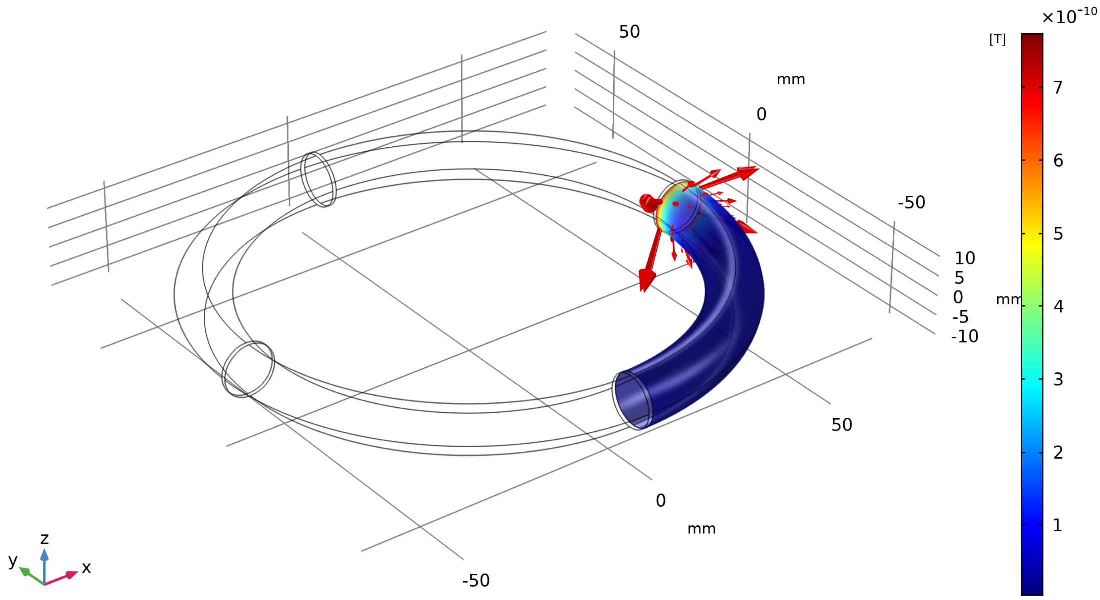

(a)

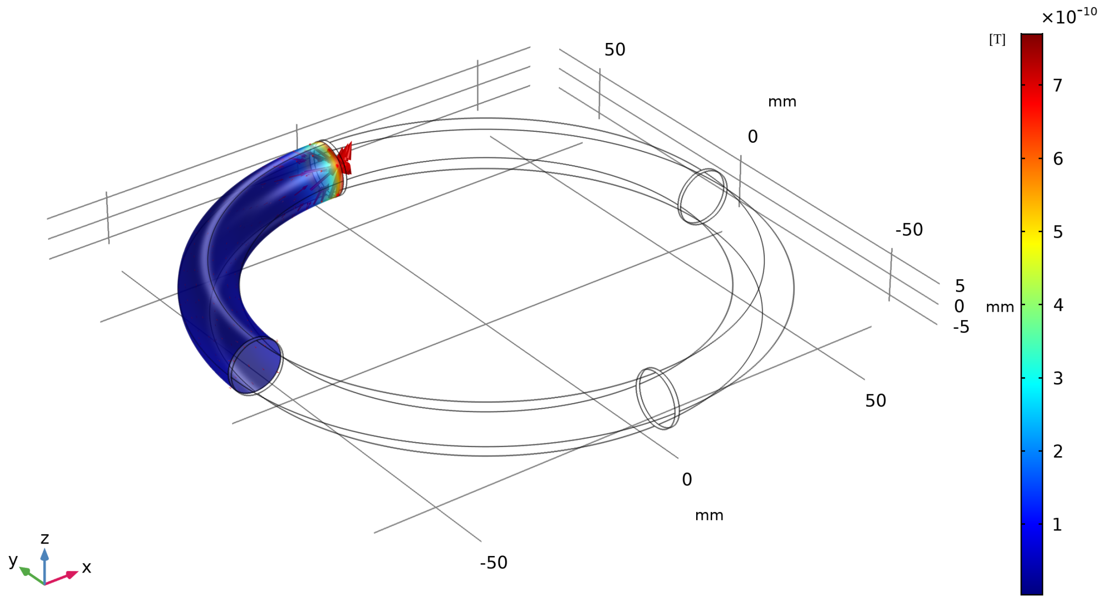

(b)

Figure B.3: Normalized magnetic flux density in the surface domains of the neighboring quadrant 2 (a) and the neighboring quadrant 4 (b) when the quadrant 1 is excited with a current of 292.7 nA and the remaining quadrants are closed ended from the case study 9. The red arrows represent the directional magnetic flux density along the x-,y- and z-axis.

B.3 Response for different winding orientation

Following the mathematical formula A.23 as stated in appendix A, the induced voltage response from the different quadrants of the Rogowski BPM for the second winding orientation (see figure 3.9 (b)) can be constructed. And using the following relations for the different quadrants:

$$\psi_1 = \frac{\pi}{4}, \tag{B.1}$$

$$\psi_2 = \frac{7\pi}{4}, \tag{B.2}$$

$$\psi_3 = \frac{5\pi}{4}, \tag{B.3}$$

$$\psi_4 = \frac{3\pi}{4}, \tag{B.4}$$

$$\Delta\psi = \frac{\pi}{2}, \tag{B.5}$$

the induced voltage for the four quadrants becomes:

$$\begin{aligned} U_{\text{in1}}(x,y,\omega) = \; & n\mu_0\omega I c_0' \Big[1 + c_1'(y) + c_2'(y^2 - x^2) + c_3'(y^3 - 3yx^2) \\ & + c_5'(-y^5 + 10y^3x^2 - 5x^4y) \Big], \end{aligned} \tag{B.6}$$

$$\begin{aligned} U_{\text{in2}}(x,y,\omega) = \; & n\mu_0\omega I c_0' \Big[1 + c_1'(x) + c_2'(x^2 - y^2) + c_3'(x^3 - 3xy^2) \\ & + c_5'(-x^5 + 10x^3y^2 - 5y^4x) \Big], \end{aligned} \tag{B.7}$$

$$\begin{aligned} U_{\text{in3}}(x,y,\omega) = \; & n\mu_0\omega I c_0' \Big[1 - c_1'(y) + c_2'(y^2 - x^2) + c_3'(-y^3 + 3yx^2) \\ & + c_5'(y^5 - 10y^3x^2 + 5x^4y) \Big], \end{aligned} \tag{B.8}$$

$$\begin{aligned} U_{\text{in4}}(x,y,\omega) = \; & n\mu_0\omega I c_0' \Big[1 - c_1'(x) + c_2'(x^2 - y^2) + c_3'(-x^3 + 3xy^2) \\ & + c_5'(x^5 - 10x^3y^2 + 5y^4x) \Big]. \end{aligned} \tag{B.9}$$

The difference over the sum must be constructed from the responses at the output, but if the quadrants are perfectly similar as in the case of the COMSOL modeling, the factor from deriving the output response will simply drop out as it should be a common factor for all coils. Additionally, if the contributions from the coupling between the coils were neglected as they ate on the few percent level for the lower frequency range, then one can use the previous four equations to develop a mathematical representation of the difference over the sum in the case of the second orientation of Rogowski winding. Using eqs. B.6-B.9, the horizontal ratio becomes:

$$\frac{\Delta_x}{\Sigma} = \frac{1}{2}\left[c_1^{'}(x) + c_3^{'}(x^3 - 3xy^2) + c_5^{'}(-x^5 + 10x^3y^2 - 5y^4x)\right]. \tag{B.10}$$

While the vertical ratio becomes:

$$\frac{\Delta_y}{\Sigma} = \frac{1}{2}\left[c_1^{'}(y) + c_3^{'}(y^3 - 3yx^2) + c_5^{'}(-y^5 + 10y^3x^2 - 5x^4y)\right]. \tag{B.11}$$

The values of the $c^{'}$ for this geometrical configuration are listed in the table below. For

Table B.1: The geometrical parameters for complete winding angular coverage in the second geometrical orientation.

Parameter	Expression
$c_0^{'}$	$R - u$
$c_1^{'}$	$\frac{2\sqrt{2}}{\pi u}$
$c_2^{'}$	$\frac{a^2}{\pi u^3(R-u)}$
$c_3^{'}$	$\frac{\sqrt{2}Ra^2}{3\pi u^5(R-u)}$
$c_5^{'}$	$\frac{\sqrt{2}a^2R(3a^2+4R^2)}{20\pi u^9(R-u)}$

the first orientation, the values of the c terms were given in table A.2 in appendix A. By comparing the parameters in both cases, and considering the linear approximation for the difference over the sum, the sensitivity to the positions can be compared by taking the ratio of the slopes for both orientations, which is approximated to:

$$\frac{\frac{1}{2}c_1^{'}}{c_1} \approx 0.7\,. \tag{B.12}$$

Appendix C

C.1 Gaussian error propagation on the calibration ratios

The horizontal and vertical ratios (the difference over the sum) are defined as:

$$\frac{\Delta_x}{\Sigma} = \frac{U_1 + U_2 - U_3 - U_4}{U_1 + U_2 + U_3 + U_4}, \tag{C.1}$$

$$\frac{\Delta_y}{\Sigma} = \frac{U_1 + U_4 - U_2 - U_3}{U_1 + U_2 + U_3 + U_4}. \tag{C.2}$$

Applying Gaussian error propagation on the above ratios results in:

$$\delta_{\frac{\Delta_x}{\Sigma}} = \frac{2\sqrt{({\delta_{U_1}}^2 + {\delta_{U_2}}^2)(U_3 + U_4)^2 + ({\delta_{U_3}}^2 + {\delta_{U_4}}^2)(U_1 + U_2)^2}}{\Sigma^2}, \tag{C.3}$$

$$\delta_{\frac{\Delta_y}{\Sigma}} = \frac{2\sqrt{({\delta_{U_1}}^2 + {\delta_{U_4}}^2)(U_2 + U_3)^2 + ({\delta_{U_2}}^2 + {\delta_{U_3}}^2)(U_1 + U_4)^2}}{\Sigma^2}, \tag{C.4}$$

where δU_i is the noise level from the ith quadrant, U_i is the amplified realistic signal from the ith quadrant. Σ is the sum signal.

C.2 Estimation of the Rogowski BPM's frequency characteristics

Based on the derivations of ω_0, $\Delta\omega$, ω_1 and $\gamma(\omega_0, \omega_1, \omega)$ (see the appendix A) and using the results from the measurement of the frequency response (see chapter 5, figure 5.2), the frequency characteristics of the single quadrants of the Rogowski BPM were calculated at the frequency of 750 kHz. The results are shown in table C.1.

Table C.1: The frequency characteristics of the four Rogowski quadrants calculated from the measurement of the frequency response in Figure 5.2

Quadrant	ω_0	$\Delta\omega$	ω_1	$\gamma(\omega_0, \omega_1, \omega = 2\pi \times 750\,\text{kHz})$[1]
1	7.446×10^6	183.431×10^3	30.222×10^7	1.669
2	7.603×10^6	187.961×10^3	30.750×10^7	1.625
3	7.634×10^6	305.111×10^3	19.101×10^7	1.616
4	7.665×10^6	344.708×10^3	17.046×10^7	1.607

[1] Units of ω terms are all in rad/s. The γ is unit-less.

C.3 Pre-amplifiers' gain factors

Figure C.1 shows the variations of the gain factors as a function of the frequency for the four pre-amplifiers used for signal amplification in one Rogowski BPM (upper subplot). The lower subplot is the ratio of the four gain factors with respect to the gain of the pre-amplifier 1. The numbers in the legend are indices referring to the different pre-amplifiers.

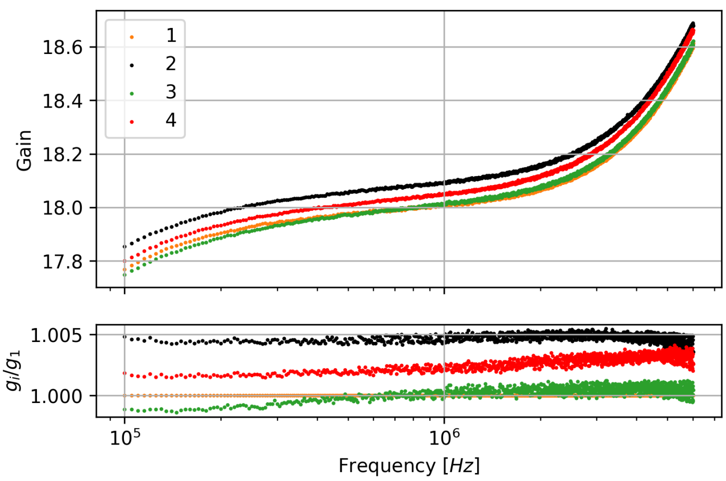

Figure C.1: Variations of the gain factors as a function of the frequency for the four pre-amplifiers used for signal amplification in one Rogowski BPM (upper subplot). The lower subplot is the ratio of the four gain factors with respect to the gain of the pre-amplifier 1. The numbers in the legend are indices referring to the different pre-amplifiers.

Bibliography

[1] Donald H Perkins and Donald H Perkins. *Introduction to high energy physics*. CAMBRIDGE university press, 2000.

[2] Donald H Perkins. *Particle astrophysics*. Number 10. Oxford University Press, 2009.

[3] Claudio Heller. Measurement of the cp violating phase φ s and the decay width difference $\delta\gamma$ s in the decay b 0 s$\rightarrow$ j/$\psi\varphi$ with the atlas experiment. 2013.

[4] Chien-Shiung Wu, Ernest Ambler, RW Hayward, DD Hoppes, and Ralph Percy Hudson. Experimental test of parity conservation in beta decay. *Physical review*, 105(4):1413, 1957.

[5] Paul R Lashomb. *MEASURING PARITY VIOLATION IN COBALT-60 DECAY*. PhD thesis, Houghton College, 2015.

[6] John Morrison. *Modern physics: for scientists and engineers*. Academic Press, 2015.

[7] Reza Moulavi Ardakani. Time reversal invariance in quantum mechanics. *arXiv preprint arXiv:1802.10169*, 2018.

[8] Elvira Gamiz. Kaon physics: Cp violation and hadronic matrix elements. *arXiv preprint hep-ph/0401236*, 2004.

[9] L Iconomidou-Fayard and D Fournier. The discovery of direct cp violation. In *60 Years of CERN Experiments and Discoveries*, pages 205–235. World Scientific, 2015.

[10] Manfred Jeitler. Cp violation in k decays: experimental aspects. 2006.

[11] Thomas Mannel. Theory and phenomenology of cp violation. *Nuclear Physics-Section B-PS-Proceedings Supplements*, 167:115–119, 2007.

[12] Yannis K Semertzidis. Storage ring edm experiments. In *EPJ Web of Conferences*, volume 118, page 01032. EDP Sciences, 2016.

[13] Matthias Le Dall, Maxim Pospelov, and Adam Ritz. Sensitivity to light weakly-coupled new physics at the precision frontier. *Physical Review D*, 92(1):016010, 2015.

[14] Diptimoy Ghosh and Ryosuke Sato. Lepton electric dipole moment and strong cp violation. *Physics Letters B*, 777:335–339, 2018.

[15] Nodoka Yamanaka. Nuclear electric dipole moment as a good probe of cp violation. In *Proceedings of the 8th International Conference on Quarks and Nuclear Physics (QNP2018)*, page 031033, 2019.

[16] Andreas Lehrach, Bernd Lorentz, William Morse, Nikolai Nikolaev, and Frank Rathmann. Precursor experiments to search for permanent electric dipole moments (edms) of protons and deuterons at cosy. *arXiv preprint arXiv:1201.5773*, 2012.

[17] JM Pendlebury, S Afach, NJ Ayres, CA Baker, G Ban, Georg Bison, Kazimierz Bodek, Martin Burghoff, Peter Geltenbort, Katie Green, et al. Revised experimental upper limit on the electric dipole moment of the neutron. *Physical Review D*, 92(9):092003, 2015.

[18] Jedi collaboration. `http://collaborations.fz-juelich.de/ikp/jedi/index.shtml`. Accessed: 2020-12-04.

[19] Takeshi Fukuyama and Alexander J Silenko. Derivation of generalized thomas–bargmann–michel–telegdi equation for a particle with electric dipole moment. *International Journal of Modern Physics A*, 28(29):1350147, 2013.

[20] F Rathmann, NN Nikolaev, and J Slim. Spin dynamics investigations for the electric dipole moment experiment. *Physical Review Accelerators and Beams*, 23(2):024601, 2020.

[21] William M Morse, Yuri F Orlov, and Yannis K Semertzidis. rf wien filter in an electric dipole moment storage ring: The “partially frozen spin” effect. *Physical Review Special Topics-Accelerators and Beams*, 16(11):114001, 2013.

[22] Jamal Slim. *A novel waveguide RF Wien filter for electric dipole moment measurements of deuterons and protons at the COoler SYnchrotron (COSY)/Jülich*. PhD thesis, RWTH Aachen University, Aachen, 2018.

[23] J Slim, R Gebel, D Heberling, F Hinder, D Hölscher, A Lehrach, B Lorentz, S Mey, A Nass, F Rathmann, et al. Electromagnetic simulation and design of a novel waveguide rf wien filter for electric dipole moment measurements of protons and deuterons. *Nuclear Instruments and Methods in Physics Research Section A: Accelerators, Spectrometers, Detectors and Associated Equipment*, 828:116–124, 2016.

[24] Marcel Stephan Rosenthal. *Experimental benchmarking of spin tracking algorithms for electric dipole moment searches at the cooler synchrotron COSY*. PhD thesis, RWTH Aachen University, Aachen, 2016.

[25] Fabian Hinder. *Development of Beam Diagnostic Systems for Electric Dipole Moment Measurements at Particle Accelerators*. PhD thesis, Universitätsbibliothek der RWTH Aachen, 2017.

[26] Walter rogowski. `https://de.wikipedia.org/wiki/Walter_Rogowski`. Accessed: 20121-04-22.

[27] M. A. Farahnakian M. H. Samimi, A. Mahari and H. Mohseni. The rogowski coil principles and applications: A review. *IEEE Sensors Journal*, 15:651–658, 2015.

[28] Slawomir Tumanski. Induction coil sensors—a review. *Measurement Science and Technology*, 18(3):R31, 2007.

[29] Mohammad Hamed Samimi, Arash Mahari, Mohammad Ali Farahnakian, and Hossein Mohseni. A review on the rogowski coil principles and applications. *measurements*, 4:5, 2013.

[30] Theodore Frankel. Maxwell's equations. *The American Mathematical Monthly*, 81(4):343–349, 1974.

[31] Klaus Wille. *The physics of particle accelerators: an introduction*. Clarendon Press, 2000.

[32] Robert G Brown. Classical electrodynamics. *Robert Brown, URL http://www. phy. duke. edu/˜ rgb/Class/phy319/phy319/phy319. html*, 2009.

[33] Andrew McHutchon. Electromagnetism laws and equations.

[34] DJ Griffiths. Introduction to electrodynamics 4th edn (harlow, 2014.

[35] A Murari, C Vinante, and M Monari. Comparison of peek and vespel® sp1 characteristics as vacuum seals for fusion applications. *Vacuum*, 65(2):137–145, 2002.

[36] HJ Stein, D Prasuhn, H Stockhorst, J Dietrich, K Fan, V Kamerdjiev, R Maier, IN Meshkov, A Sidorin, and VV Parkhomchuk. Present performance of electron cooling at cosy-j\" ulich. *arXiv preprint arXiv:1101.5963*, 2011.

[37] V Kamerdzhiev, J Dietrich, et al. Nondestructive beam instrumentation and electron cooling beam studies at cosy. 2010.

[38] C Böhme, J Dietrich, V Kamerdzhiev, M Bryzgunov, V Reva, BINP A Kobets, I Meshkov, A Rudakov, N Shurkhno, and A Sidorin. Results of electron cooling beam studies at cosy. *Proceedings of RuPAC*, 2010.

[39] F. Trinkel. *Development of a Rogowski coil Beam Position Monitor for Electric Dipole Moment measurements at storage rings*. PhD dissertation, RWTH Aachen University, Department of Physics, Dec 2017.

[40] G Murtaza Hashmi, Matti Lehtonen, and Abdelsalam ELHAFFAR. Modeling of rogowski coil for on-line pd monitoring in covered-conductor overhead distribution networks. *Pulse*, 1:P2, 2007.

[41] Guillermo Robles Muñoz, Muhammad Shafiq, and Juan Manuel Martínez Tarifa. Designing a rogowski coil with particle swarm optimization. 2018.

[42] ZÁ Tamus. High frequency behavior of rogowski-coil passive l/r integrator current transducer. In *IEEE Postgraduate Conference on Electrical Power Systems*, volume 8, pages 115–118, 2002.

[43] Daniel McBrearty. *Electronics calculations data handbook*. Elsevier, 1998.

[44] Seon-Jae Jeon and Dong-Wook Seo. Coupling coefficient measurement method with simple procedures using a two-port network analyzer for a multi-coil wpt system. *Energies*, 12(20):3950, 2019.

[45] Theodoros Theodoulidis and Robert J Ditchburn. Mutual impedance of cylindrical coils at an arbitrary position and orientation above a planar conductor. *IEEE Transactions on Magnetics*, 43(8):3368–3370, 2007.

[46] *Coupling Between Coils or Coefficient of Coupling (Leakage Inductance)*. `https://www.w0qe.com/Technical_Topics/coupling_between_coils.html`.

[47] COMSOL Multiphysics and CMHT Module. Comsol multiphysics user's guide. *Version: COMSOL Multiphysics 5.5*, 2019.

[48] AB Comsol. Comsol multiphysics-ac/dc module, user's guide, 2019.

[49] HA Haus and JR Melcher. Introduction to electroquasistatics and magnetoquasistatics. *Electromagnetic Fields and Energy*, pages 1–22, 1989.

[50] S Frei, RG Jobava, D Karkashadze, A Gheonjian, and E Yavolovskaya. Calculation of low frequency emc problems in large systems with a quasi-static approach. In *2004 International Symposium on Electromagnetic Compatibility (IEEE Cat. No. 04CH37559)*, volume 3, pages 798–803. IEEE, 2004.

[51] ID Vagner, BI Lembrikov, and P Wyder. Quasi-static electromagnetic field. In *Electrodynamics of Magnetoactive Media*, pages 68–81. Springer, 2004.

[52] Howard Johnson, Howard W Johnson, and Martin Graham. *High-speed signal propagation: advanced black magic*. Prentice Hall Professional, 2003.

[53] William H Hayt Jr, John A Buck, and M Jaleel Akhtar. *Engineering Electromagnetics | (SIE)*. McGraw-Hill Education, 2020.

[54] *MUltifrontal Massively Parallel Solver*. `http://mumps.enseeiht.fr/doc/userguide_5.4.0.pdf`.

[55] CD Sijoy and S Chaturvedi. Fast and accurate inductance calculations for arbitrarily-wound coils for pulsed power applications. In *2005 IEEE Pulsed Power Conference*, pages 1464–1467. IEEE, 2005.

[56] *Keysight Technologies*. `https://literature.cdn.keysight.com/litweb/pdf/5991-0692EN.pdf`.

[57] B Hoistad, J Ritman, COSY Collaboration, et al. Proposal for the wide angle shower apparatus (wasa) at cosy-juelich-" wasa at cosy". *arXiv preprint nucl-ex/0411038*, 2004.

[58] Magnus Wolke. The wasa facility at cosy. *Nuclear Physics News*, 20(4):29–32, 2010.

[59] *LIMES 150-IMS*. https://www.owis.eu/fileadmin/user_upload/owis.eu/products/pdf/pi_limes_150-ims.pdf.

[60] *API laser tracker 3*. https://wiki.lbto.org/pub/Engineering/TelescopeAlignment/Tracker3_15-40-60_UserManual_2008.pdf.

[61] *HF2LI Lock-in Amplifier*. https://www.zhinst.com/products/hf2li.

[62] Niels Marquardt. Introduction to the principles of vacuum physics. 1999.

[63] Giuliano Franchetti. Vacuum i. 2013.

[64] Eshraq Al-Dmour. Fundamentals of vacuum physics and technology. *arXiv preprint arXiv:2006.01464*, 2020.

[65] Ari Krister Riihimaki. *Outgassing Studies of Some Accelerator Materials*. PhD thesis, Helsinki U., 2019.

[66] E Fischer. Ultra-high vacuum. 1974.

[67] *Pirani gauge head TPR 018*. https://www.pfeiffer-vacuum.com/productPdfs/PTR15014.en.pdf.

[68] *Cold cathode gauge head IKR 070*. https://www.pfeiffer-vacuum.com/productPdfs/PTR20501.en.pdf.

[69] *AMETEK, Dycor LC-D200M*. http://208.112.27.152/files/RGAs/Ametek/Ametek%20Dycor%20LC-D%20Residual%20Gas%20Analyzer%20RGA%20Manual.pdf.

[70] *Balzers Instruments, QualyTest HLT260*. http://nanophys.kth.se/nanophys/facilities/nfl/leakdetector/Pfeiffer_HLT_260_Qualytest.pdf.

[71] *Pfeiffer HiCube 300*. https://mmrc.caltech.edu/Optical%20Furnace/Manuals/Pfeiffer%20HiCube%20Classic%20Manual.PDF.

[72] Debanjan Polley, Nanna Zhou Hagström, Clemens von Korff Schmising, Stefan Eisebitt, and Stefano Bonetti. Terahertz magnetic field enhancement in an asymmetric spiral metamaterial. *Journal of Physics B: Atomic, Molecular and Optical Physics*, 51(22):224001, 2018.

[73] Krishna Naishadham. Closed-form design formulas for the equivalent circuit characterization of ferrite inductors. *IEEE transactions on electromagnetic compatibility*, 53(4):923–932, 2011.

[74] *R&S®ZVL Vector Network Analyzer*. https://scdn.rohde-schwarz.com/ur/pws/dl_downloads/dl_common_library/dl_brochures_and_datasheets/pdf_1/ZVL_bro_en.pdf.

[75] Christian Böhme, Ilja Bekman, Vsevolod Kamerdzhiev, Bernd Lorentz, Michael Simon, Christian Weidemann, et al. Cosy orbit control upgrade. In *6th Int. Beam Instrumentation Conf.(IBIC'17), Grand Rapids, MI, USA, 20-24 August 2017*, pages 263–266. JACOW, Geneva, Switzerland, 2018.

[76] Robert E Shafer. Beam position monitoring. In *AIP conference proceedings*, volume 249, pages 601–636. American Institute of Physics, 1992.

[77] Giuseppe Vismara. Signal processing for beam position monitors. In *AIP Conference Proceedings*, volume 546, pages 36–60. American Institute of Physics, 2000.

[78] Peter Forck, D Liakin, and P Kowina. Beam position monitors. 2009.

[79] Stephen R Smith. Beam position monitor engineering. In *AIP conference proceedings*, volume 390, pages 50–65. American Institute of Physics, 1997.

[80] C Simon, D Roudier, M Luong, D Nölle, J Novo, O Napoly, S Chel, N Mildner, N Baboi, and N Rouvière. The cold re-entrant bpm. Technical report, CARE, 2007.

[81] Alexander Wu Chao, Karl Hubert Mess, et al. *Handbook of accelerator physics and engineering*. World scientific, 2013.

[82] Jamal Slim. Multibunch spin manipulation for the deuteron edm measurement in storage rings. Presented as online talk for the DPG Spring Meetings - Dortmund, 2021. `http://collaborations.fz-juelich.de/ikp/jedi/public_files/usual_event/DPG_Slim_2021.pdf`.

[83] F Abusaif, A Aggarwal, A Aksentev, B Alberdi-Esuain, L Barion, S Basile, M Berz, M Beyß, C Böhme, J Böker, et al. Feasibility study for an edm storage ring. *arXiv preprint arXiv:1812.08535*, 2018.

[84] M. Rosenthal. Rf wien filter based edm measurements using clock wise/counterclockwise beams. JEDI: Internal Note. 2. `https://indico.cern.ch/event/570680/contributions/2310234/attachments/1341838/2025273/Spin16_MR.pdf`.

[85] Storage Ring EDM Collaboration. A proposal to measure the proton electric dipole moment with 10^{-29} e cm sensitivity. 2011. `https://www.bnl.gov/edm/files/pdf/proton_EDM_proposal_20111027_final.pdf`.

Typeset November 17, 2021